Size Selection and Monolayer Enrichment in Liquid Exfoliated Tungsten Disulphide Dispersions

Beata Maria Szydłowska

A thesis submitted for the degree of
Doctor of Philosophy in physics

Supervised by
Prof. Jonathan N. Coleman & Prof. Werner J. Blau

School of Physics
Trinity College Dublin

2018

Statement of Originality

I declare that this thesis has not been submitted as an exercise for a degree at this or any other university and it is entirely my own work.

I agree to deposit this thesis in the University's open access institutional repository or allow the library to do so on my behalf, subject to Irish Copyright Legislation and Trinity College Library conditions of use and acknowledgement.

Beata Maria Szydłowska

Acknowledgements

First I would like to thank **Professor Werner J. Blau** for giving me the oppourtunity to start my PhD. For allowing me to work in his Molecular Electronics and Nanotechnology group and to expand my education in such a great place as the Trinity College Dublin. I want to especially thank him for his kindness and support and all the oppourtunities he gave me to collaborate and travel for coferences, trainings and summer schools. That has trully enriched me and I will be always greatfull for that.

I would also like to thank **Professor Jonathan N. Coleman.** First for helping me out in difficult time and letting me into his Chemical Physics of Low Dimensional Nanostructures Group. Atlhough I was an official member for the last year only, I felt as a part of the group much earlier. I believe his attitude make the group vibrating environment (both, scientificly and personally) and I loved every minute of being its part. I greatly apprieciate all Professor Jonathan N. Coleman's advice, guidance, discussions, supervision and scientific input over the last three years as well as an attitude towards me and support in general.

A very special thanks go to **Dr. Claudia Backes.** This work could not have been done without her. Thanks a million for all advices, supervision, help, long weekends in the lab, Saturday chats and for most, being a good teacher and a friend at all the time. Thanks for all the exciting moments and uplifting me while needed.You invested quite a bit of trust in me, and day by day showed how amazing and beautifull science is.

Thanks to all **Blau Group** and **Coleman Group** members (the former and actual ones). For the help, funny conversations, listening to complains and sharing the painfull and happy moments in the SNIAM basement. It was great to meet you all and share so many moments. I was very happy and lucky to be a part of such a great community of amazing, warm and cheerfull people. I am very thankfull I could have always count on help

or good word (sometimes mean too...) in any situation. Besides, huge thanks to people who corrected my bad English and other mistakes and patiently read parts of this thesis (Aideen, Adam, JB, Cian, Claudia, John and Victor) and for cheerfull coffe breaks.

Thanks to all of you – I belived there is such a thing like co-working, helping and looking out at each other, I will always remember it and put as an example!

Outside of college I want to thank my parents for always putting my education first. You have instilled in me the values of hard work, self motivation and perseverance. Thanks to my brother Paweł for being around and beliving in my "luck" and capabilities (remember you are as capable as I am!). Thanks to Bartek for being a rock by my side in good and bad moments and for cheering me up whenever I was down.

Last but not least to all the people who I didn't mentioned but who surrely contributed to my experience at Trinity and in Dublin. To all those who in past 4 years have left a fingerpring on my life and undoubtly changed it to the one I have now.

Thank you all!

Publications

[1] **Szydlowska, B.M.** and W. Blau, “Highly monolayer enriched ws2 dispersions produced by liquid phase exfoliation in liquid cascade as nonlinear optical materials,” *Advanced Photonics 2016 (IPR, NOMA, Sensors, Networks, SPPCom, SOF)*, 2014. DOI: 10.1364/NOMA.2016.NoTu3D.5.

[2] C. Backes, D. Hanlon, **Szydlowska, B.M.**, A. Harvey, R. Smith, T. Higgins, and J. Coleman, “Preparation of liquid-exfoliated transition metal dichalcogenide nanosheets with controlled size and thickness: A state of the art protocol,” *Journal of Visualized Experiments*, 2016. DOI: 10.3791/54806.

[3] C. Backes, **Szydlowska, B.M.**, A. Harvey, S. Yuan, and V. Vega-Mayoral, “Production of highly monolayer enriched dispersions of liquid - exfoliated nanosheets by liquid cascade centrifugationn,” *ACS Nano*, 2016. DOI: 10.1021/acsnano.5b07228.

[4] K. Wang, **Szydlowska, B.M.**, G. Wang, X. Zhang, J. Wang, J. Magan, L. Zhang, J. Coleman, J. Wang, and W. Blau, “Ultrafast nonlinear excitation dynamics of black phosphorus nanosheets from visible to mid-infrared,” *ACS Nano*, 2016. DOI: 10.1021/acsnano.6b02770.

[5] J. J. Gough, K. E. Siewerska, S. Mehigan, D. Hanlon, C. Backes, Z. Gholamvand, **Szydlowska, Beata M**, W. J. Blau, E. McCabe, and A. L. Bradley, “Influence of graphene oxide/ag nanoparticle composites on the fluorescence properties of organic dyes,” *Journal of Nanoscience and Nanotechnology*, 2017. DOI: 10.1166/jnn.2017.13889.

[6] A. Harvey, J. Boland, I. Godwin, A. Kelly, **Szydlowska, B.M.**, G. Murtaza, A. Thomas, D. Lewis, P. OBrien, and J. Coleman, “Exploring the versatility of liquid phase exfoliation: Producing 2d nanosheets from talcum powder, cat litter and beach sand,” *2D Materials*, 2017. DOI: 10.1088/2053-1583/aa641a.

[7] G. Wang, K. Wang, **Szydlowska, B.M.**, A. Baker-Murray, J. Wang, Y. Feng, X. Zhang, J. Wang, and W. Blau, “Ultrafast nonlinear optical properties of a graphene saturable mirror in the 2 um wavelength region,” *Laser and Photonics Reviews*, 2017. DOI: 10.1002/lpor.201700166.

Abstract

Since the the discovery of graphene in 2004, the scientific environment turned its great interest towards new type of nanomaterials, commonly called two dimensional (2D) layered nanomaterials. Over last 15 years, they consistently prove to have unique properties, which can only be seen when their lateral dimensions are taken into the nanoscale. Honouring their favourable properties, many new applications have emerged, ranging from gas sensing, transistor technologies, optical switches to energy storage devices. Although there are several methods to exfoliate layered crystals, Liquid Phase Exfoliation (LPE) method developed by Coleman et al. was used in work described in this thesis. It applies to a wide range of layered materials such as graphene, hexagonal boron nitride, transition metal dichalcogenides (including WS_2) and even materials like talc or cat litter.

This thesis is dedicated to in-depth investigation of Tungsten Disulphide (WS_2), a semiconducting transition metal dichalcogenide (TMDC). Described work starts with the WS_2 powder and is aimed at the production of high-quality 2D nanosheets in aqueous dispersion (LPE). The size selected WS_2 nanosheets dispersions are proven to be state of the art by a range of characterisation techniques. Those include AFM, TEM, Absorption and Extinction Spectroscopy, Raman Spectroscopy and Photoluminescence spectroscopy. Moreover, the size dependent Nonlinear Optical (NLO) response of WS_2 nanosheets are studied. Their saturable absorption (SA), as well as optical limiting (OL) capabilities were demonstrated. Further, thanks to the development of multiple secondary cascades, WS_2 dispersions are taken to an enriched level, where the monolayer volume fraction in the dispersions is ˜ 75%. Finally, high quality, uniform, optically active WS_2-PMMA composite thin films are produced. They will surely find a real life application as the pristine properties of WS_2 produced from LPE are from now on accessible in the solid state.

Contents

List of Figures

List of Tables

List of Acronyms

PMMA	Poly(methyl methacrylate)
TMDC	Transition Metal Dichalcogenide
NLA	Nonlinear Absorption
NLE	Nonlinear Extinction
LPE	Liquid Phase Exfoliation
AFM	Atomic Force Microscopy
PL	Photoluminescence
TEM	Transmission Electron Microscopy
LCC	Liquid Cascade Centrifugation
OA	Open Aperture
OAD	Open Aperture Detector
RD	Reference Detector
SC	Cholate Hydrate
SA	Saturable Absorption
OL	Optical Limiting
SHG	Second Harmonic Generation
CMC	Critical Micelle Concentration
RSA	Reversed Saturable Absorption
VB	Valence Band

CB	Conduction Band
ML	Monolayer
NLA	Nonlinear Absorption
NLS	Nonlinear Scattering
NLO	Nonlinear Optical
OD	Optical Density
FL	Fewlayered
NMP	N-methyl-pyrrolidone
BE	Bound Excitonic
CVD	Chemical Vapour Deposition
FWHM	Full Width of the Half Maximum

Chapter 1

Literature background on materials

1.1 Introduction

The following chapter will introduce the brilliance of nanotechnology and its surprisingly long history and benefits to human kind. The review will include the history, properties, applications and various production methods of nanomaterials. The story will start with carbon-based materials, which are not the main focus of this thesis but played a major role in the development of nanotechnology. Understanding their properties was a fundamental discovery and led to an ignition of the 2-dimensional (2D) branch of research. This will be followed by a deeper discussion of Transition Metal Dichalcegonides (TMDC s) family, with special consideration given to tungsten disulphide (WS_2), which is the material of greatest interest in this thesis. Finally, a short review of 2D material production methods focusing on Liquid Phase Exfoliation (LPE) will be presented.

1.2 Nanotechnology

Nanotechnology is the term which can easily be used as a key word describing material science currently. It describes materials with at least one dimension in the range of 1-100 nm. Depending on the number of the dimensions in that range the material can be classified as 0D, 1D, or 2D. The change of these dimensions is closely followed by the physico-chemical properties of the material like plasmon resonance in metal particles or quantum confinement effects in semiconductors. The last one is observed when the size of the particle is comparable to the wavelength of the electron. To describe this effect one may break "quantum confinement" into two words: quantum and confinement. Confinement means to confine the motion of randomly moving electron to restrict its motion in specific energy levels and quantum reflects the atomic nature of particles.

Materials considered in this work decrease their size in exfoliation proces from macro to a nano scale. Effectivelly, the decrease in confining dimension makes the energy levels discrete and results in increased or widened up band gap what ultimately make the band gap energy increases.

One might think that nanotechnology is a development of our century, but in fact it is present since very early ages. It is impossible to date the first time when the nanotechnology such as we understand it appeared. Nonetheless, it is known that as early as in the 9$^{\text{th}}$ century, nanoparticles were used by craftsmen to create the glittering effect on the pottery in Mesopotamia. A later example of the presence of nanotechnology comes from the middle ages, where metals were specially treated to generate lustre posts or to make flexible and sharp objects by infusing metals with structures known today as carbon nanotubes. Another example is very popular production of stained glass. Regardless of the mentioned above use of nanotechnology in every-day life, people knew nothing about nanotechnology back then. They were only blindly following traditional recipes having in mind only the certain results to be achieved.

The first time, when nanotechnology made an official appearance was in the 19th century. Faraday discovered then that gold nanoparticles are no longer metallic when they are small enough and that they change colour below a certain size. Although Faraday's discovery is considered to be a first scientific approach to nanotechnology, the first scientific publication about nanomaterials with 2D crystalline structure was printed in 1922 (CdI_2) [33] and then in 1930 (MoS_2) [68]. Graphene itself was for the first time descrbed in 1925 by Bernal. Those were followed by many theoretical studies about to be discovered, observed, synthesised and explored low-dimensional structures [16], [68]. Finally, in 1985, the fullerene's discovery (0D structures) started the race of the exploration of predicted materials.

Even before the nanomaterials made such an appearance in scientific journals, their tremendous impact on the development of technology was seen and predicted by bright minds of the 20th century. In 1959, in the speech "There is plenty of room at the bottom", famous Richard Feynman predicted the possibility of new discoveries while moving knowledge and attention into low dimensional systems and materials. They still did not exist at his times but are explored in depth by scientific community and surely will leave a significant fingerprint on the technology we know now, and will see in future decades.

1.3 Layered Materials

Graphite is undoubtedly the most known and famous among 2D layered materials. The same one can be exfoliated into graphene [17], what was done for the first time in 2004 [17] by A. Geim and K. Novoselov and recognised as such a great discovery that it was awarded a Nobel Prize in 2010. While still in 3D crystalline graphite form, the layers are stacked on each other by Wan der Waals interactions which are broken by exfoliation and as a result isolate Graphene monolayers. This is a 2D layered material composed of carbon atoms of sp^2 hybridisation. The atoms in graphene form a honeycomb shaped planar structure, where carbon atoms are covalently bonded to each other. As the structure gets thinner, and the number of layers is decreased reaching a monolayer, the properties of the material change dramatically. Unlike graphite, graphene is highly electrically conductive and a mechanically strong material.

Although graphene opened the window to a new type of nanomaterials and raised high hopes, it is not the only 2D material known. The broad range of 2D nanomaterials includes the Transition Metal Dichalcegonides (TMDCs) family with WS_2 of most interest here. However each material might exhibit different chemical nature due to present atomic species and their apparent configuration; they are all built out of individual layers stacked on the top of each other and bonded with relatively weak Van der Walls interactions. These interactions are weak enough to make it possible to easily and efficiently exfoliate mentioned materials into few and single layers accessing their new unique properties.

1.3.1 Transition Metal Dichalcegonides – especially WS_2

Transition Metal Dichalcogenides (TMDCs) are a group of materials with MX_2 stoichiometry. M is a transition metal (group IV, V, VI in the periodic table), eg. Mo, W, Nb. X is a chalcogen, e.g. sulphur, selenium, tellurium. The TMDCs family is huge, and there are about 60 possible configurations [57]. Different from zero-bandgap graphene, TMDC materials offer a broad range of electronic properties such as semiconducting [39], metallic [69], semimetallic [85] or superconducting [40].

In any TMDC material, the transition metal is placed between two chalcogen layers. Typically, the in-plane bonding is strong, but individual layers are held together by weak van der Waals out of plane bonding. These exist in the sandwich form of individual layers stacked one on the top of another. The configuration of the stacking leads to the creation of different polymorphs[2], [39]. They are classified as two types of atomic arrangements [27]: the trigonal prismatic and the octahedral [41]. Depending on the above mentioned arrangement, the material could either exhibit semiconducting (e.g. MoS2, WS2, WSe2 and MoSe2) or metallic-superconducting behaviour (e.g. NbS2 and NbSe2)[27], [41], [69], [86], [114].

The electronic properties of Transition Metal Dichalcogenides are very promising. As mentioned previously, depending on the configuration of transition metal and chalcogen their electronic properties range from semiconducting to metallic. Transition metals properties are determined by the *d* orbitals, where configuration changes from left to right across the periodic table. That configuration affects the electronic properties of the current carrier directly. A semiconducting subgroup of TMDCs (where WS_2 belongs to) can be n- or p-type depending on the relative configuration of atoms in the structure. WS_2 itself is an n-type semiconductor.

Normally, the bulk hexagonal phases (trigonal prismatic) of semiconducting TMDCs reveal an indirect band gap. That was confirmed both by first principles calculations[23], [86] and experimentally through photoluminescence in exfoliated[42], [58], [87] and chemical vapour deposited monolayers of WS_2.

As a semiconductor, WS_2 has specific bandgap[39], [43] which is around 1.9 eV [102], and is physically defined as an energy difference between the Conduction Band (CB) minimum and Valence Band (VB) maximum. Normally in WS_2, the transitions from Valence Band to Conduction Band are indirect, as the minimum of the CB and maximum of the VB do not overlap. The bandgap of WS_2 increases, as the material is transformed from bulk to monolayer or when the chalcogen atom is substituted. The change is caused by quantum confinement of electrons in the structure. The most direct method to probe such a change is the Photoluminescence measurement, where the transition can be observed. For most of the TMDCs (including WS_2) it is observable only for monolayer.

TMDCs nanosheets also exhibit unique size dependent nonlinear optical properties [8] changing from Saturable Absorption (SA) to Reversed Saturable Absorption (RSA) as the lateral dimensions changes. For semiconducting materials, SA phenomena is commonly observed. It is associated with the depletion of free carriers. In the visible light, it is mostly related to the excitation of the free carriers in the material.

The fundamental physics of the atomically thin TMDCs are dependent not only on the type of the metal and chalcogenide atom [88] in the structure but also on the lateral sheet dimensions [28]. TMDCs' band structure strongly depends on its number of layer. This size dependence is an excellent handle for property manipulation.

1.3.2 Applications of TMDCs

TMDCs are a family of materials with unique and extraordinary properties. The types of 2D materials available has been growing and now includes insulators, (e.g., hexagonal boron nitride), semiconductors (e.g., transition metal dichalcogenides, TMDs), and semi-metals (e.g., black phosphorus). From these new materials, a wide array of optical, mechanical, chemical and electric phenomena have been realized. They become widely explored nanomaterials and hold promise for technological applications in a variety of areas fields like energy storage[70], [103], transistors [89], hydrogen evolution[103], [116], photonic devices[9], [22], photodetection [25], flexible electronics[71], [90], chemical sensing [4] and broadly understood electronics. The last one governed a huge interest in applying TMDCs materials into electronic devices (e.g. transistors[44], [118]) mainly due to their bandgap existing in monolayers which is a significant advantage over pure graphene.

The list of applications where 2D materials are expected to be used or are being already used is very broad and still open. To list a few there are: batteries[95], [113], [115], [121], secutity devices[24], [107], conductive inks[91], [112], [120], 3D printing[111], supercapacitors[123], fuel cells[99], [117] or water filtration[124]. Due to the high performance and stability (of many 2D materials) among the most novel and promising applications of 2D materials are flexible devices and nanoscale electronics and optoelectronics.

While some TMDCs like MoS_2 have received big attention due to its relative ease of mechanical exfoliation, its close relative WS_2 (formed by hexagonally packed [119] layers of covalently bonded in-plane S-W-S atoms) draw the attention by demonstrated optical properties[34], [102], [119]. A direct bandgap presented in single-layer WS_2 is an attractive characteristic for developing optoelectronic devices.

In monolayer TMDs are said to have a spin valence band that is almost fully spin polarised near K and K' points of the Brillouin zone. The spin polarization is predicted to be reversed between the K and K' points, implying the existence of an unusual spin-valley coupling in the TMDs. In particular, this splitting is predicted to be entirely a consequence of spin-orbit coupling in the monolayer limit and a combination of spin-orbit coupling and interlayer interaction in the bulk limit. Current electronic band structure studies of bulk WS_2 are limited by energy and momentum resolution and lack focus on the valence-band splittings. Experimentally, the sizes of the splittings have been characterized, but only with limited resolution. The ability to selectively populate [22], [26], [101] the mentioned valleys demonstrates their viability for use in spintronics and valleytronics devices. [45] Described spin-orbit coupling [59], suggests WS_2 may also exhibit stronger magnetic field effects which are desired for optoelectronic and spintronic functionalities as well as field effect transistors.

In general, TMDCs have shown a thickness-dependent electronic band structure[46], [118] and relatively high carrier mobility [44]. As one of them, WS_2 exhibits the transition from indirect to direct bandgap when exfoliated from bulk into monolayer [47]. WS_2 is a semiconductor with an indirect bandgap of 1.4 eV in bulk while the monolayer WS_2 form has a direct bandgap of 2.1 eV [48].

Although WS_2 electrical characteristics are sensitive to the environment (the obvious drawbacks for its use in devices production), WS_2 serves recently as a centre of the interest for next-generation nanoelectronic and optoelectronic materials. It is due to its high ON/OFF current ratio, high thermal stability, the absence of dangling bonds, and electrostatic integrity [20]. An atomically thin layer of WS_2 is surely a strong competitor to graphene and traditional semiconductors. It is seen as a potential future in a broad range of applications.

1.4 Production Methods of 2D Nanomaterials

There are several different methods available to produce 2D layered materials[18], [72], [81], [92]. Although all of them lead to 2D nanosheets, they are classified into two groups based on the scientific approach: bottom-up and top-down. First group – bottom-up include self-assembly[60], [104] (typically in the wet chemical process) and Chemical Vapour Deposition[73], [81] (CVD). Second group: top-down methods include mechanical cleavage [17] and liquid-based methods like Li-ion intercalation and Liquid Phase Exfoliation (LPE). Although each method has its own positive and negative aspects, some of them for example lead to nanosheets high in defects or are difficult to scale up. The choice of production method is always governed by calculation of 3 factors: quantity and quality of the material and desired application. For instance, CVD produced nanosheets are excellent for electronic applications while LPE produced material is preferred in any application which require extremally high quantities of nanosheets.

The first method ever used to isolate monolayers of 2D materials is mechanical cleavage [17]. It is also well known as “Scotch tape method” and was for the first time used by Frindt to isolate MoS_2 nanosheets in 1963.It was also the one first time used to produce graphene. The method provides high-quality monolayers, but it is very time consuming and generates very low output. The CVD technique [29] is the next popular technique used to produce few or monolayers of 2D layered materials. It is applicable not only to Graphene but also to TMDCs. To produce monolayer material out of the bulk through the CVD method [35], a metal substrate (such as copper) is heated to about 1000 °C increasing its domain size. Then a carbon-based gas (methane) is passed over the substrate and decomposes due to the elevated temperature resulting in carbon deposition on the surface of the substrate [73]. The advantage of the CVD method is the high quality of the resulting material and low rate of defects. For TMDCs process is similar, but vapour phase reaction occurs with use of oxide precursors [103] and a gaseous chalcogen.

As a subgroup of top-down techniques liquid medium based methods are the ones widely used. Those include Li-ion intercalation, which is a Li-ion insertion into the bulk crystals of starting material. This action causes layer separation, and as a result produces individual layers in the solution. Li-ion method is quantitively very efficient concerning the number of produced monolayers, but the nanosheets are highly defective. Another liquid-based method - Liquid Phase Exfoliation (LPE) produce layered nanosheets in a liquid dispersion. Most commonly in organic solvents[61], [62] but also in water with an additive of stabiliser[36], [105]. Liquid Phase Exfoliation (LPE) is based on solubility parameters. Ideally, a layered material can be taken and immersed in a suitable solvent chosen based on the surface energy of the nanomaterial. In the process, the energy is supplied to the system through the sonication and it must be greater or equal to the nanomaterial surface energy to overcome van der Waals interactions between the layers in the bulk material. When sufficient energy is provided, layer separation occurs, and a range of mono-, bi- and multi-layered nanosheets are dispersed in the solvent[43], [49], [72], [74]. The methodology can be used not only for graphene but also for other materials like TMDCs (h-BN, TMDs, TMOs and layered III-VI semiconductors), BN or BP. Also, solvents (like NMP, CHP) are not the only option to stabilise the dispersion. It can be achieved as well with the use of surfactants[10], [74], [105], [106] or polymers [5] present in the system. The main strength of the LPE method is the flexibility of post-processing material after exfoliation due to the variable choices of the medium and transferring options. Also, quantitively speaking, the method can be scaled up to industrial levels of the output material. [18]

1.5 Dispersion Theory

1.5.1 Introduction

Solubility theory, solution thermodynamics as well as Hansen parameters used through the experimental parts of this thesis will be introduced. They were used to determine suitable exfoliation media to produce stable dispersions of nanosheets in solution. Since the prepared dispersions are desired to be stable over long time periods, the surfactant stabilisation will be described.

1.5.2 Solubility Theory, Solution Thermodynamics & Hansen Parameters

Solubility is a physicochemical property of any solid, liquid or gas. It is a physical property described through solubility parameters to depict chemistry of mixing process between material and solvent [5]. Mentioned parameters were introduced based on a thermodynamic model by Hildebrandt and Hansen and later on called by his name as Hansen parameters of solubility [5]. It is known that not all the solvents can produce a stable dispersion and it is critical at the beginning to be able to match material and solvent correctly. The match is done based on the surface energies[50], [75]. That is why solubility parameters and solubility theory are a strong basis for the exfoliation process as they are used to determine the solubility of nanomaterials in certain media[43], [82]. A mismatch between solvent and material will result in dispersion collapse, rapid aggregation or immediate sedimentation.

Liquid Phase Exfoliation is a solution based process, where the material is exfoliated via sonication from variable source (sonic bath, sonic tip). It is most often done in organic solvents serving as a medium. To achieve stable material-solvent dispersions, requirements of solubility theory and Hansen parameters must be met. The solution thermodynamics theory says: while mixing two or more of chemical compounds there is a change in entropy (ΔS_{mix}) and enthalpy (ΔH_{mix}) in the system. The interaction is described by Gibbs free energy [83] (ΔG_{mix}) principle which is a function of enthalpy (ΔH_{mix}), entropy (ΔS_{mix}) and temperature (T). To prepare a feasible dispersion, the Gibbs free energy must be negative. At the same time, large positive values of entropy are desired in the system. That is hard to fulfil in the case of 2D nanomaterials as they are very small and stiff causing entropy (ΔS_{mix}) to be low [50]. To balance that drawback the enthalpy of the system (ΔH_{mix}) needs to be minimised. The process is not straightforward and to fulfil thermodynamics of the solution theory, both – solute and solvent – interactions must be considered.

1.5.3 Surfactant Stabilisation

Surfactants themselves are long chain molecules made up of the polar head group and nonpolar tail group. They tend to adsorb on the surfaces they interact with. In the case of 2D nanosheets, the polar head group is orientated towards water medium while the non-polar tail interacts with nanosheets. Surfactants can interact not only with medium or nanosheets but also between each other forming aggregates in solution. Accumulation of mentioned aggregates is reducing energy in the solution. This happens when the hydrophilic groups are directed towards the water, and hydrophobic tails towards the centre of surfactant sphere. In the described configuration, the interaction between nonpolar tail groups and water is minimised. Aggregates of that type are called micelles and are formed at specific conditions, when the surfactant concentration reach critical micelle concentration (CMC) [36]. The geometry of formed micelles depend on the kind of surfactant used as well as on temperature and pH of the solution. Micelles might take variable shapes from spheres through ellipsoids, cylinders, or inverted micelles. In this thesis work, there is no exfoliation done in a solvent. Instead, water is used as an exfoliation medium with an additive of surfactant, here Sodium Cholate Hydrate (SC). It acts as a stabiliser throught coating nanosheets in the dispersion and therefore prevents them from aggregation.

Chapter 2

Methods

2.1 Preparation Methods

2.1.1 Liquid Phase Exfoliation (LPE)

The Liquid Phase Exfoliation (LPE) method [92] was used as the principal technicque for the separation of single, few and multi-layered nanosheets of WS_2. To prepare the WS_2 dispersions, probe sonication was applied to powdered WS_2 (Sigma Aldrich) immersed in an aqueous surfactant (Sodium Cholate Hydrate, Sigma Aldrich) solution. The mixture was placed in a metal beaker under cooling at 4 $\circ$C. It was then sonicated using a flathead tip probe (Sonics VX-750) in two sonication steps, with a centrifugation step in between. The first sonication step was for a duration of 1hr, pulsed at 4 s on and 2 s off with an amplitude of 60% and served as initialisation of powder exfoliation. The subsequent centrifugation step (2 hrs at 6 krpm) was performed with a Hettich Mikro 220R centrifuge and served as a cleaning step of pre-exfoliated material. The supernatant containing impurities was discarded and the sediment re-dispersed in a fresh aqueous surfactant solution (SC). This was subjected to a second sonification using the same solid flathead tip probe for 5 hrs, at

60% amplitude and pulsed at 4s on and 4s off resulting in dispersion of polydispersed nanosheets.

2.1.2 Sedimentation Process & Size-Selection Methodology

Liquid Phase Exfoliation (LPE) results in a polydispersed final dispersion. There are both stable and unstable species in its volume. The stable species consist of small and large nanosheets stabilised by the solvent or presence of a surfactant. The unstable constituents are either unexfoliated residue of the material or exfoliated, but aggregated nanosheets. The unstable, unexfoliated and aggregated species are undesired in the dispersion and sediments with time. This process can be accelerated by centrifugation.

Forced sedimentation by centrifugation is a process which is the outcome of balancing environmental forces: the force due to gravity (F_G), the force due to buoyancy (F_B) and the force due to viscous drag (F_D). All the forces experienced by the particle can be expressed by physical laws and equations.

- the force due to the gravity can be expressed by Newton's 3^{rd} law of motion
- the buoyant force is described as the weight of the fluid displaced by the volume of each particle when it is immersed in a liquid
- the force due to viscous drag is described as the force exerted on particle moving through the fluid. It can be explained by Stokes law, which describes the frictional force acting on the interface between the fluid and the particle

Summarising, while the particle is in the liquid medium it will experience a downward force (*gravity*) and an upward force (*buoyancy*). When the particle density is greater than the density of the surrounding medium, it will start to fall towards the bottom of the vial. The time it takes a particle to reach the bottom of a vial, therefore to travel certain distance depends on the viscosity and density of the fluid, and density of the dispersed material.

It is critical to have in mind that the described, simplified theory is based on particles of spherical shape and it is taken as an approximation in this thesis. In practice, centrifugation is used in this work for the separation of the nanosheets by their mass rather than volume.

In experiments:

To select nanosheets by size, Liquid Cascade Centrifugation (LCC) was performed with the use of a Hettich Mikro 200R centrifuge at 13 ∘C with subsequently increasing rotation speeds. Two rotors were used depending on the rotational speed needed. For speeds $\leq$ 5 krpm a fixed angle rotor 1016 (RCF=106.4*f^2) was used with four 28 ml glass vials filled up to 10 ml each. For speeds $>$ 5 krpm a fixed angle rotor 1195-A was used with 1.5 ml vials (RCF=97.4*f^2).

To size select the polydisperse nanosheets produced using LPE, the following procedure was applied. The unexfoliated WS_2 was removed by centrifugation at 1.5 krpm for 2 hrs. The supernatant was subjected to further centrifugation at 2 krpm for 2 hrs. The sediment was collected in fresh surfactant at the volume reduced to 4 ml, while the supernatant was centrifuged again at 3 krpm for 2 hrs. Again, sediment was collected, and supernatant further centrifuged for 2 hrs at a rotational speed of experimentalist choice.

2.2 Characterisation Methods

2.2.1 Absorption Spectroscopy (Absorbance & Extinction)

Absorption spectroscopy is based on the absorption of light passing through the material and results in the promotion of an electron to a higher energy level within the material. It provides information on the band structure of the investigated material.

Spectra usually consist of broad bumps rather than sharp peaks or lines, which are the sum of not only electronic transitions but also vibrational and rotational transitions. In other words, when a photon has energy higher than needed for an electronic transition, then an excess of the energy is used towards vibrational or rotational transitions. In addition to this, nano crystals of materials exert forces on each other while being in solution, and this can alter the energy levels and blur spectral lines into the often observed bands.

The absorption spectroscopy technique is based on the Beer-Lambert Law, which states that the absorbance of the substance in the solution is directly proportional to the concentration and the path length of the cuvette. Transferring this theory into a measurement in the UV-Vis spectrometer, data from the spectrometer might be presented as Transmission (T) or Absorbance (A) and can be explained by one of the equations (Equation 2.1, Equation 2.2) below.

$$A = \log_{10}(I_0 \div I) = \log_{10}(100 \div T) = k * c * l \tag{2.1}$$

$$T = \exp(-\alpha * L) \tag{2.2}$$

where:

I_0 – the intensity of the incident radiation,

I – the intensity of the transmitted radiation,

I/I_0 – the transmittance (T) - often presented in %,

A – absorbance,

L – path length of the sample,

c – the concentration of the solution,

k – extinction coefficient (constant for the material, depends on the wavelength of the radiation and nature of the molecule)

T – the transmission of the sample

α_0 – the linear absorption coefficient

In a typical UV-Vis spectra (taken for gases, crystalline solids or molecules in a liquid), absorption is usually dominated by extinction process. When the particles inside our liquid medium are dimensionally comparable to the wavelength of the light passing through, the scattering contribution becomes more significant and must be considered. The lateral size of nanosheets considered in this work is in the range of 35 nm – 2 μm. This overlaps with the range of wavelengths where absorption spectroscopy is measured (200 – 800 nm), what implies that scattering process is observable. To distinguish both cases "*absorption*" will be used for purely absorption processes and "*extinction*" when scattering has a contribution.The relationship between the two is described as extinction being equal to the sum of absorption and scattering.

All three components of optical spectroscopy are useful and necessary to fully characterise 2D nanoflakes. They allow us to observe changes in the positions and shapes of spectroscopic features, which change together with the lateral dimensions and thickness of nanosheets[1], [76].

In experiments: Optical extinction was measured in quartz cuvettes with a path length of 0.4 cm in 1 nm increments. Extinction spectra were measured in a standard UV-Vis spectrometer (Varian Cary 500) in quartz cuvettes with a path length of 0.4 cm in 1 nm increments. Absorption spectra were measured in an integrating sphere, which collects both transmitted light (extinction) and the light which is scattered (scattering). Knowing that extinction is the sum of scattering and absorption processes, the absorption could be easily calculated by subtracting the scattering from the extinction. [21]

2.2.2 Photoluminescence Spectroscopy

Photoluminescence (PL) was first observed in 1560 by B. de Sahagun [13] and then reported by N. Monardes. Photoluminescence is observed as the spontaneously emitted light after the material has been previously excited. As a result of excitation, electrons are transferred from their ground states into excited states.

Since then, they are no longer in equilibrium and may undergo various relaxation processes like radiative transitions, non-radiative transitions or a combination of radiative-non-radiative transitions. In the case of radiative decay, photons are being emitted. These can be a measurable characteristic for the observed transitions. For semiconducting TMDCs (WS_2 belongs to that subgroup) the origin of PL is the recombination of the electron and hole in the bound state (exciton and trion). For TMDCs, PL measurement is a non-invasive way to determine the optical bandgap of the material.

Semiconducting layered materials go through a transition from indirect bandgap to direct bandgap as they go from bulk to monolayer materials. For the monolayers, which have a direct bandgap, the light emission yield is a few orders of magnitude higher than one corresponding to bi- tri- and few layers. Thanks to this dependence, photoluminescence is a powerful tool in the process of identifying monolayers and their content in a dispersions.

In experiments: Photoluminescence excitation-emission maps were measured in quartz cuvettes using an Edinburgh Instruments FS920 PL spectrometer equipped with a Xe lamp (450 W) and S900 photomultiplier tube detector at room temperature with a single monochromator in excitation and emission. A typical measurement was taken with bandwidths of 3-5 nm and acquisition times between 0.3-0.5 s. To eliminate artefacts a 550 nm cut-off filter was placed on the emission side.

2.2.3 Raman spectroscopy

Raman Spectroscopy is broadly used to study vibrational, rotational and other low-frequency modes to characterise various types of materials from drugs to semiconductors. The process underlying the Raman Spectroscopy technique was discovered and described by Sir Chandrasekhara Venkata Raman in 1928 and is named after him. For that discovery, he was awarded Nobel Prize in physics two years later.

Raman Spectroscopy is based on the scattering process of photons passing through the medium. That could be either: elastic scattering (when photons preserve their energy) or inelastic processes (when photons exchange their energy with the medium they pass through). Since lattice oscillations depend on the material's crystal structure, atomic mass and its position in the unit cell, the type of interatomic bonds as well as the energy difference between incident and scattered photon (phonon energy), this technique carries lots of information about the material. While Raman scattering provokes a shift in the energy of incoming photons, the narrower the spectrum of incident light is the higher outcome energy resolution we can achieve. Based on the final photon energy compared to its initial energy there are two types of scattering. Stokes scattering - when there is an energy loss, and anti-Stokes scattering - when there is an energy increase. In both cases, the spectra are symmetric and give the same information.

The Raman spectroscopy technique is a powerful tool for 2D nanomaterials characterisation. As reported in the literature, WS_2 for instance, changes its crystal lattice vibration with a decreasing layer number [47]. These changes can be well tracked and observed on Raman shift spectra. An additional advantage of Raman spectroscopy in 2D nanosheets characterisation is that while the material is being excited at or above its resonance, the spectra consist of a contribution due to photoluminescence (PL).

This is known to be emitted only from monolayers, while the Raman signal comes from all multi- bi- and monolayers. That relationship is used to extract quantitative information on the volume fraction of monolayers [1].

In experiments: Raman/PL spectroscopy was performed on the liquid dispersions using Horiba Jobin LabRAM HR800 with 532 nm excitation laser in air, under ambient conditions. The Raman/PL emission was collected by a 100x objective lens and 10% of laser power (about 2 mW). It is crucial to take great care during the measurement as any change in the focal plane during acquisition may introduce an error. This may result in a tilted baseline or asymmetric PL or even visually, when the laser spot shape changes during the measurement. To enable reproducibility, the following procedure was applied: a 20 μL drop of high concentration WS_2 dispersion was placed on a glass slide, and the drop edge was focused with a 10x objective. Then it was refocused again with 100x objective at the same spot and readjusted, so the focus was slightly above the drop. It is important to take measurements closer to the edge than to the centre of the droplet as the lower curvature means the focus stays constant. An average of 5 measurements were taken. Acquisition times were kept as short as possible (2-10 s) and were dependent on dispersion concentration.

2.2.4 Transmission Electron Microscopy (TEM)

Transmission Electron Microscopy (TEM) is a technique which serves to investigate the quality and morphology of nanomaterials [51]. It is widely used to characterise nanosheet dimensions as well as the quality of materials. TEM images presented in this thesis were acquired with use of bright field TEM and let us assess the nanosheets produced via the liquid phase exfoliation method quantitatively.

In TEM microscopy, an electron beam is used to create an image of the sample. The beam itself is set up by guns of two types: field emission (Schottky, Cold FEG) or thermionic (W, LaB_6). The electron beam travels down the column and interacts with the sample. As a result, some electrons are being scattered at a given angle about the normal angle of the incident beam. Since the distance between electrons in the electron beam at 100 kV is about 0.15 mm, we consider the interaction between beam and sample as a single electron event. The beam is being focused through selective area aperture. Depending on the focal plane position, the TEM can be operated in diffraction or imaging mode. Diffraction mode is enabled by use of back of the focal plane of the intermediate and projection lenses and brings up the information on either the crystalline or amorphous structure. For well exfoliated thin nanosheets, a characteristic diffraction pattern will be observed. If there are some contaminations, a diffuse crystalline cloud would be observed. Diffraction patterns could also serve to detect monolayer nanosheets via their corresponding theoretical patterns.

In experiments: When the nanosheets of interest were isolated from the standard dispersion via the size selection method, the sample was deposited on a TEM grid by multiple drop casting of the dispersion over the surface of the grid.

The choice of the TEM grid type itself is important for TEM statistics and depends on the expected mean size of nanosheets in the investigated dispersion. When the majority of the nanosheets are assumed to be large, then the holey carbon grid is used. It consists of a stretched layer of carbon pulled over the supporting structure, enabling solvent to leak over the grid and only nanosheets to be left on the grid surface. In the other case when the nanosheets are expected to be small, then the continuous carbon film is used as a substrate for TEM imaging. It keeps all sizes of nanosheets on the surface but needs to be handled with care during deposition to avoid aggregation or washing the nanosheets away.

2.2.4.1 Statistical TEM analysis

For statistical TEM analysis, low-resolution TEM has been used to quantitatively analyse the quality, mean length and the distribution of nanosheets dispersions produced by Liquid Phase Exfoliation. All the low-resolution TEM was performed on a Joel 2100 operated at 200 kV using LaB_6 filament.

After the grid was appropriately prepared, actual TEM images were taken with statistical analysis in mind, so to be able to statistically work out the mean length and width of nanosheets in the sample. This is achieved by randomly picking spots on the grid and imaging minimum of 200 flakes. When a random representation of nanosheets was imaged, the statistical analysis can be performed. To extract numbers for "length" and "width", images are opened with ImageJ software and lines are drawn along the long side of nanosheets for "length" and along shorter sides for "width". Considering the imaging magnification scale, corresponding readings are taken and then statistically analysed giving the mean length and width of a representative flake in the sample together with the standard deviation for each dimension.

Using analytical TEM was very important in this thesis as it allows us to determine the mean geometry of the nanosheets produced via Liquid Phase Exfoliation. The information taken from here might be useful for scattering component correlation and AFM dimensional analysis correlation.

2.2.5 Atomic Force Microscopy (AFM)

Atomic Force Microscopy (AFM) is a powerful characterisation tool for 2D nanomaterials as it gives information about the nanosheets geometry and quality. Unlike other microscopic techniques, it is not based on electromagnetic radiation but measures vertical displacement of the tip as it moves along the sample surface and creates a topological profile of the nanomaterial.

The tip movement across the surface of the sample is detected by a laser, which is being reflected from the back side of the cantilever and then it is focused on a photodiode. There are two modes which AFM can operate: contact and non-contact mode. The choice of the mode depends directly on the sample to be measured and its properties. The process of the interaction between the tip and specimen is described by the Lennard-Jones potential, where the interaction is described as a function of tip-sample distance. While in operation, the cantilever is usually no more than a few Angstroms from the surface. The main force of the interaction is repulsive as the tip is following the topography of the surface of the sample. In the non-contact mode, the cantilever is further away than in contact mode (about a few hundred of Angstroms). In so-called tapping mode, the tip oscillates at its resonant frequency and slowly profiles the surface as it moves across. Normally, atoms are weakly attracted to each other, but when the distance separating the tip and the specimen decreases, the attraction increases. In another case, while the separation is close, the electron clouds start to overlap and repel each other. At this stage, any decline in separation will result in sample deformation caused by the van der Waals forces that create the direct deflections and oscillations of the cantilever due to attractive or repulsive interactions. This is all converted into a topographic map of the sample which is of our interest.

In experiments: WS_2 nanosheet dispersions were diluted with deionised water and drop casted (10 μL) on preheated (150$\circ$C) Si/SiO_2 wafers (0.25 cm^2) with an oxide layer of 300 nm. After deposition, wafers were rinsed with deionised water and dried with compressed air prior to measurement to remove excess surfactant and to dry adsorbed water residues. The location of the imaging was not arbitrary, but regions with low density were determined as ideal for acquiring reliable information and to avoid aggregates common around “coffee-stain”-like structures.

AFM imaging was carried out on a Veeco Nanoscope – IIIa from Digital Instruments. An E-head in tapping mode was used for all measurements and the typical image size taken was $8x8$ μm for overview images and $4x4$ μm for zoomed in images with 512 lines per image and scan rates of 0.8 Hz. Measured thickness was converted to a number of layers based on conducted step height analysis. AFM was used to get information on the geometry of dispersed WS_2 nanosheets, especially thickness and the effective number of layers,$< N >$.

2.2.5.1 Statistical AFM analysis

After a sufficient number of images were taken to generate a reasonable minimum of 200 flake readouts of numbers corresponding to "length" and "width", images were opened with Gwydion software. Similarly, to TEM statistical analysis, lines were drawn along the long side of nanosheets for "length" and along shorter sides for "width". Along with the lateral nanosheet's parameters height profiles were extracted from drawn lines. Based on a sufficient number of values collected for "length", "width" and "thickness" and statistical calculations, mean length, width and thickness of a representative flake in the sample were determined. Following this, the number of layers value was evaluated based on step height analysis and measured thickness value.

2.2.5.2 Step Height Analysis

As the apparent AFM heights from LPE nanomaterials are usually overestimated (due to a residual solvent or surfactant) to overcome that issue the apparent measured AFM thickness is converted to the number of layers. This involves measuring the height of the steps associated with the traces of partially exfoliated nanosheets on the nanosheet surface. For reliable results a minimum of 60 counts must be taken. The apparent height of the step is always a discrete value which represents the apparent height of one monolayer seen by the AFM. For WS_2 it was estimated to be 1.9 nm.

2.2.6 Nonlinear Optical Transmission

Nonlinear optical materials are interesting for applications and the production of photonic devices. They can be used to control the amplitude gain or extinction, polarisation, phase, reflection and refraction of light. Many of 2-Dimensional materials are believed to exhibit such properties. Some reports on TMDCs showed that for the monolayers, second harmonic generation (SHG) is strongly enhanced [52]. The LPE WS_2-Polymer composites has been already used as saturable absorvers in Optical fiber lasers [19]. This is why WS_2 is investigated in this thesis toward nonlinear effects.

Nonlinear effects might be numerically described through nonlinear parameters like the nonlinear absorption coefficient (β_{eff}) [93]. Based on the value of β_{eff}, the process might be classified as: saturable absorption when [$- \Delta\ \beta_{\text{eff}} < 0$] or as an optical limiting when [$- \Delta\ \beta_{\text{eff}} > 0$].

2.2.6.1 Optical Limiting (OL)

There are two mechanisms that explain the nature of the optical limiting process [12]. One is that particles in the dispersion heat up while absorbing the light, which makes them ionise and produce microplasmas while vaporisation temperature is reached. These so called microplasmas scatter further incident light. Another known mechanism is that dispersed nanosheets are first to absorb heat from the incident light and then when they can not absorb any more the excess is transfered to the surrounding solvent. First, localised regions of lower refractive index are getting hotter. The heating creates bubbles which scatter the light incoming to the specimen. Through this mechanism, optical limiting occurs below the vaporisation temperature of the nanosheets.

A good optical limiting material should exhibit high linear transmission for inputs of low energies but low transmission for high energy inputs, so that it may work as a protective film that filters too high energies. Thanks to this optical property, limiters are widely applicable in protective eyewear and laser protective sensors.

2.2.6.2 Saturable Absorption (SA)

Saturable absorption is a property, where the absorption of light decreases with increasing light intensity. As it is a high energy process, it exists when a sufficiently high incident light intensity is provided. It is a balanced process consisting of both absorption and stimulated emission [94].

When light passes through a medium it is attenuated according to Beer-Lambert's law. The fraction of absorbed light depends on the absorption coefficient. Absorption coefficient is in the simplest case dependent on the number of electrons available to absorb photons and on the amount of available states in the higher level of the transition. If the incident light is resonant with a transition where there is a limited amount of states (either electrons in the lower transition states or available states in the higher transition level) a fraction of that light will be absorbed. If the intensity of the incident is increased till the transition‘s ground state is fully depopulated (or the higher transition‘s state fully populated) the material won't be able to absorb more photons. Then the absorbed light will be a lower fraction of the incident light as its intensity increased. This is known as saturable absorption process of 100% Transmission, and 0% absorption so called as Saturable Absorption (SA). Saturable absorbers are used in laser cavities and for passive Q-switches [6]. The key parameters for a saturable absorber are its wavelength range, dynamic recovery time, saturation intensity and fluence.

2.2.6.3 Z-scan Technique

The development of optical limiters began the search for materials with fast and strong nonlinearities. The promising materials can be distinguished from others by the measurement and comparison of the nonlinear refractive index and nonlinear absorption coefficient.

The Z-scan technique, for which the name originates from the z-axis translation stage where the sample is usually placed, is widely recognised as one of the simplest and most reliable methods to extract information about the nonlinear optical properties of materials. Its simplicity and low maintenance costs made it a standard technique for measurements of such properties as the nonlinear absorption coefficients or nonlinear refractive index. In the majority of cases, one can obtain these parameters directly from Z-scan collected data. The main advantage of the Z-scan technique is the ability to get information on the nonlinear optical behaviour of the sample based on measurement of optical energy in the far field.

In Open Aperture (OA) Z-scan configuration, the nonlinear absorption coefficient can be obtained. In this setup, the transmittance of the sample is measured through the open aperture as the function of z-position while the sample is transported through the z-distance with time- and length-wise specified steps. Measurement progresses from the low-intensity regime through high intensity at the laser focal point to a low-intensity regime again. The distance itself depends on pulse parameters and sample thickness. In theory, scanning in a range ± z_0 (the Rayleigh length, Equation 2.3), is sufficient, but for thicker samples a distance of $\geq 5\ z_0$ is preferable.

$$Z_0 = \frac{\pi * \omega_0^2}{\lambda} \tag{2.3}$$

where:

λ – wavelength

ω_0 – beam waist

During the measurement, an open aperture (OA) detector is placed at the end of the optical line and detects changes in intensity as the sample is moved through the focal point of the laser beam. When the optical losses such as scattering or absorption occur, plots of transmission intensity vs the z-position of the sample exhibit bell shape curves, with the minimum transmission at the focus point of the beam. For practical reasons, when fluctuation of the laser power during the scan is observed a second reference detector is introduced into the system.

In experiments: The nonlinear optical measurements presented were performed with the home build open-aperture (OA) z-scan system geometry. This consisted of a Minilite II laser source, reference detector (RD) and open aperture detector (OAD), a beam splitter, two focusing lenses and a z-axis movement stage for sample holding.

The laser source used in nanosecond (ns) timescale experiments was Minilite II, with a pulse duration of 6 ns and repetition rate set at 10 Hz. The laser was operated at 532 nm wavelength. All the samples have been measured in quartz cuvettes with a 1 mm path length. Samples linear transmission was fixed at 80%. For the femtosecond (fs) time scale experiments, the same z-scan setup geometry (section 4.2, Figure 4.1) was used with the laser source of 340 fs, 100 Hz mode-locked fiber laser operating at 520 nm wavelength.

The computer controlled system was designed and built especially for the need of the experiments. The software written in LabVIEW allows for detailed control of the number of pulses averaged per data point, movement distance step, start and end point and also control of the intensity of the signals being read on both detectors.

Chapter 3

WS_2 – High-Quality Liquid Exfoliated Nanosheets

3.1 Introduction

The inexpensive and reliable method of producing and processing 2D nanomaterials [7] in the liquid phase[53], [92] opened wide doors for promising 2D materials with still growing range of possible applications like composite materials, sensors, energy storage and flexible electronics [63]. The possibility of on demand lateral dimensions[21], [101] and controllable morphological properties at the nanoscale made liquid phase exfoliation an important technique giving access to a variety of nanostructures in relatively large, upscalable quantities. The mentioned Liquid Exfoliation Method (described in detail in subsection 3.2.1) involves sonication of layered crystals in a liquid, which, if appropriately chosen, will stabilise nanosheets against aggregation.

Despite significant progress, nanosheets produced in the LPE process are still very polydispersed in lateral size and thickness which is a bottleneck for the production of high-performance devices for which uniform material is required. Monodispersed material properties are more predictable and controllable what is a must in real life applications. To meet that challenge, several size selection procedures have been developed. The simplest one being homogeneous centrifugation, another density gradient centrifugation and lastly liquid cascade centrifugation [1] used in work presented in that thesis. All the above methods were described in section 3.2.

3.2 WS_2 Dispersion Preparation

3.2.1 WS_2 – Liquid Phase Exfoliation

The WS_2 dispersion was prepared by the Liquid Phase Exfoliation (LPE) method described in detail in subsection 3.2.1 by probe sonicating the WS_2 powder. In the experiment, 20 g/L of WS_2 powder was immersed in 80 ml aqueous solution of sodium cholate (SC) acting as a stabiliser, with a concentration of 6 g/l. The mixture was placed in an ice cooled metal beaker. A flathead sonic tip (Sonics VX-750), which was immersed in the dispersion, lowered to the bottom of the beaker and then raised about 1 cm above the bottom.

The mixture was sonicated under constant ice cooling for 1hr at 60% amplitude and pulse of 4s on and 2s off. After the procedure was finished, the dispersion was transferred from the metal beaker into six glass vials and centrifuged for 1.5 hr at centrifugation speed of 6000 rpm. The supernatant of the centrifuged dispersion containing impurities was discarded and the sediment redispersed in fresh surfactant (SC) aqueous solution with a concentration of 2 g/l. The new dispersion was transferred again into a metal beaker and subjected to a second, longer sonification. Again, the flathead tip was used as a sonication probe. Typical sonication times were 5 hrs at 60% amplitude with pulse of 4 s on and 4s off, all under ice cooling.

The final dispersion produced in that two step sonification procedure is a polydisperse WS_2 in aqueous dispersion of Sodium Cholate Hydrate (SC), which is a surfactant acting as a stabiliser (subsection 1.5.3). It is a starting point dispersion for all the post processing and characterisation which will be further described in this thesis and referred to as "stock" dispersion.

3.2.2 WS_2 – Size Selection

As the *"stock"* dispersion produced in the exfoliation process is highly polydisperse, Liquid Cascade Centrifugation (LCC) was applied to select nanosheets by size. The multi-step centrifugation was performed with iteratively increasing centrifugation speed. After each step, supernatant and sediment were separated, the sediment collected and the supernatant subjected to centrifugation at higher speeds than the pevious one. It is presented schematically in Figure 3.1.

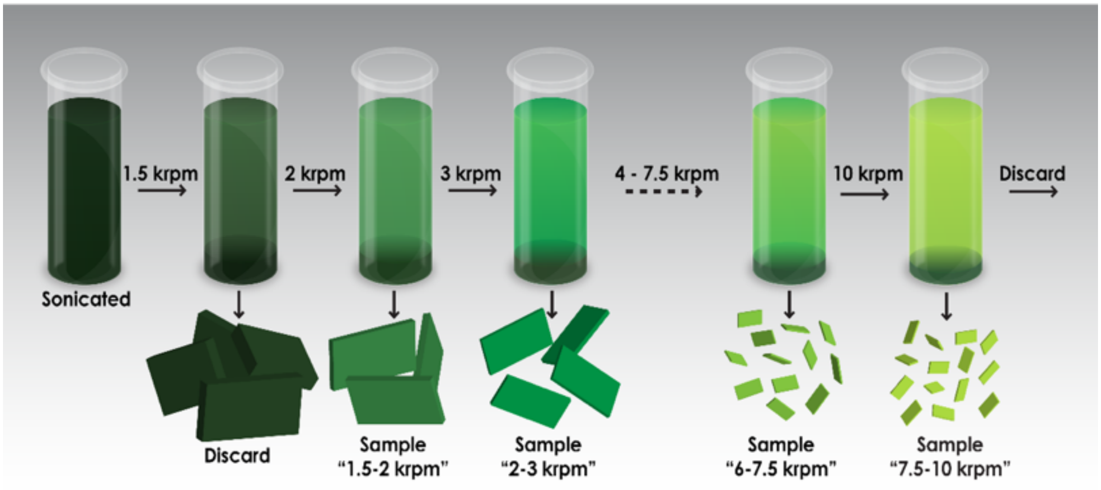

Figure 3.1: Schematic describing the basic centrifugation cascade employed in this study. Size-selected nanosheets are collected as sediments. Each sediment is collected or "trapped" between two centrifugation speeds.

The *"stock"* dispersion was transferred equally into four glass vials and centrifuged for 2 hrs at 1500 rpm. The sediment, being mostly unexfoliated WS_2 powder, was discarded and the supernatant collected and further referred to as a *"standard"* dispersion. The *"standard"* dispersion is still dimensionally polydisperse but contains only single and multilayer nanosheets and no bulk material.

The "*standard*" dispersion was taken into the Liquid Cascade Centrifugation, which produced WS_2 liquid dispersions with relatively narrow size distributions which were characterised in depth in this thesis. To start the LCC, the "*standard*" sample was transferred equally into four glass vials and centrifuged for 99 minutes at 2 krpm. The sediment was collected in fresh SC (1 g/l) solution and labelled as "*standard-2k*" while the supernatant was again equally transferred into four glass vials and again centrifuged for 2 hrs at 3 krpm. Again, the sediment was collected and labelled as "*2 - 3k*" and the supernatant was subjected to another 2 hr centrifugation at a higher speed of 4 krpm. This procedure was repeated for speeds 5 krpm, 6 krpm, 7.5 krpm, 10 krpm, 15 krpm and 18 krpm. For speeds above 7.5 krpm, 1.5 ml Eppendorf vials were used instead of 4 glass vials in the procedure.

The LCC based size selection process produced seven reasonably narrow size distribution samples of WS_2 dispersions called "*std-2k*", *"2-3k"*, *" 3-4k"*, *"4-5k"*, *"5-6k"*, *"6-7.5k"*, *"7.5k-10k"*. The quality and properties of LPE WS_2 samples produced were further investigated through microscopic, linear and nonlinear spectroscopic characterisation as described in section 3.2, section 4.2 and section 4.3

3.3 Microscopic Characterisation

Nanosheets collected after each iteration of the LCC described in section 3.2 (7 samples) were characterised using both statistical Transmission Electron Microscopy (TEM) and Atomic Force Microscopy (AFM). The representative images for each size are presented in Figure 3.2 (TEM) and Figure 3.3 (AFM).

To quantitatively characterise the samples size selected by LCC dispersions, TEM images were analysed, and the nanosheet length (the longest dimension) was measured for $\sim$ 100 individual nanosheets in each sample over all seven dispersions. Histograms revealing the log normal length distribution of the nanosheets in each fraction are presented in Figure 3.2A-G in this chapter. These histograms show a reduction in nanosheet length as the centrifugation speed increases (so as it progresses through the cascade) as expected.

Similarly, statistical AFM analysis was performed, so length (L), width (W, dimension perpendicular to width) and thickness (T) of nanosheets were measured. The apparent thickness is typically overestimated from the theoretical thickness in AFM on LPE samples due to the presence of trapped and adsorbed solvent and surfactant. It was converted into the mean number of monolayers per sheet <N> (Figure 3.3A-G), by dividing the apparent AFM thickness by the measured thickness of one layer which was determined to be 1.9 nm in the case of WS_2. The value was extracted through step height analysis [21]. By measuring length, width and layer number, volume fractions of nanosheets of a given thickness (for example monolayers) in each dispersion can be determined if the statistics are robust enough. Therefore, in the case of AFM, $\sim$ 300 individual nanosheets per sample were analysed.

The final AFM layer number histograms are shown in Figure 3.3A-G. These histograms follow a log normal trend quite closely. Again, we observe the same trend, as the dispersion goes through the cascade: when the centrifugation speed increases the reduction in nanosheet thickness occurs. The log normal shape of the histogram suggest that in each separated fraction there is a small amount of larger species (histogram tail).

To represent changes in lateral dimensions more clearly, the mean nanosheet length (extracted from both TEM and AFM) is plotted as a function of the centrifugal acceleration (expressed as relative centrifugal acceleration in multiples of the *g*-force) which is associated with the midpoint of the pair of rpms used in each step of the cascade described (Figure 3.4A). The mean nanosheet length falls off as (g-force)$^{-0.5}$ as expected due to the close relationship between <L> and the size of the largest particle remaining in the dispersion after centrifugation.

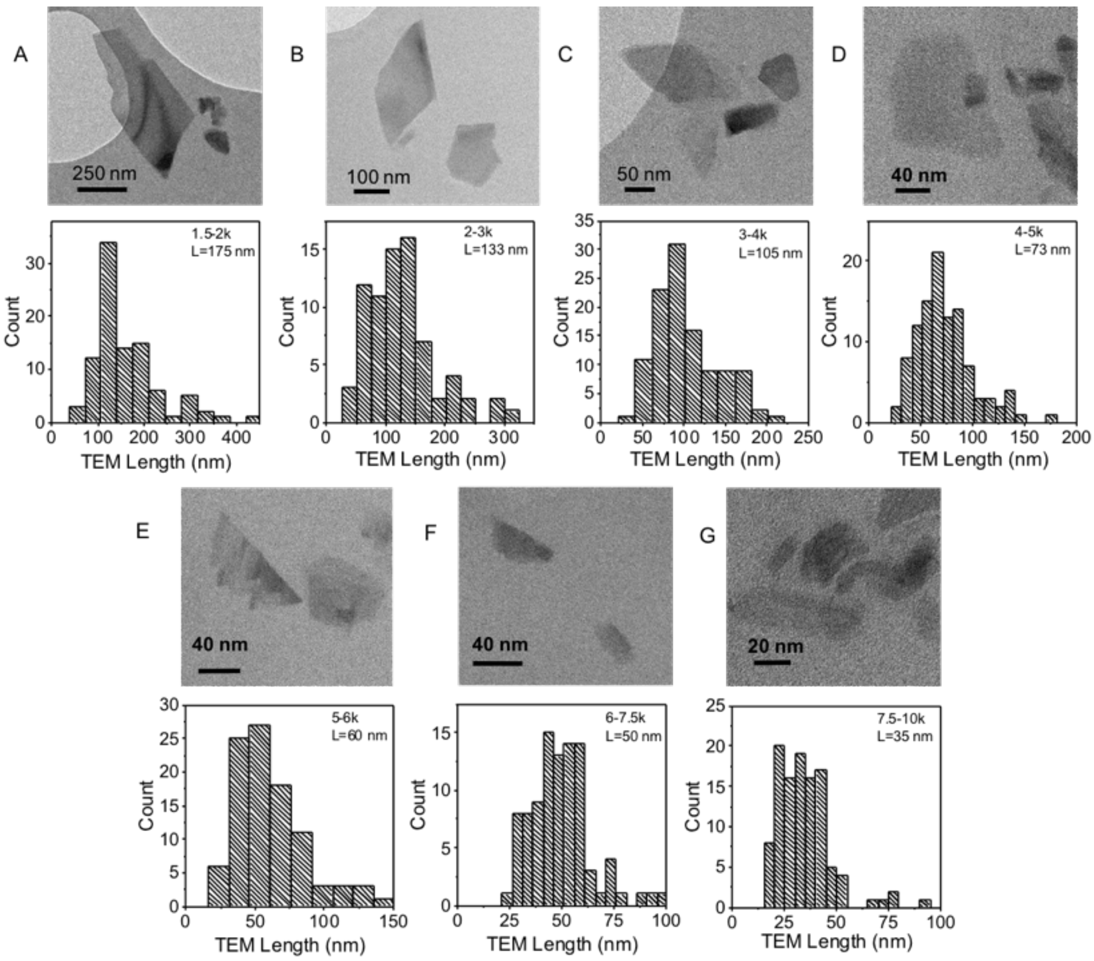

Figure 3.2: TEM images and length histograms of WS_2 samples obtained from the standard LCC. **A-G)** WS_2 dispersed in an aqueous solution of sodium cholate (SC, 2 g/L) after centrifugation between **A)** 1.5-2 krpm **B)** 2-3 krpm **C)** 3-4 krpm **D)** 4-5 krpm **E)** 5-6 krpm **F)** 6-7.5 krpm **G)** 7.5-10 krpm.

Analagous to the length, the mean nanosheet layer number, <N> is plotted vs the *g*-force in Figure 3.4B. The mean number of layers falls with central rotational speed via (g-force)$^{-0.4}$. Based on the set of size-selected samples (fractions 1-7) investigated, it is clear that <L> $\propto$ <N>. That relationship certainly limits the described method. Ideally, one would like to vary <L> and <N> independently as will be addressed in subsequent chapters of this thesis. The mean thickness and produced mass dependence on the centrifugal force are presented in Figure 3.4C-D.

Due to the effects like tip broadening and pixelation, the lateral dimensions mea-

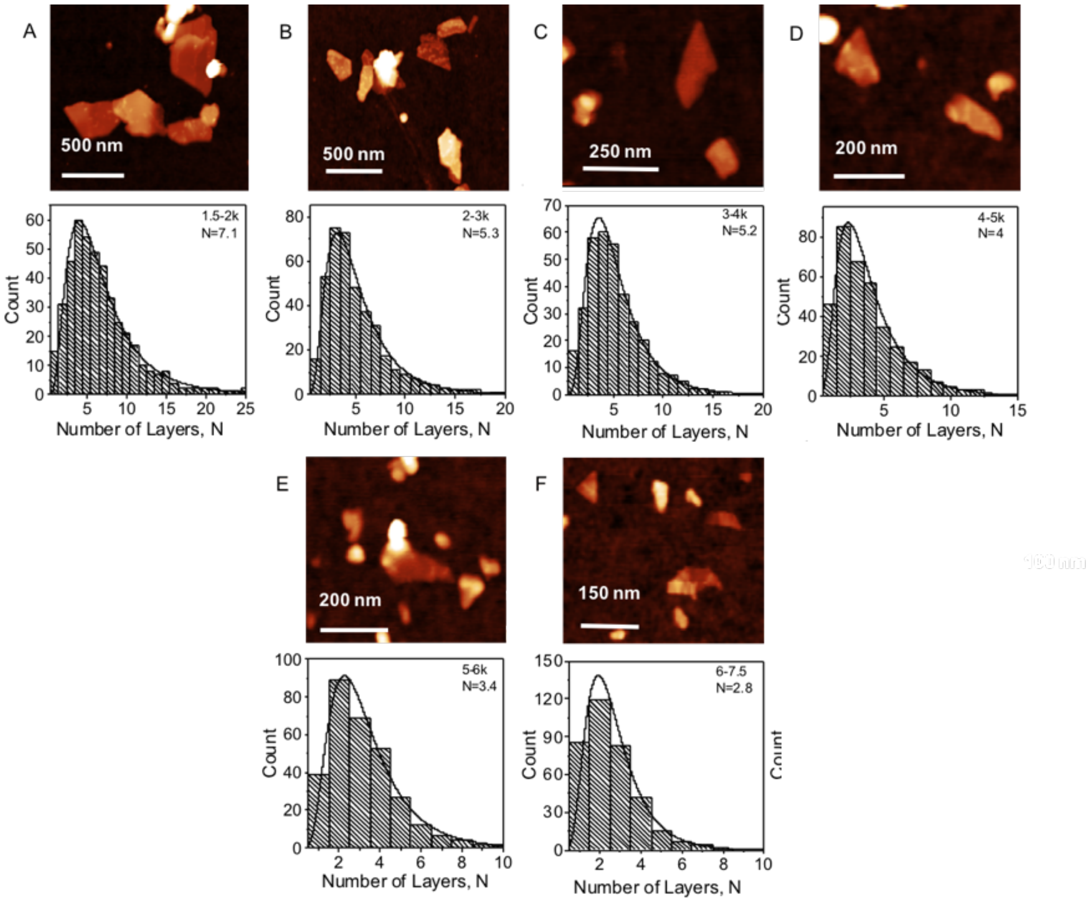

Figure 3.3: AFM images and length histograms of WS_2 samples obtained from the standard LCC. **A-G)** WS_2 dispersed in an aqueous solution of sodium cholate (SC, 2 g/L) after centrifugation between **A)** 1.5-2 krpm **B)** 2-3 krpm **C)** 3-4 krpm **D)** 4-5 krpm **E)** 5-6 krpm **F)** 6-7.5 krpm.

sured by AFM are overestimated. As length was measured from both TEM and AFM images, we were able to correlate values from both methods and correct the lateral dimensions measured by AFM for the rest of the analysis. The correlation is presented in Figure 3.5, where we plot the mean length <L> measured by AFM vs mean length <L> measured by TEM. The data is fitted to a linear function with a slope of 1.21 and intercept of 6 nm. We believe that the slope is due to the pixelation and the intercept corresponds to tip broadening.

The corrected length from AFM measurements $<L>_{corr}$ is related to the measured length $<L>_m$ according to the equation (Equation 3.1):

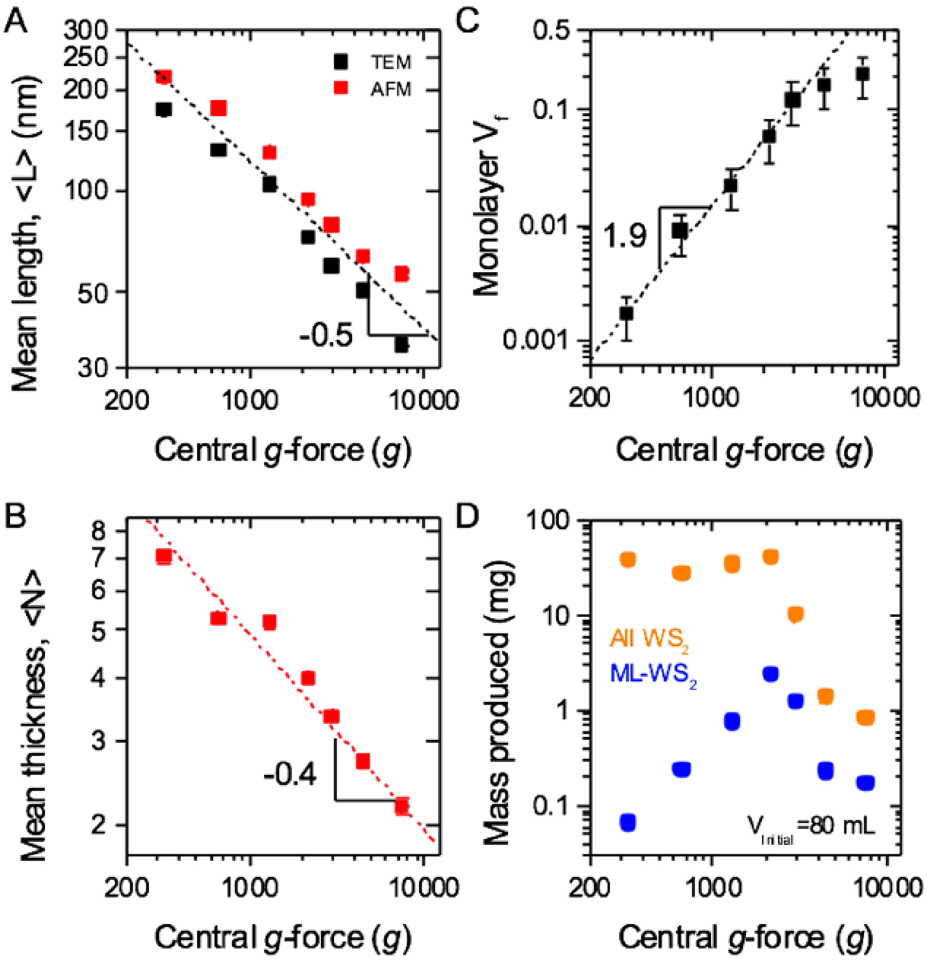

Figure 3.4: Statistically analysed data extracted from AFM and TEM imaging. **A, B)** Data extracted from histograms for a range of centrifugation conditions. Mean values of **(A)** nanosheet length and **(B)** nanosheet thickness as a function of g-forces. **C, D)** Standard deviation of nanosheet length **(C)** and thickness **(D)** vs mean length and thickness respectively.

$$L_{corrected} = L_{measured}/1.21 - 6nm \tag{3.1}$$

This correction equation was applied to all data further presented. It must be noted that it is not a general relation but one related to a specific instrument, scanning parameters and cantilever used.

To investigate the relationship between <L> and <N> in more detail, we plot

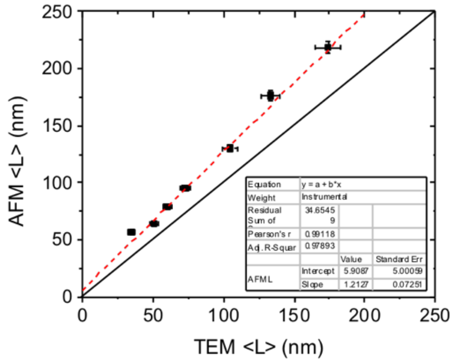

Figure 3.5: Correlation of measured AFM and TEM length.

L as a function of N for each nanosheet measured by AFM in Figure 3.6A. The different colors represent the different fractions after LCC. That plot shows to be consistent with the proportionality of L and N which means that this relationship is likely a fundamental property of LPE nanosheets and not necessarily a result of the centrifugation. Interestingly, for a given sample (e.g., 4- 6 krpm as shown in the inset), the nanosheet length does not vary systematically with thickness.

To explore this more carefully, the mean nanosheet length was extracted for each value of N and plotted vs N for each sample in Figure 3.6B. This shows that for a chosen step in the cascade, the mean nanosheet length is roughly independent of N.

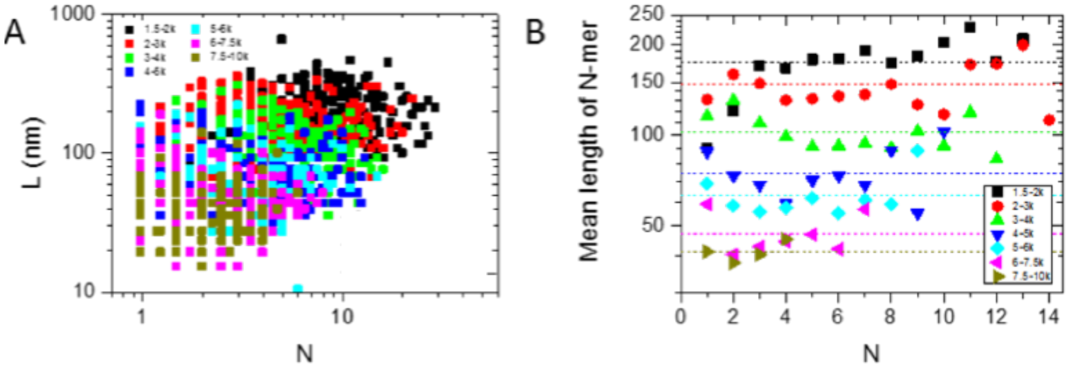

Figure 3.6: Mean length of N-mers from the standard cascade. **A)** Flake by flake nanosheet length vs a number of layers **B)** Corrected AFM mean length of nanosheets with a certain thickness of 1-10 layers vs a number of layers for standard size selected samples

These findings suggest that the described LCC is predominantly a length not mass separation process. Reasons for this are currently unclear, but are likely linked to the fact that the equilibrium in the centrifugation was not reached after the relatively short centrifugation times of 2h in each step. In such cases, back diffusion and friction can play a prominent role and unexpectedly lead to size selection which is not strictly governed by nanosheet mass. This means that centrifugation at lower central g-forces selects larger nanosheets in general, wich also means larger monolayers. To give an example, for the relatively low central g-forces (2-3 krpm sample) the mean monolayer length was as high as 130 nm, with individual monolayers as long as 200 nm observed, while they were typically 40 nm in the fractions isolated at higher centrifugal accelerations (where <N> is as low as 2.2). Unfortunately, these large monolayers are more often found in the low g-force samples, and present only a minority population in the respective high g-force fraction.

Most probably, the monolayer length distribution in the stock is set by the exfoliation conditions (e.g., details of sonication regime and stabiliser, crystallite size). It will be under our investigation in the future to identify conditions leading to potentially larger monolayers).

3.4 Linear Spectroscopic Characterisation

3.4.1 Determination of the Extinction Coefficient.

For MoS_2, it was shown that optical extinction spectra of liquid exfoliated Transition Metal Dichalcogenides (TMDCs) are known to change as a function of size and thickness [3]. It was suggested that the foundation of the changes with length are different extinction coefficients of the nanosheets's basal plane and edge region, respectively [76]. As a result, extinction spectra change as a function of nanosheet size. To test whether this is the case for WS_2, extinction coefficieant spectra were determined for

WS_2 as described below.

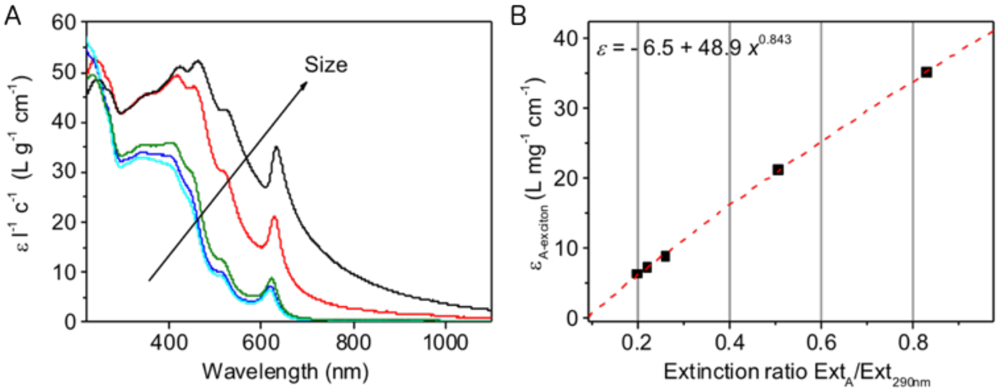

Figure 3.7: Size dependent extinction coefficient. **A)** Extinction coefficient spectra of WS_2 exfoliated in an aqueous solution of sodium cholate for different mean nanosheet sizes and thicknesses. **B)** Extinction coefficient at the A-exciton (~615-620 nm) as a function of extinction peak intensity ratio at A-exciton / 290 nm

We prepared a number of WS_2 dispersions with varying sizes and thicknesses by LCC similar to the procedure described in the methods (chapter 2) and measured the optical extinction spectra. The concentration of WS_2 was then determined by filtration and weighing (alumina membranes pore size 0.02 μm). Before weighing, the samples were washed with 600 ml of deionised water and dried under vacuum at 70 °C. Slightly different centrifugation conditions were chosen (fewer samples, larger spacing between rpms) to maximise the mass and thus reduce the error from the weighing. With knowledge of the volume and mass, the extinction spectra can be converted to extinction coefficient spectra (Figure 3.7A). Similar to MoS_2, they show systematic changes with nanosheet lateral size/thickness.

To express the spectral changes in dispersions with unknown lateral size and thickness, it is feasible to take peak intensity ratios from spectra regions with most prominent changes. In the spectra above, the intensity ratio of the A-exciton (615-620 nm) over the local minimum appears a good choice. In Figure 3.7B, the extinction coefficient at the A-exciton is plotted as a function of the peak intensity ratio. This gives the size-dependent extinction coefficient at the A-exciton which is used to convert the extinction spectra of the LCC dispersions to the respective extinction coefficient.

3.4.2 Optical Extinction Dependence on Nanosheets Lenght

As indicated above and previously demonstrated for MoS_2 [76], the profile of optical extinction spectra strongly depends on nanosheets dimensions. The fractions produced by LCC were used to investigate the effect of nanosheet size and thickness on the optical properties of LPE WS_2 dispersions described in subsection 2.1.1 To do this, we first measured the optical extinction, absorbance and scattering spectra for all seven fractions of WS_2 described in section 3.2.

The extinction coefficients were calculated using the measured mass of dispersed nanosheets as outlined in subsection 3.4.2 (Figure 3.7). Optical extinction spectra of liquid exfoliated WS_2 display the characteristic excitonic transitions and vary systematically with nanosheet size and thickness due to edge and confinement effects in analogy to MoS_2 [44], Similar behaviour was observed for the absorbance and scattering coefficient spectra (Figure 3.8).

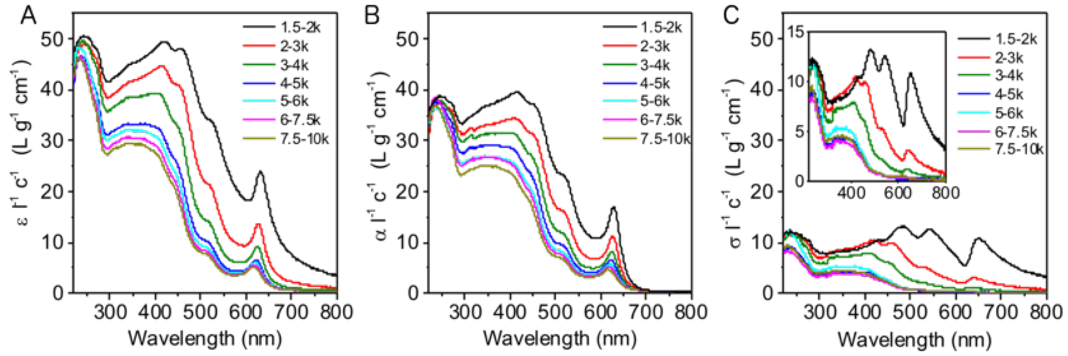

Figure 3.8: Extinction, absorbance and scattering coefficient spectra. **A)** Extinction coefficient spectra of the size selected WS_2 dispersion **B)** Absorbance coefficient spectra **C)** Scattering coefficient spectra

The scattering can contribute significantly to the measured extinction in nanosheet dispersions. This is why true absorbance spectra were acquired by measurements in an integrating sphere as described in subsection 2.2.1. The scattering spectra were calculated as *Extinction - Absorbance.* Positively, for these nanosheet dispersions the absorbance and extinction spectra are very similar making scattering a minor contributor (Figure 3.8). This is because scattering spectra follow absorbance spectra in shape in the resonant regime, and indicates scattering coefficients are lower than absorbance coefficients.

The size dependent spectral changes are presented on Figure 3.9A. It was observed that the extinction coefficient, for example at the A-exciton (~620 nm), depends strongly on nanosheet length as shown in Figure 3.9B. However, the extinction coefficient at 235 nm is invariant with nanosheet length making this ideal to determine the nanosheet concentration via $\varepsilon_{\mathrm{235nm}} = 47.7\ \mathrm{Lg^{-1}cm^{-1}}$ and the Lambert Beer law.

The effect of edges on the spectral shape can be quantified by the ratio of extinction intensities at two different wavelengths. In principle, any peak intensity ratio can be chosen. However, in WS_2, we found the ratio of 235 nm and 290 nm, $\mathrm{Ext_{235}/Ext_{290}}$, to yield reliable changes across various samples. It is presented in Figure 3.9C and can be fitted to the following equation:

$$\frac{Ext_{235}}{Ext_{290}} = \frac{\alpha_c(235nm)L + 2x(k+1)\Delta\alpha(235nm)}{\alpha_c(290nm)L + 2x(k+1)\Delta\alpha(290nm)} \tag{3.2}$$

where:

α_C – the absorption coefficient associated with the nanosheet basal plane,

$\Delta\alpha = \alpha E - \alpha C$, where αE is the edge region absorption coefficient,

L, x and k are the nanosheet length, edge thickness and aspect ratio, respectively

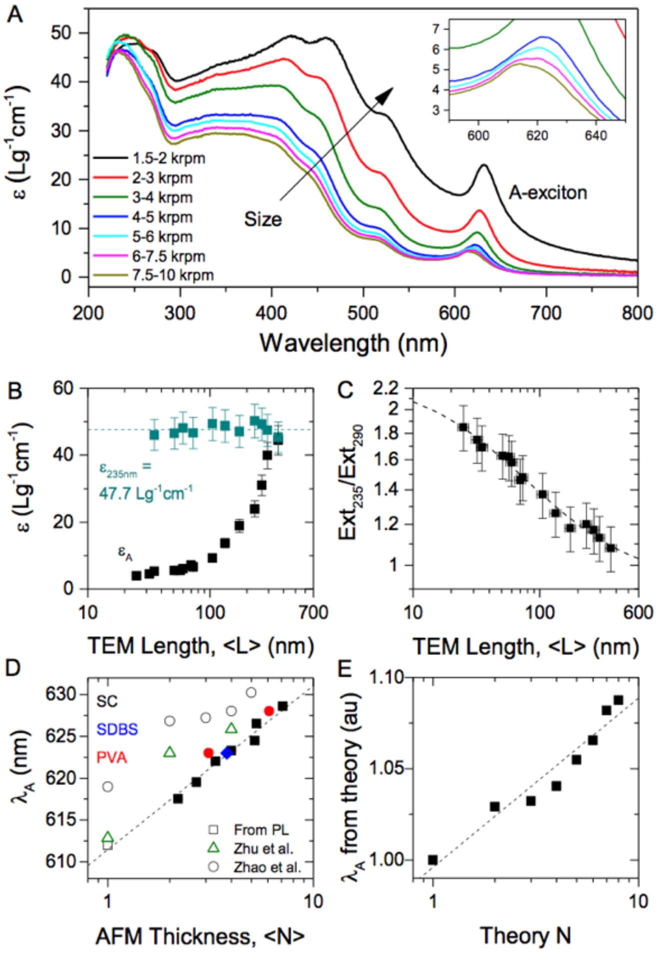

Figure 3.9: Dependence of the optical properties of nanosheet dispersions on the nanosheet dimensions. **A)** Optical extinction coefficient spectra measured for WS_2 dispersions (water/SC) prepared using different centrifugation conditions, and so with different mean nanosheet lengths and thicknesses. Inset: magnified A-exciton region. **B)** The extinction coefficient, measured at 235 nm and the A-exciton position (∼615nm) plotted versus mean nanosheet length, as measured by TEM. **C)** The ratio of extinction at 235 nm to that at 290 nm plotted versus mean nanosheet length, as measured by TEM. The dashed line is a fit to eq. 2. **D)** A-exciton center of mass position (determined from second derivatives) plotted versus mean nano- sheet thickness. Also included is data for WS_2 nanosheets dispersed in SDBS and PVA and from the literature. The open symbol represents the A-exciton position from photoluminescence measurements. The dashed line shows an empirical relationship between λ_A and N according to eq 4. **E)** Calculated relative wavelength associated with the optical gap of WS_2 [21] (i.e., the direct band gap at the K-point)

This equation was found to fit the data very well allowing us to generate a function, which relates the mean nanosheet length, <L> to the extinction peak intensity ratio (Equation 3.3):

$$L(nm) = \frac{2.3 - Ext_{235}/Ext_{290}}{0.02Ext_{235}/Ext_{290} - 0.0185} \tag{3.3}$$

This relationship is beneficial as it allows to extract the mean nanosheet length in any dispersion from an extinction spectrum without the need for time-consuming microscopic measurements.

3.4.2.1 Optical Extinction Dependence on Nanosheets Thickness

The extinction spectra not only contain encoded information on nanosheet length, <L>, but also on mean nanosheet layer number <N>. These changes in nanosheet thickness are visible as shifts in the A-exciton position, Figure 3.9A. The A-exciton shifts toward lower wavelengths as the nanosheet thickness is reduced. Moreover, not only the shift occurs but previously unseen spectral features become apparent. For example, for fractions isolated at high centrifugal forces (e.g. for the 7.5-10 krpm sample), the peak is composed of two distinguishable components: a shoulder at ∼622 nm and a peak at ∼612 nm (Figure 3.9A: inset). With increasing ML volume fraction, a well separated component at 2.033 [100] eV (∼612 nm) can clearly be identified and is attributed to ML-WS_2, while the previously existing one at about 622 nm corresponds to FL-WS_2.

To look closer into the A-exciton shift, the spectrum was first differentiated and then smoothed with the Adjacent Averaging Method. Then the centre of mass peak position at the full width of the half maximum (FWHM) in the smoothed second derivative was determined (as shown in Figure 3.10).

The relationship between the centre of mass position of the A-exciton (λ_A) and the mean WS_2 nanosheet thickness is presented in Figure 3.9D. As shown, λ_A increases logarithmically with nanosheet thickness and leads to an empirical metric for the number of layers of exfoliated WS_2. Importantly, data points using different stabilisers fall on the same curve. In addition, a comparison to literature [54] shows that such beviour is also observed in micromechanically exfoliated WS_2, even though it was far not explicitely discussed.

The data presented in Figure 3.9D can be fitted to the empirical Equation 3.4 which allows us to extract the mean nanosheet thickness <T> from the wavelength associated with the A-exciton (Equation 3.4):

$$< N >= 6.35 * 10^{-32} e^{\lambda_A(nm)/8.51} \tag{3.4}$$

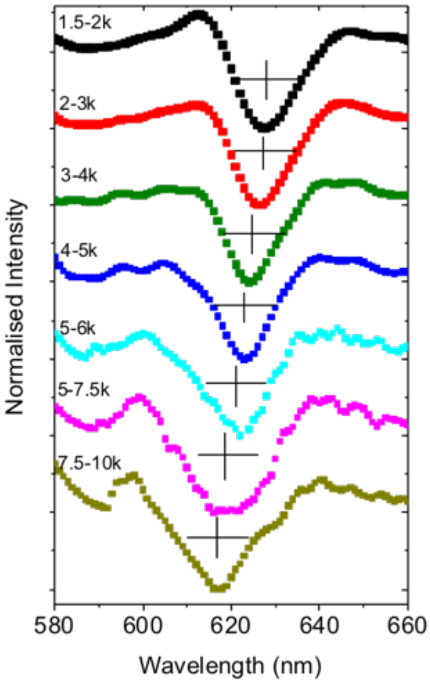

Figure 3.10: Smoothed second derivatives of the A exciton of the standard size selected samples

3.4.3 Photoluminescence Dependence on Monolayer Content in Dispersions

While quantitative spectroscopic metrics for length and thickness presented in subsection 3.4.2 are instructive, a metric for ML content would be even more useful and desired. The most obvious candidate characteristic of WS_2 to base it on, is the nanosheet photoluminescence (PL).

To determine the PL from the investigated dispersions, a Raman spectrometer was used. Due to its superior sensitivity, it was possible to detect PL even in uncentrifuged stock dispersions with low monolayer (ML) content. It was found that when acquiring a Raman spectrum from the surface of liquid drops of WS_2 ($\lambda_{\text{exc}} = 532$ nm), the photoluminescence of the monolayer is typically detected at high wavenumbers ($\sim$2460 cm^{-1}). This measurement is greatly facilitated by the high concentrations of WS_2 accessible from redispersing the sediments in LCC, as acquisition times can be minimised.

The Raman/PL spectra were acquired for all seven dispersions and normalised to the WS_2 Raman mode (355 cm^{-1}, 543 nm) and then plotted (Figure 3.11A) as a function of wavelength. In addition to the WS_2 Raman modes, (see inset on Raman shift scale), the typical photoluminescence peak of the WS_2 is detected at $\sim$612 nm. The last one was present only when dispersion contained monolayers. The feature at $\sim$650 nm is the Raman response of water due to the aqueous nature of these dispersion. It is clear that the photoluminescence increases relative to the Raman mode with decreasing nanosheet thickness and hence increasing monolayer content.

Further, a part of the WS_2 spectrum corresponding to a typical PL spectrum was plotted versus photon energy in Figure 3.11B. All PL spectra fit well to single Lorentzians, representing excitonic emission with minor contribution from trions which would introduce more asymmetry.

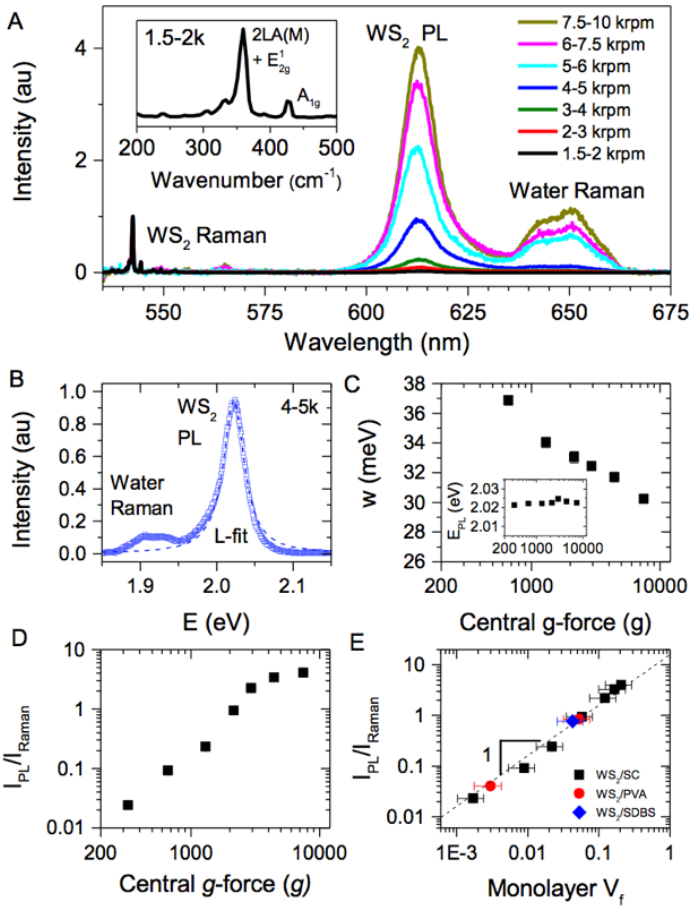

Figure 3.11: Photoluminescence data for dispersions with different monolayer content. **A)** Photoluminescence (~610 nm) and Raman (~540 nm) spectra of surfactant-stabilised WS$_2$ dispersions prepared with various centrifugation conditions and measured in liquid using a Raman spectrometer (λ_{exc}=532nm). **B)** Photoluminescence spectrum of WS$_2$, plotted on an energy scale and fitted to a Lorentzian. **C)** PL linewidth, from the Lorentzian fit, plotted versus central centrifugation acceleration (expressed in units of g). Inset: PL position vs g-force. **D)** The ratio of PL intensity to Raman intensity, I_{PL}/I_{Raman}, plotted vs g-force. **E)** I_{PL}/I_{Raman} plotted versus monolayer volume fraction

Lorentzian function is used for curves fitting in this work as this is the most commonly encountered band shape in infrared spectrometry. Also a number of publications on photoluminescence have demonstrated that high-quality materials displays a high-energy peak due to bound excitonic (BE) recombination. In elemental or binary III-V or II-VI materials the linewidth of the bound exciton is smaller than kT, since the bound exciton has no kinetic energy. The theoretical line shape of the bound exciton can therefore be approximated by a Lorentzian function. I have additionally tested Gaussian fitting on the same datasets but the fitting results clearly show that the Lorentzian lineshape is a better model for the data than the Gaussian. The last one gives worse fits than the Lorentzian what might be due to a presence of the trion emission at the lower energy from the main exciton component. Optimized Lorentzians provide accurate information about integrated intensity and position of each band what is usefull for establishing of the experimental metric.

Figure 3.11C shows the line width which falls off with increasing centrifugation rate. This suggests that larger nanosheets are slightly more defective than smaller ones. It must be noted that the acquired PL peaks are very narrow, displaying widths as low as 30 meV. This agrees well with micromechanically exfoliated WS_2 which usually displays PL linewidths of between 22 and 75 meV[37], [108]. This suggests that not only does the water/SC environment not significantly dope the nanosheets but also they are mostly defect-free after LPE.

As presented in Figure 3.11D we found the ratio of PL to Raman intensity to increase strongly with central g-force as the monolayer population increases. This intensity ratio, I_{PL}/I_{Raman}, can be quantitatively linked to the monolayer content which was determined from the statistical AFM analysis. It is suggested that the intensity of the Raman modes is proportional to the total number of WS_2 units probed by the laser. Because only the monolayers are luminescent, the PL intensity should be proportional to only the WS_2 units in monolayers. According to this, I_{PL}/I_{Raman} should scale linearly with the monolayer volume fraction. Figure 3.11E shows I_{PL}/I_{Raman} versus the monolayer volume fraction (V_f), and confirms that this is indeed the case. Importantly, this linear relationship holds over $>$ 2 decades of both I_{PL}/I_{Raman} and V_f and allows a rapid determination of the monolayer content.

Equivalent measurements for WS_2 nanosheets exfoliated in SDBS and PVA give data which fall on the same curve proving that this metric is quite robust toward changes in the stabiliser, although it may depend on the quality of the WS_2 starting material. A linear fit to the data presented in Figure 3.11E yields Equation 3.5 which related the PL/Raman intensity quantitatively to the monolayer content. While it holds over a broad range of sizes and monolayer content, we note that it eventually breaks down for very small nanosheets, as edges may activate non-radiative decay.

$$V_f = \frac{1}{17}\frac{I_{PL}}{I_{Raman}} \tag{3.5}$$

The presented photoluminescence – monolayer content dependence is a significant result, as it means that the monolayer volume fraction in a dispersion of WS_2 can be simply quantified by a Raman/PL measurement. This is hugely advantageous over traditional techniques such as AFM or TEM, which are very time consuming and can require skills and experience.

3.4.3.1 Optical Extinction Dependence on Nanosheets Dimensions in NMP System

This equation (Equation 3.4) applies to aqueous SC-, SDBS- and PVA-stabilized WS_2 dispersions [1], what was confirmed experimentally and almost certainly gives approximate nanosheet thicknesses in a wide range of liquid environments. It holds for surfactant-exfoliated WS_2 nanosheets, but was also tested for nanosheets exfoliated in the N-methyl-pyrrolidone (NMP) solvent. For this purpose, WS_2 was exfoliated and size-selected in NMP and extinction spectra acquired. After this, the samples were centrifuged again and redispersed in aqueous SC to quantify <L> and <N> *via* the established metrics.

The result of the metric <L> and <N> for WS_2 exfoliated in NMP is plotted as a function of median *g*-force in Figure 3.12A,B. With the exception of the smallest nanosheets, the data from LCC in NMP collapses on the same curve as SC in the case of <L>, Figure 3.12A. The deviation at high centrifugal forces is likely related to

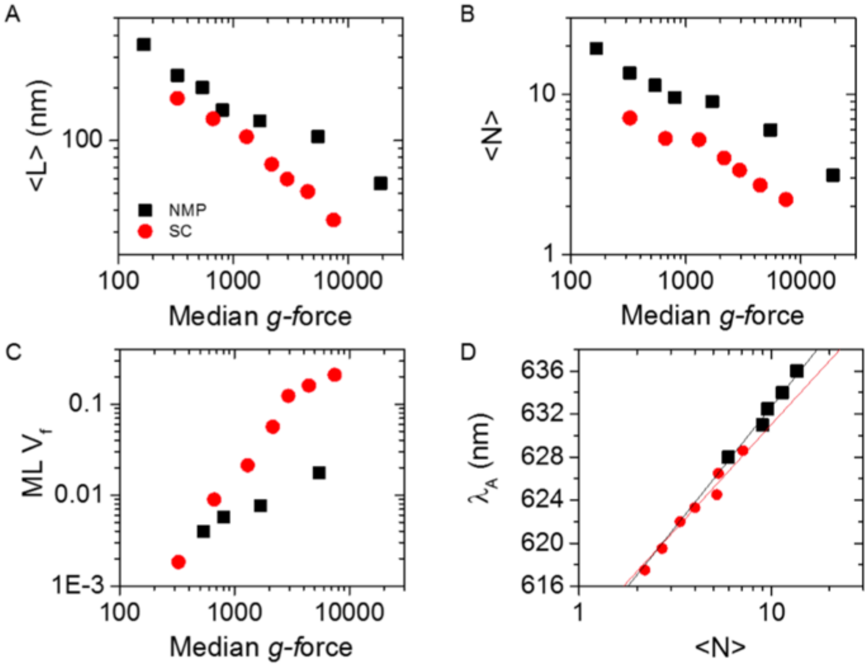

Figure 3.12: Comparison of LCC in NMP to LCC in SC. **A)** nanosheet length **B)** Nanosheet thickness **C)** Monolayer volume fraction **D)** Wavelength associated with A-excition, plotted vs mean nanosheet thickness for nanosheets exfoliated in NMP and SC

the fact that the population of nanosheet sizes and thicknesses is different in the stock dispersion after exfoliation in NMP and SC. In contrast, the thickness data for the samples exfoliated in NMP is offset to thicker nanosheets with a similar trend (Figure 3.12B). This strongly suggests that nanosheets exfoliated in NMP are simply thicker in general, but the separation mechanism is the same.

Following the WS_2 – exfoliated in aqueous SC solution the metric described in section 0, the A-exciton wavelength (in SC and NMP, respectively) vs mean nanosheet thickness for nanosheets exfoliated in both SC and NMP were plotted together (Figure 3.12D). The red line represents the metric for SC-exfoliated WS_2 and fits quite well with a black line for NMP- exfoliated WS_2 nanosheets. While the NMP data gives a slightly different slope, the quantitative relationship is still similar in NMP. This suggests that the SC thickness metric equation (Equation 3.4) could be applied to NMP dispersions and it is accurate within $< 20\%$ error, especially if <N> is below 10. This small mismatch implies that solvatochromic effects occur, i.e. that the exciton binding energy is influenced by the dielectric environment.

Although Equation 3.4 can be used as a first approximation in any system based on aqueous or organic solvents we used the data presented Figure 3.12D to extract an accurate thickness metric for WS_2 nanosheets in NMP (black line). From now the thickness of nanosheets in NMP can be estimated and is given by the newly adjusted Equation 3.6

$$< N >= 6.35 * 10^{-28} e^{\lambda_A (nm)/9.74} \tag{3.6}$$

3.4.3.2 Ageing of WS_2 SC Dispersions and Oxidation Prevention

There are obvious advantages to the LPE method of WS_2 including the high quality of samples obtained and the ability to control nanosheet lateral dimensions. In addition, the observed photoluminescence of the monolayers gives a unique and sensitive handle to investigate the stability over time.

To address this, a series of Photoluminescence measurements were taken with two different sizes of nanosheet dispersions after various time intervals. The Photoluminescence excitation-emission maps were acquired with a PL spectrometer to give access to a broader excitation/emission profile compared to the measurement in Raman spectrometers. The excitation was varied between 350 nm and 500 nm. The emission was detected in the range 490-800 nm. To avoid scattering, a red cut-off filter was placed on the emission side. The measurements were taken on fresh dispersion, 1-day old dispersion, 2 days, 3 days old dispersion and finally at a week old one. Results of such an experiment are presented in Figure 3.13.

It is clear there are changes in PL with dispersion age. It is suggested that this is the result of the oxidation of the monolayer nanosheets in the aqueous environment. Changes are more pronounced for small nanosheets than for larger ones suggesting that degradation starts from the edge. Even though this process is undesired, it

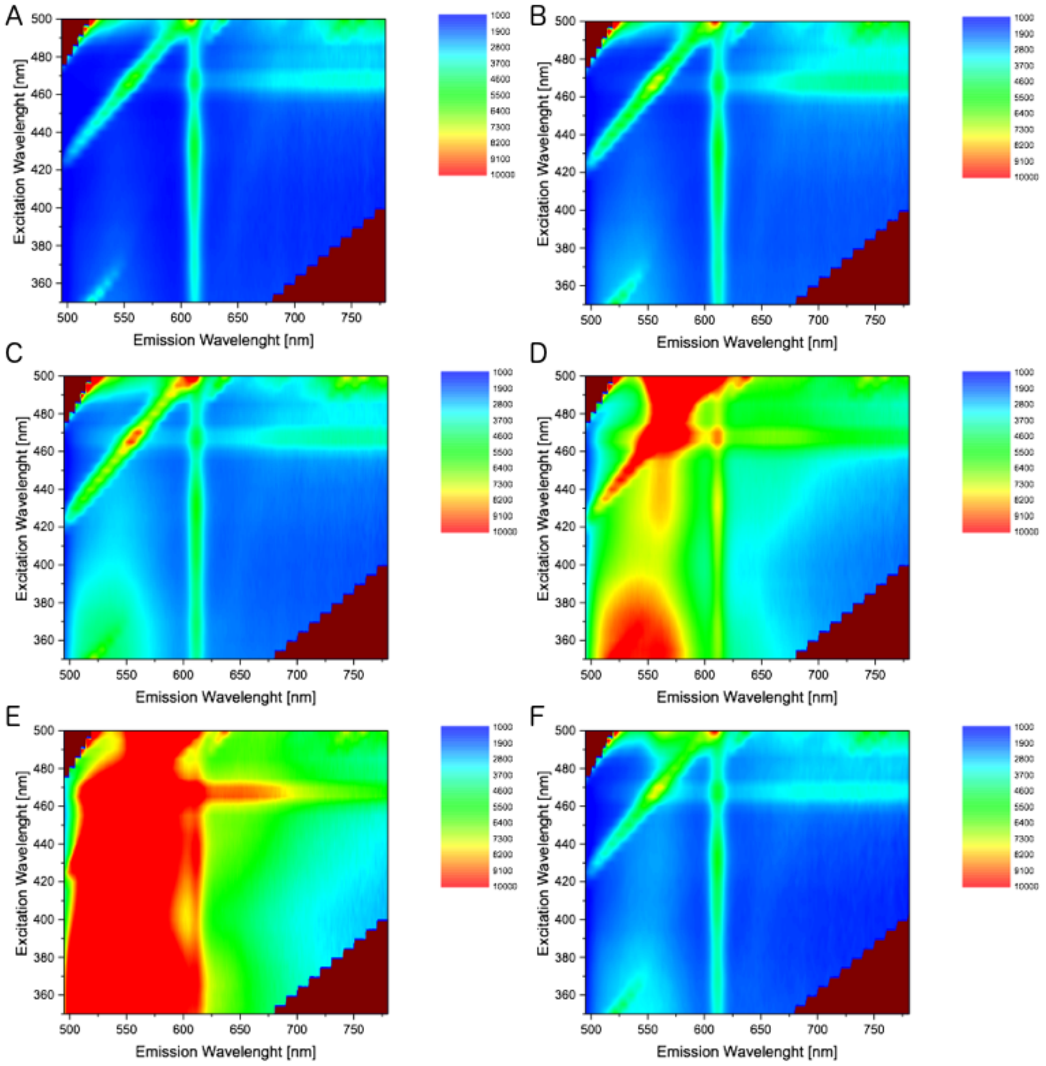

Figure 3.13: Excitation-Emission Photoluminescence contour plots of WS_2 H_2O-SC based dispersions (5-22k g) measured at different times after the exfoliation stored at room temperature. **A)** Fresh dispersion. **B)** 1 day old. **C)** 2 days old. **D)** 3 days old. **E)** 7 days old. **F)** 7 days old stored in low temperature.

emphasises the strength of LPE, size selection and characterisation of monolayer ensembles, as this information would have otherwise not been accessible.

Furthermore, it opens the possibility to prevent the degradation. A possible solution would be storage of the samples at lower temperatures to decrease the probability of the activation energy to overcome. While the initial dispersions were taken for the time dependent measurements, half of each dispersion was kept in the fridge at a temperature of 4 °C. The halves maintained in the refrigerator for the seven days were subjected to the same measurement as the samples stored at the room temperature. They did not exhibit any of the ageing effects as previously shown. The excitation emission maps were virtually unchanged compared to the acquired from the freshly prepared dispersion, Figure 3.14.

The storage at lower temperatures is an easy, non-invasive and efficient way to maintain the optical properties of WS_2 dispersions and prevent ageing due to oxidation. Nontheless, care must be taken in further processing steps to avoid elevated temperatures as much as possible. The finding that the degradation can be readily followed from photoluminescence also represents the foundation for future investigations in this area.

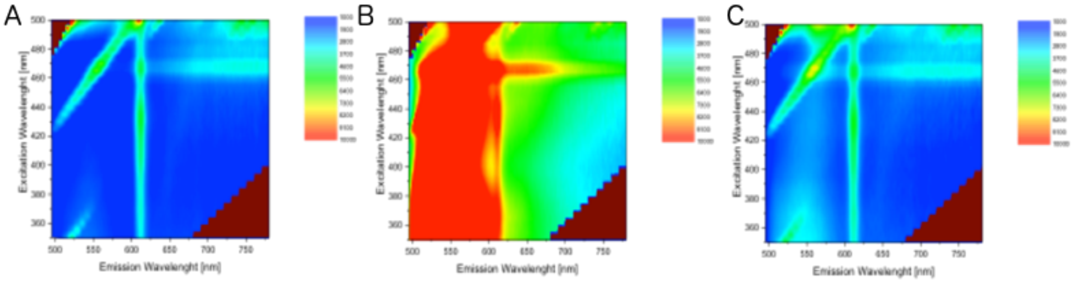

Figure 3.14: Excitation-Emission Photoluminescence contour plots of WS_2 H_2O-SC based dispersions (5-22k g). **A)** Fresh dispersion. **B)** 1-week old dispersion kept at room temperature. **C)** 1-week old dispersion maintained in the fridge.

Chapter 4

Nonlinear Optical Characterization

4.1 Introduction

Investigation of light propagation in materials being concerned as Nonlinear Optical (NLO) media is crucial for the development of photonic devices like photonic crystals, saturable absorbers, optical switches, optical limiters, etc[11], [14], [15], [77], [122]. Till now, a variety of materials, such as porphyrins [30], fullerenes[31], [32], [64], carbon nanotubes[84], [109], [110] and graphene[65], [78], have been found to exhibit effects like strong nonlinear extinction (NLE), nonlinear absorption (NLA) and nonlinear scattering (NLS), to high-intensity laser field. Those have a chance to be considered to be used as photonic materials in real devices [66].

Since the graphene discovery which highlighted not only a new material with extraordinary physical and chemical properties but revolutionised the traditional concept of nanoscience and nanotechnology a new chapter of two-dimensional (2D) materials[7], [125] has been opened. Having in mind the need for the development of novel photonic devices, the nonlinear and ultrafast optical properties of the 2D nanomaterials like nonlinear refraction and absorption, carrier relaxation lifetime were undoubtedly important to be investigated.

The family of transition metal dichalcogenides (TMDC s) has received significant attention[38], [70] because of their unique properties like large surface area, the weak coupling between the layers and high mechanical strength [79].

Being so different from the zero-gap graphene, TMDs nanomaterials represents a broad range of electronic properties from insulating to metallic. WS_2 which is of our most vital interest, is for instance a semiconductor with a high potential for use in electronic devices [96]; transistors [39], photoswitches [67], supercapacitors [80], additives for mechanical reinforcement [105] or gas sensors [118].

It is known by now that the physical properties of atomically thin TMDCs are dependent not only on the type of metal and chalcogenide elements [88] but also on the nanosheet sheet size and thickness [97]. Also, the band structure strongly depends on the number of layers changing its electrical properties as they become thinner from the bulk to the monolayer. It is important to note that the intensity dependence of different nonlinear processes might vary a lot and one can observe the process at a lower intensity which will be overtaken by another process at a higher intensity.

In this work, the NLO properties of variable thickness WS_2 nanosheets were investigated with use of a Z-scan technique in both the nanosecond and femtosecond time scale regimes.

The use of both nanosecond and femtosecond laser pulse durations allows accessing different nonlinear processes which naturally occurs on various timescales [6]. For femtosecond pulses, almost all electronic relaxation processes are slower than the pulse duration. In effect, the main observable processes in femtosecond time scale are transient electronic excitations. When we look at the nonlinear processes in nanosecond scale, usually the relaxation times are much faster than the pulse duration. The energy carried by single nanosecond laser pulse is also much larger than that carried by femtosecond pulse. As a result, thermal accumulation processes like scattering or plasma bubbles become dominant at high energies, especially in nanosecond regime.

4.2 Nanosecond Z-scan

The nonlinear optical properties of WS_2 dispersions were investigated by the open aperture Z-scan technique with 6 ns Gaussian pulses at 532 nm from Q-switched Nd: YAG laser with repetition rate of 10 Hz. Dispersions were held in 1 mm path length cuvettes. The linear transmission of the samples was set at 80% for all time. Since measurements were carried out in the nanosecond regime, thermal effects must be considered as a contributing factor.

The Z-scan home built geometry (Figure 4.1) consisted of mentioned Minilite II laser source, detector, reference detector as well as focusing lenses, a beam splitter and a translation stage.

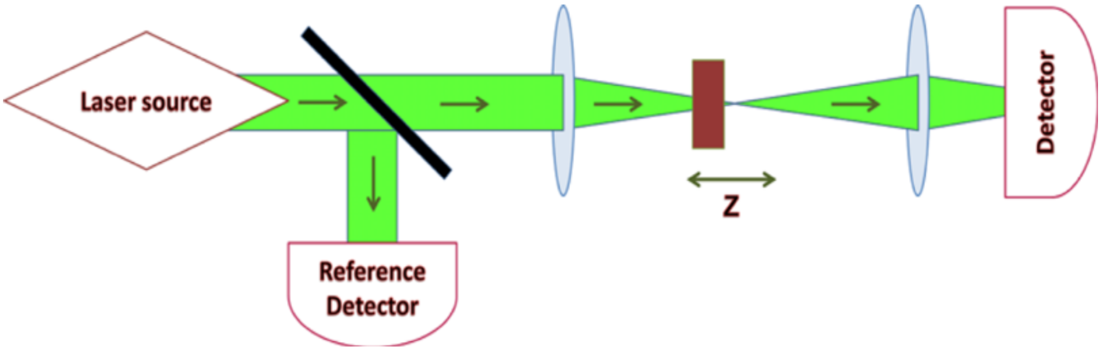

Figure 4.1: Schematic of the geometry of the Z-scan setup

The Z -scan technique was applied to study the NLO properties of mono- bi- and few- layer nanosheets of eight WS_2 dispersions with different thickness prepared by the standard method described in detail in section 3.2 and previously extensively characterised (section 3.3).

The mentioned before Q-switched Nd: YAG laser with repetition rate of 10 Hz was used to generate 6 ns pulses with incident light energies being equal to 0.1 mJ, 0.75 mJ, 1.5 mJ, 3.0 mJ. Specially written LabView software was used to operate the measurement allowing to control the step, dwell time, averaged number of pulses as well as the total z-distance. The detector collected the light transmitted through the sample at the end of its route. The signal was then normalised to the flat part of the curve. Then, the normalised transmittance was used to evaluate the NLO properties of the different size of WS_2 nanosheets.

What one can observe is that in some cases normalised transmittance's maximum take positive value (upward facing curve) and WS_2 exhibits Saturable Absorption (SA). In other situations, when normalised transmittance's maximum takes a negative value (downward facing curve), the sample is dominated by Nonlinear Scattering and exhibits Optical Limiting.

Since the curves obtained from Z -scan measurements of WS_2 perform both SA and OL phenomena a two-process equation [55] was used to fit the Z-scan curves (Equation 4.1):

$$\alpha = \frac{\alpha_0}{1 + \frac{I}{I_s}} + \beta_{eff} I \tag{4.1}$$

where:

α_0 – the linear absorption coefficient

I – incident laser intensity

I_s – saturable intensity

β_{eff} – nonlinear coefficient

The expression – "$\alpha_0 /(1+ I / I_s)$" represents the Saturable Absorption part, which increases when I_s rises. The second part indicates that with a higher value of β_{eff}, the contribution of Nonlinear Scattering increases, resulting in Optical Limiting. The Z-scan plots of all WS_2 dispersions were fitted using Equation 10, and the fitted plots are displayed in Figure 4.2.

Figure 4.2A-D show fitted experimental Z-scan results, where the normalised

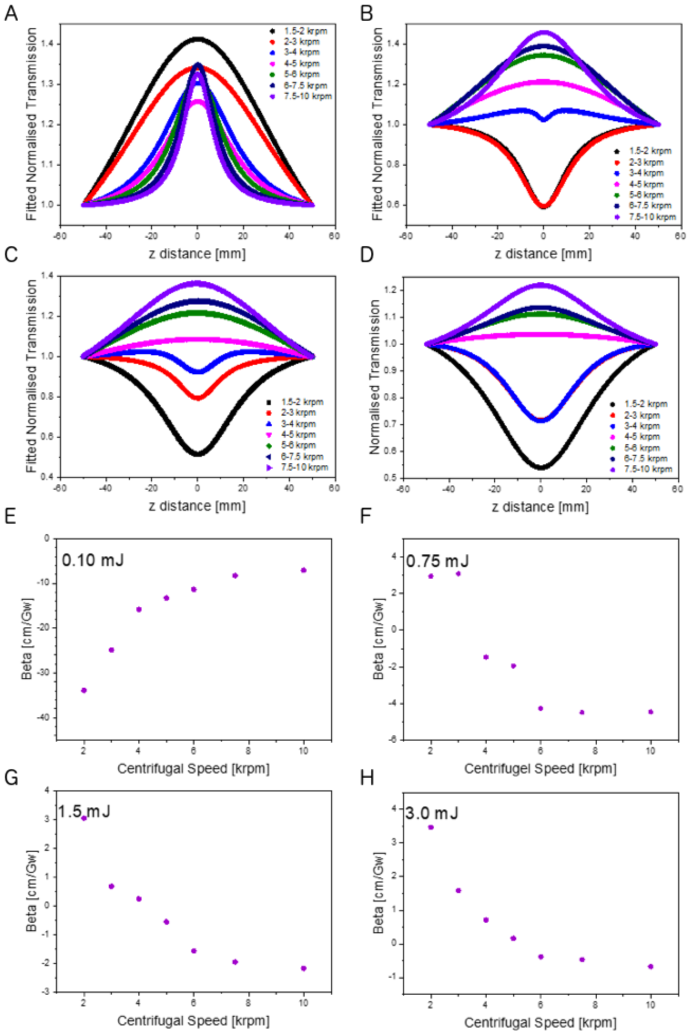

Figure 4.2: **A-D)** Size and energy dependent Nonlinear Optical Response of WS_2 nanosheets (fitted). **(A)** 0.1 mJ. **(B)** 0.75 mJ. **(C)** 1.50 mJ. **(D)** 3.00 mJ. **E-H)** Size dependent β_{eff} coefficient **(E)** 0.1 mJ. **(F)** 0.75 mJ. **(G)** 1.50 mJ. **(H)** 3.00 mJ.

transmission was plotted vs sample position Z. Each of the plots shows size dependent WS_2 dispersion NLO response for corresponding incident energy of 0.1 mJ, 0.75 mJ, 1.50 mJ, 3.00 mJ respectively.

Presented (Figure 4.2) open-aperture, fitted Z-scan curves are symmetric, with the centre about Z_0. That proves that the focused Gaussian beam field is symmetric and much smaller than the Rayleigh length of the lens and therfore thickness of nonlinear medium can be neglected[56], [98].

Figure 4.2 shows that all WS_2 dispersions exhibit NLO behaviours in the nanosecond regime. For some of the WS_2 dispersions at any given incident energy, the transmittance increases near the laser beam focus (z distance = 0) indicating obvious SA. In some other cases, WS_2 exhibited a decreased transmittance near the zero Z–position implying Optical Limiting process.

Looking into details, Figure 4.2A-D represents the NLO response of WS_2 nanosheets of a variable number of layers at different incident energy respectively. Data presented on Figure 4.2A corresponds to the lowest investigated intensity of 0.10 mJ. Nevertheless of the WS_2 nanosheets thickness, the NLO response is purely Saturable Absorption process, and it is getting stronger as the nanosheets are bigger.

The calculated from fitting β_{eff} values were plotted vs the centrifugal speed (Figure 4.2E). As the WS_2 nanosheets are getting smaller and thinner (larger centrifugal speeds) the values of β_{eff} are presenting rising trend, but still negative values. They are presented in Table 4.1.

No.	Energy N	0.1 mJ cm/GW	0.75 mJ cm/GW	1.5 mJ cm/GW	3.0 mJ cm/GW
1	7.1	-33.88	2.95	3.05	3.47
2	5.3	-24.87	3.09	0.68	1.59
3	5.2	-15.80	-1.47	0.25	0.71
4	4.0	-13.23	-1.95	-0.55	0.17
5	3.4	-11.31	-4.26	-1.56	-0.39
6	2.8	-8.26	-4.48	-1.95	-0.47
7	2.2	-7.07	-4.45	-2.13	-0.68

Table 4.1: Size dependent β_{eff} coefficient for a variable pulse energy of nanosecond pulses.

Depending on the thickness and incident laser energy, more than one nonlinear process is occururing at the same time. That means that the signal observed in the measurement comprises of two or more phenomena. A good example of the transition between the nonlinear processes occurring during the WS_2 interaction with the laser light are fitted Z-scan curves for 1.5-2 krpm sample presented on Figure 4.2. When incident energy of 0.01 mJ was applied to the 3-4 krpm nanosheets Saturable Absorption was observed, (Figure 4.2A). As the energy increases the effects of Nonlinear Scattering (so Optical Limiting) became more prominent. With energy of 3.00 mJ (Figure 4.2D), the optical limiting was a dominant process and only this one could be observed. Apart from that, depending on thickness of the nanosheets in the dispersion, for the same value of energy, there are curves that exhibit either SA or OL features. This is because both processes occur at the same time with one of them being dominant depending on single nanosheet thicknes.

The β_{eff} values plotted vs centrifugal speed at 0.01 mJ in Figure 4.2E) become less negative as the nanosheets become smaller. In case of 0.75 mJ, 1.50 mJ and 3.00 mJ, β_{eff} values are increasing with a decrease of nanoflakes size, (Figure 4.2F,G,H). That is the opposite finding to the first one. The reason for such behaviour is the higher incident energy injected into the systems by the laser source (0.75 mJ, 1.5 mJ and 3.0 mJ). It is found that in general for higher incident intensity the SA process reverts into the OL process as the high-energy introduced in the system tend to produce scattering centres. Also, the larger particles have smaller I_s what makes them scatter easily while smaller nanosheets tend to saturate.

4.3 Femtosecond Z-scan

The nonlinear optical properties of different WS_2 dispersions prepared by the standard method described in detail in section 3.2 and previously extensively characterised section 3.3) were again investigated by the open aperture Z-scan technique (same geometry as for nanosecond measurements, Figure 4.1).

This time the femtosecond regime WS_2-laser light interactions have been studied. A fibre laser generating 340 fs Gaussian pulses at 520 nm with a repetition rate of 100 Hz was used as a source. Dispersions were held in 1 mm path length cuvette, and their linear transmission was fixed at 80%. The size-dependent NLO processes were observed in WS_2 dispersions when the variable energy of 0.75 μJ, 3.0 μJ, 8.0 μJ were injected into the system.

The experimental data were fitted similarly to data from nanosecond measurements (details in section 4.2) according to the Equation 4.1. Figure 4.3AC show fitted experimental Z-scan results, where the normalised transmission was plotted vs sample position Z. Each of the plots shows size dependent WS_2 dispersion NLO response for corresponding incident energy of 0.75 μJ, 3.0 μJ, 8.0 μJ respectively. The Figure 4.3D represents β_{eff} nonlinear coefficient for all investigated dispersions plotted vs centrifugal speed. It is easy to notice that the incident energy has a clear impact on the observed trends. The β_{eff} coefficient for all data points is presented in Table 4.2.

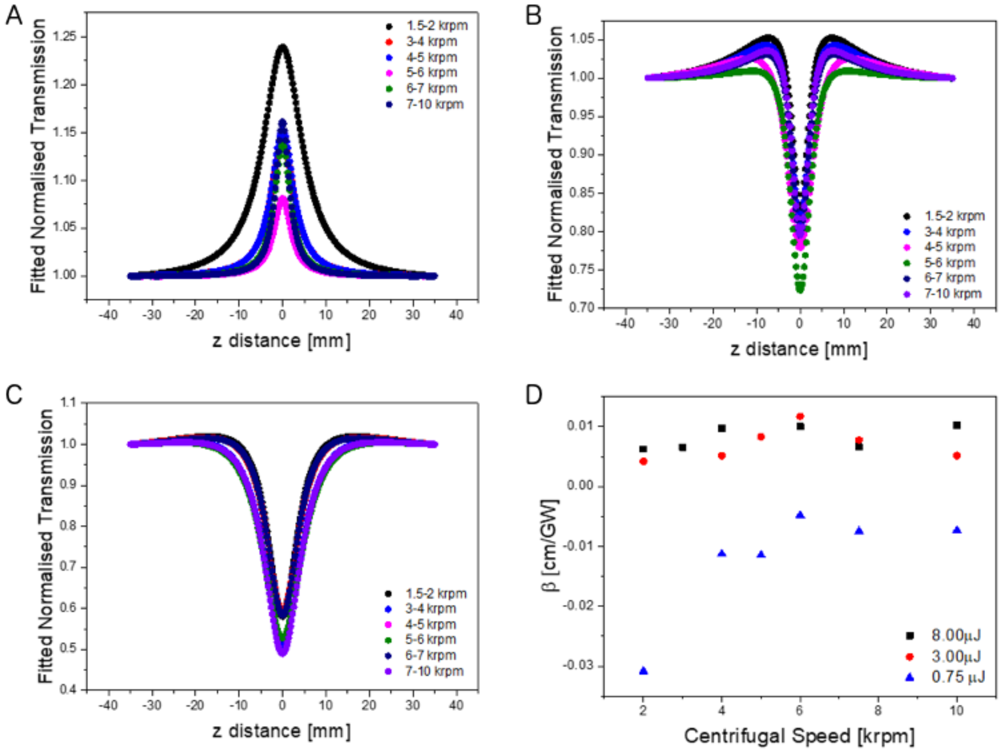

Figure 4.3: **17 A-C)** Size and energy dependent Nonlinear Optical Response of WS_2 nanosheets (fitted). **(A)** 0.75 μJ. **(B)** 1.50 μJ. **(C)** 3.00 μJ. **D)** Size dependent β_{eff} coefficient for variable WS_2 nanosheets size and pulse energy of femtosecond pulses

Plots presented in Figure 4.3 shows that all WS_2 dispersions exhibit NLO behaviour in the femtosecond regime. For WS_2 dispersions at low incident energy (0.75 μJ) the transmittance rapidly increased near the laser beam focus point (z distance = 0) indicating obvious saturable absorption. As the incident light fluence increases (3.00 μJ), optical limiting become prominent. The peak envelope of Z-scan curve becomes larger and might be attributed to the thermally induced nonlinear scattering. Strong optical limiting is dominating at high excitation fluence (8.0 μJ). This phenomena have also been reported in other transition metal dichalcogenide (TMDC) nanosheet dispersions.

No. N	Energy	8.0 μJ cm/GW	3.0 μJ cm/GW	0.75 μJ cm/GW
1	7.1	0.0062	0.00422	-0.03086
2	5.3	0.00655		
3	5.2	0.00968	0.00513	-0.01125
4	4.0		0.00835	-0.01147
5	3.4	0.01007	0.01173	-0.00480
6	2.8	0.00664	0.00778	-0.00748
7	2.2	0.01023	0.00516	-0.00731

Table 4.2: Size dependent β_{eff} coefficient for a variable pulse energy of femtosecond pulses

Nonlinear Optical Response of WS_2 dispersions exfoliated with Liquid Phase Exfoliation method was studied in details in this chapter. WS_2 dispersions with varying dimensions were studied using two types of laser sources. Femtosecond pulses with energies of 0.75 μJ, 3.0 μJ and 8.0 μJ, and nanosecond pulses with energy of 0.1 mJ, 0.75 mJ, 1.50 mJ, 3.00 mJ were used. The open aperture z-scan directly confirmed NLO properies. The resuls showed that WS_2 exhibits stronger nonlinear optical response and saturable absorption in the fs pulse excitation than in the ns excitation regime. Depending on the value of applied energy saturable absorption or optical limiting were observed. By manipulating thickness, the same material can be used as a saturable absorber or as a nonlinear limiter that may protect optical sensors against damage from pulsed lasers.

Chapter 5

WS_2 - Monolayer Enrichment of Liquid Dispersions

5.1 Introduction

As introduced in previous parts of this thesis Liquid Phase Exfoliation method [92] is a versatile technique producing liquid suspensions of 2D nanosheets. This process is an inexpensive and well established method, but tends to give nanosheets with broad lateral size distribution (length, thickness), Figure 3.6. This broad distribution also means that the monolayer content is quite low, below 10%, what is a serious problem for a number of applications like printed electronics. In the long term, the application will require monodisperse suspensions of only N-layers, where N will be defined by the application.

While some progress has been made towards the size selection of nanosheets, these processes are still very inefficient and yield minimal quantities of nanosheets. Monolayer (ML) enrichment is an even more challenging process than size selection itself. What is needed, is a scalable and universally applicable high yield technique to size select nanosheets or to produce highly monolayer dispersions.

Inspired by gas-separation, we have developed Secondary Liquid Centrifugation Cascades (SLCC) which allow dispersions to be both size selected and monolayer enriched at the same time in a controlled way, i.e. while maintaining reasonable lateral sizes [21]. As a result, we were able to develop secondary cascades to enhance monolayer content reaching values of ∼70%. Moreover, such monolayer-rich dispersions exhibit photoluminescence and optical properties that are distinctive from other WS_2 ensembles and that reflect the high monolayer content.

5.2 Experimental Procedure

We have designed a number of centrifugation protocols, so called secondary cascades. These begin with pre-size selected dispersions with an aim at enriching the dispersions in as few centrifugation steps as possible while maintaining in as few centrifugation steps as possible at the same time maintaining reasonable nanosheets sizes.

5.2.1 Homogeneous Cascading

The homogeneous centrifugation was compared with LCC trapping size selection at various centrifugation rates. This comparison is presented in Figure 5.1. Data is plotted vs g-force, which in the case of homogeneous centrifugation (red data points) represents the actual centrifugation speed, while in the event of the trapping between rpm cascade, the central speed is plotted. The data for the LCC was extracted from microscopy statistics, while metrics were used in the case of the homogeneous centrifugation.

At first, we designed and tested a very simple primary centrifugation cascade (subsection 3.2.2), which resulted in the production of a range of size-selected fractions (Figure 5.1), the last of which was monolayer-enriched up to N_{mono} / NT ∼ 40% and

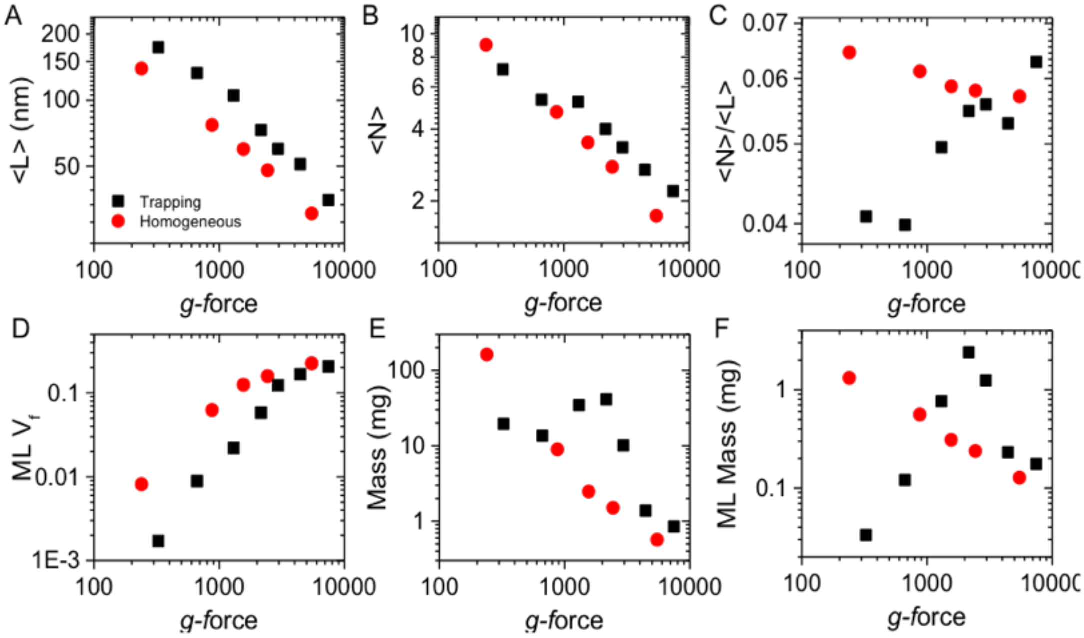

Figure 5.1: Comparison of LCC trapping size-selection and homogenous centrifugation at different rates. **A)** Mean nanosheet length versus g- force showing a decrease in nanosheet size with increasing centrifugation speed. **B)** Mean nanosheet thickness versus g-force showing a decrease in nanosheet thickness with increasing centrifugation speed. In general, mean sizes (length and thickness) are smaller for samples produced by homogeneous centrifugation, as the smallest nanosheets were not removed. **C)** Thickness/length aspect ratio as a function of centrifugation speed. The aspect ratio is widely constant for the homogeneous centrifugation, but increases in the case of the LCC size- selection. **D)** Volume fraction of monolayers versus g-force. In both cases, V_f increases monotonically, albeit less steeply for the homogeneous centrifugation suggesting ML enrichment is less efficient. **E)** Total mass of WS_2 and **F)** monolayer mass of WS_2 collected in each sample

$V_f \sim 20\%$. This cascade was the foundation for the work described above.

Changes in mean length <L>, mean number of monolayers per sheet <N>, <N>/<L> aspect ratio, ML V_f, total mass and ML mass were extracted and compared in Figure 5.1. Mean nanosheet length *versus g*- force shows a decrease in nanosheet size with increasing centrifugation speed, while mean nanosheet thickness showed a reduction in nanosheet thickness with increasing centrifugation speed.

In general, mean sizes (length and thickness) are smaller for samples produced by homogeneous centrifugation, as the smallest nanosheets are not removed in the process. This means distributions are inherently broader after homogeneous centrifugation which is undesirable. This is also manifested in the thickness/length aspect ratio which is widely constant for the homogeneous centrifugation, but increases in the case of the LCC size selection. The volume fraction of monolayers in both cases increases monotonically. This increase is more gradual for the homogeneous centrifugation, suggesting ML enrichment is less efficient. Finally, the total mass of WS_2 and monolayer mass of WS_2 collected overall is lower in the homogeneously centrifuged sample.

5.2.2 Repeated Centrifugation

Another approach to making highly monolayer rich dispersions was through repeated centrifugation at fixed rotations. In this procedure as a first step dispersion was centrifugated at a given speed (eg. 2.5 krpm) for a certain time (eg. 90 min). Then the sediment was collected as a first sample and the supernatant was taken for subsequent centrifugation (with exactly the same centrifugation parameters). Again the sediment was collected as a second sample and the supernatant was taken for further iteration of the procedure.

The repeated centrifugation at two fixed speeds (2.5 krpm and 4 krpm) was compared with LCC trapping size selection. The comparison is presented in Figure 5.2. The data is plotted vs iteration step for both variants of centrifugation procedures. Changes in mean length <L>, mean number of monolayers per sheet <N>, <N>/<L> aspect ratio, ML V_f, total mass and ML mass were extracted and compared in Figure 5.2. Mean nanosheet length and thickness are plotted as a function of iteration step. Repeated centrifugation at a fixed centrifugation speed was found to be significantly less efficient to achieve size-selection. The thickness/length aspect ratio slightly increases for the repeated centrifugation at 2.5 krpm, while it decreases in the case of 4 krpm. This shows that nanosheets of a given length are be-

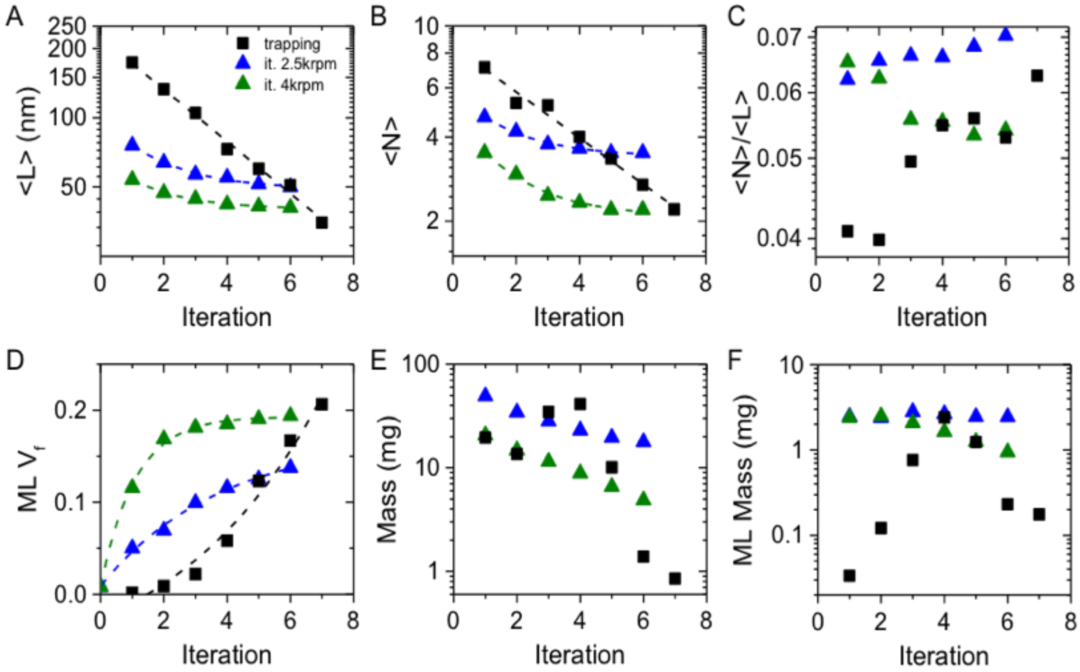

Figure 5.2: Comparision of the size selection cascade to repeated centrifugation at two fixed speeds. **A)** Mean nanosheet length and **B)** nanosheet thickness plotted as function of iteration step. Repeated centrifugation at a fixed centrifugation speed (2.5 and 4 krpm, respectively) is significantly less efficient to achieve size-selection. **C)** Thickness/length aspect ratio plotted versus cycle number. Interestingly, the aspect ratio slightly increases for the repeated centrifugation at 2.5 krpm, while it decreases in the case of 4 krpm. This is important, as it shows that nanosheets of a given length are becoming thinner. **D)** Monolayer volume fraction is a function of cycle number. The repeated centrifugation at fixed rpm is powerful in enriching the samples in monolayers (while widely maintaining the mean nanosheet size). However, an exponential increase is observed suggesting that saturation is reached at some stage (which is dependent on the centrifugation speed chosen). **E)** Total mass of WS_2 and **F)** mass of ML WS_2 as function of cycle number

coming thinner. The total mass of WS_2 and mass of ML WS_2 falls off comparatively slowly for the repeated centrifugation at a fixed rotational speed. Most importantly, no MLs are lost in the case of the repeated centrifugation at 2.5 krpm. The repeated centrifugation at fixed rpm is highly powerful at enriching the samples with monolayers while widely maintaining the mean nanosheet size. However, an exponential increase is observed which means saturation is reached at some stage with ML V_f depending on the centrifugation speed.

5.2.3 Complex Secondary Cascades

Presuming that longer centrifugation runs give a similar result as the iterative centrifugation, we can use the iterative centrifugation experiments to begin designing secondary cascades with the aim to break the initial <N>-<L> relationship and increase monolayer contents. The data above (Figure 5.2) suggests that centrifugation at low speeds such as 2.5 krpm should enrich the dispersion with ML without loss of too much ML mass. Additionally, extended centrifugation runs at about 4 krpm are expected to change the aspect ratio N/L (beneficially) of nanosheets and simultaneously increase the number of ML. Based on this preliminary knowledge, we combined long (overnight) centrifugations at low speeds with short high-speed centrifugations. This brought about the design of much more complex cascades , resulting in higher degrees of monolayer enrichment. Their strength will be not only versatility, but also the possibility to apply them to nanosheets exfoliated in solvents.

Each further approach of more complex and efficient post-processing of WS_2 dispersions starts with an initial size selection well described in subsection 3.2.2 and then, follow general scheme of secondary cascading which is presented in Figure 5.3.

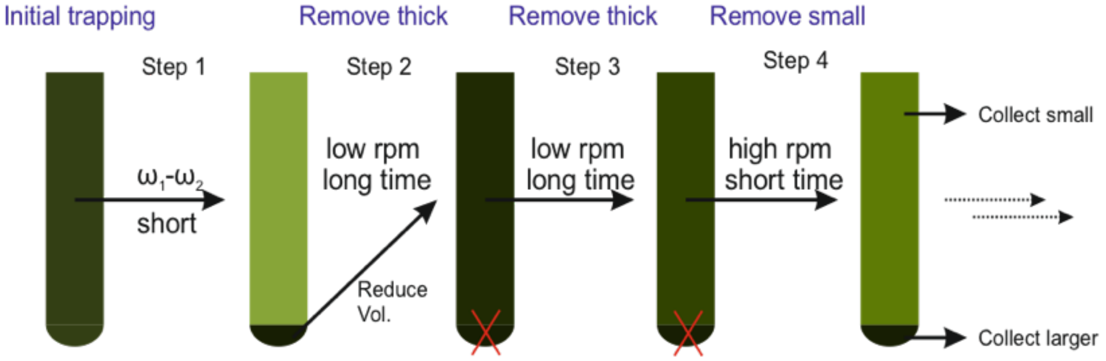

Figure 5.3: Schematic representation of the ML enrichment centrifugation

As displayed above, after the initial size selection, samples are centrifuged in further iterations at lower rpms for longer times to remove thick nanosheets and in fast short iterations to remove very small nanosheets. When designing such a cascade (if highly luminescent dispersions are required), the small-nanosheet-removal step is crucial as the PL/Raman ratios are significantly lower for very small nanosheets (even at high ML contents), probably due to edge effects. A few specific examples of the secondary enrichment cascades will be described in detail in further sections of this chapter.

5.2.3.1 ML Enrichment Secondary Cascade #1 (strongly size selected)

As shown in the scheme of the developed secondary cascade #1 on Figure 5.4A, the stock dispersion produced via liquid phase exfoliation was initially trapped between 6-8 krpm, then centrifuged at 4 krpm rotational speed for 6 hrs. After this step, the overall volume was reduced and the dispersion was further centrifuged at a rotational speed of 5 krpm for 14 hrs. Here, the sediment was discarded, and the supernatant was taken for 4 hr centrifugation at 9 krpm rotational speed. The overall volume was once again reduced and finally centrifuged for 1 hr at the high rotating speed of 15 krpm removing small nanosheets.

At each step of the cascading procedure, dispersions were subjected to UV-Vis, Raman/PL and a subset of samples to AFM characterisation and statistical analysis.

Raman /PL spectroscopy on five samples corresponding to each step of the cascade were recorded with an excitation wavelength of 532 nm. They were measured in liquid as described in the methods section. Normalised Raman/PL spectra are shown in Figure 5.4B indicating the increase in relative PL intensity which corresponds to a higher content of ML in the dispersion.

UV-Vis spectra of the dispersions at each step of the secondary cascade were normalised at 290 nm. Observable changes in the region 200-250 nm are related to variations in the length of the nanosheets. The inset of Figure 5.4C show changes in the A-exciton position, which are related to changes in nanosheet thickness. These were observed in detail as the 2$^{\text{nd}}$ derivatives of the A-exciton region were calculated

(Figure 5.4D), presenting contributions of ML and FL WS_2.

A subset of the samples of the enrichment procedure as indicated in Figure 5.4A was subjected to AFM imaging. These were WS_2 dispersions obtained by; standard size selection 6-8 krpm used as a starting point for ML enrichment, the sediment after step 3, the supernatant after step 4 and the sediment after step 5.

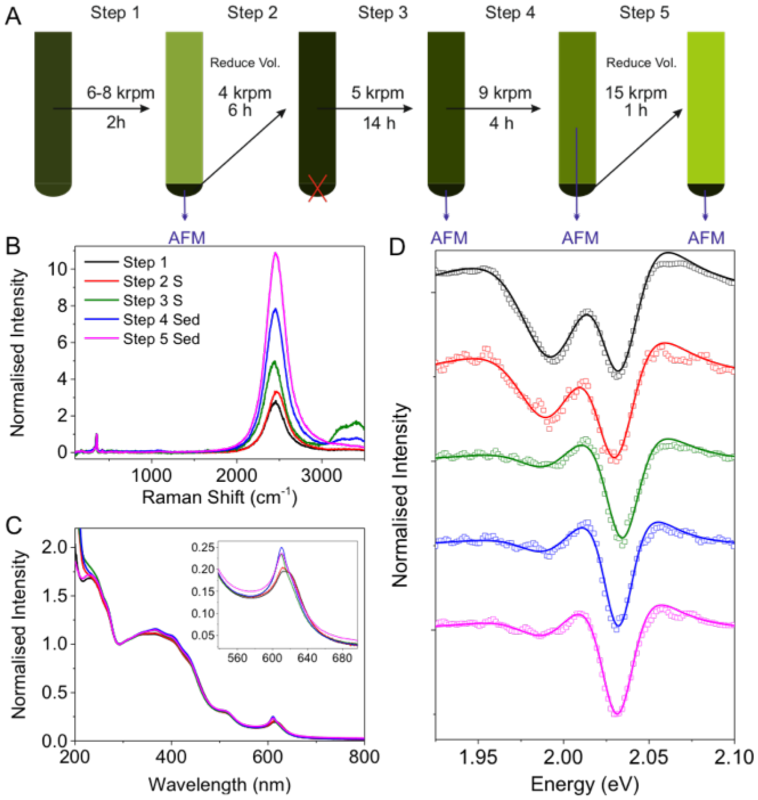

Figure 5.4: Spectroscopic data of example 1 of the monolayer enrichment. **A)** Schematic of the centrifugation procedure. A subset of the samples as indicated was subjected to AFM statistical analysis. **B)** Normalized Raman/PL spectra (λexc= 532 nm) measured on liquid drops of the dispersions after the centrifugation steps as indicated showing the increase in relative PL intensity related to the ML enrichment. **C)** UV-Vis extinction spectra normalized to 290 nm. Changes in the spectra region 200-250 nm are related to changes in length. Inset: A-exciton. Changes in the shape of the A-exciton are related to varying distributions of ML and FL WS_2. **D)** Second derivatives of the A-exciton obtained after smoothing the spectrum with the Lowess method (10-15 points). The spectra were fitted to the second derivative of two Lorentzians

The results are shown in Figure 5.5 including representative images for each sample, statistically calculated layer number histograms and histograms of the (corrected) length of the nanosheets. Note that both the supernatant after step 4 and sediment after step 5 show very narrow thickness distributions governed by monolayers.

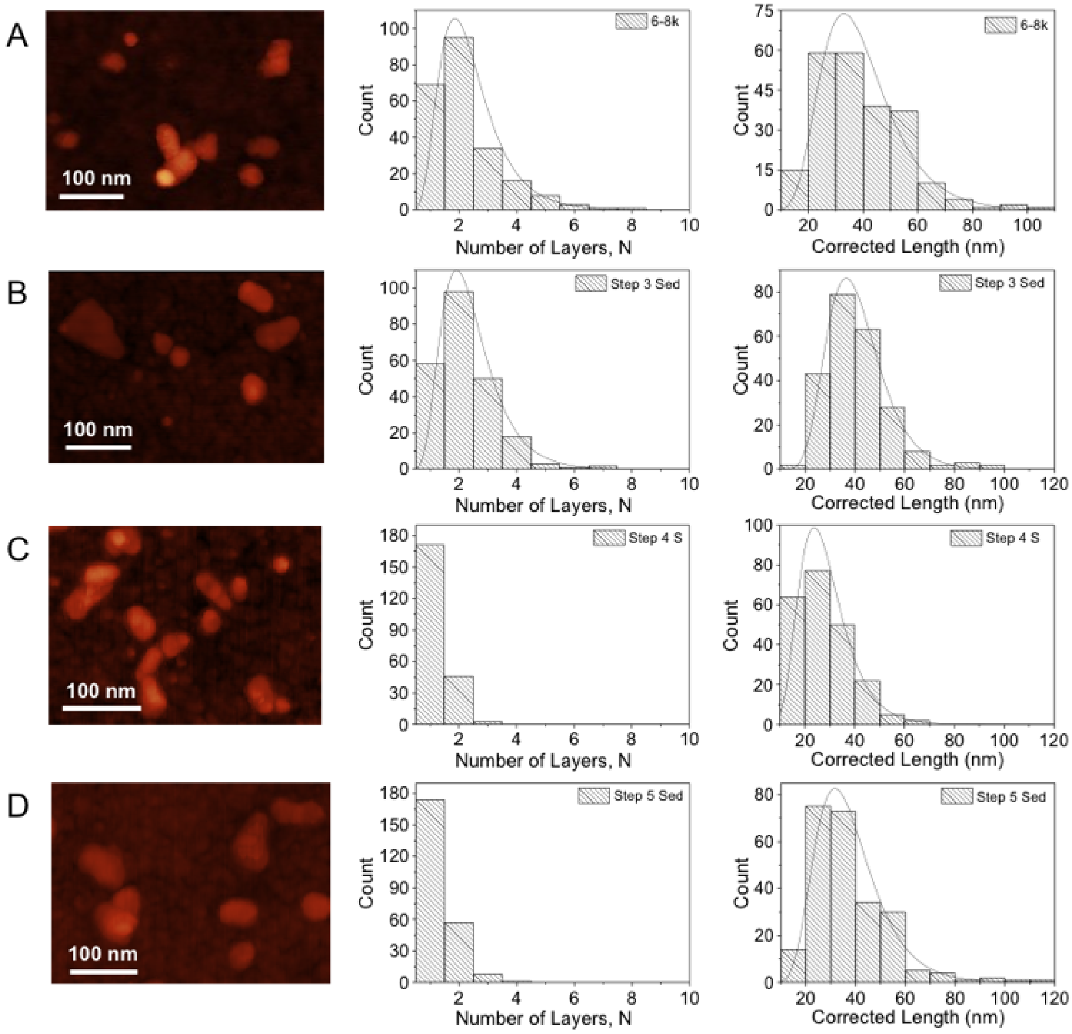

Figure 5.5: AFM analysis of selected samples of the monolayer enrichment procedure

Based on the analysis of the spectroscopic characterisation and AFM imaging, the monolayer volume fractions, as well as mean length and mass of WS_2, were calculated. As expected, the ML volume fraction increased with each step as confirmed by both Raman/PL (Figure 5.4B) and statistically analysed AFM (Figure 5.5A-D).

The data obtained from the different information sources are conclusive with the exception for the supernatant after step 4, where AFM shows a significantly higher monolayer content than anticipated by PL/Raman based. This is due to the large population of small nanosheets in this dispersion, where edges dominate the optical properties and quench the PL. Also, information regarding the mean length of nanosheets and WS_2 mass was extracted at each step and is presented in Figure 5.6. As a result of that secondary cascade, the ML V_f increased from 18 % in the starting dispersion to 65% (PL/Raman in accordance with AFM) with <L> of ~ 40 nm and a yield of ~ 10% of the initial dispersion.

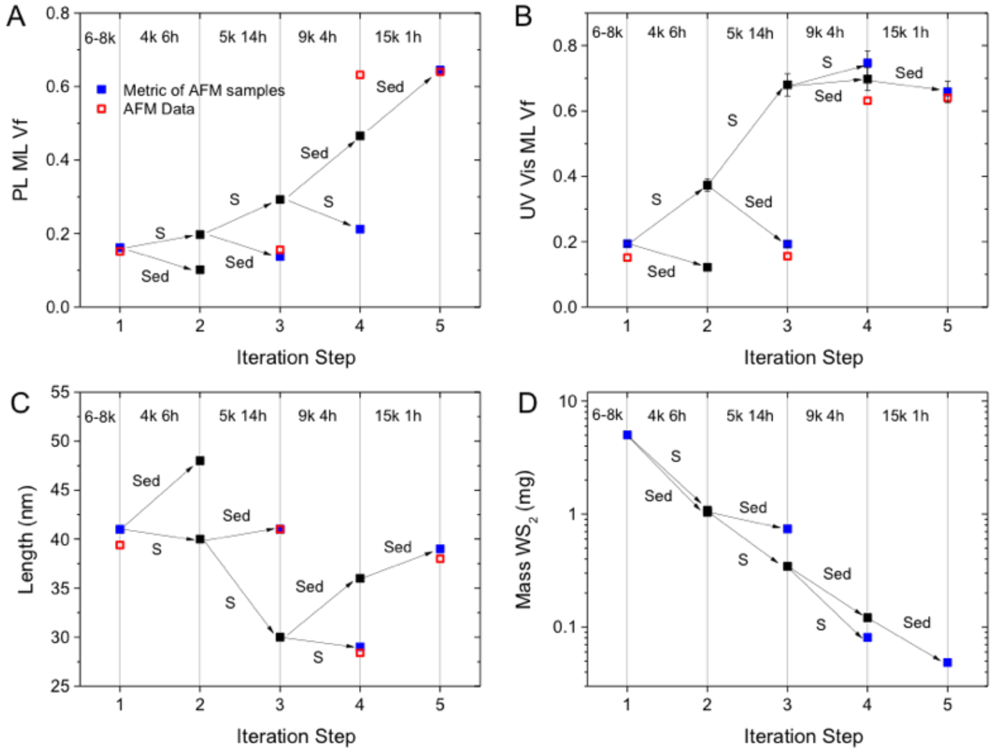

Figure 5.6: Summary of example 1 of the ML enrichment centrifugation cascade procedure. **A)** Volume fraction of monolayers determined from the PL/Raman metric of the supernatants (S) or sediments (Sed) after each iteration step. **B)** Volume fraction of monolayers determined from the UV-Vis A-exciton shape metric. Again, a strong discrepancy is observed when very small nanosheets are enriched. **C)** Mean length determined from the empirical UV-Vis peak intensity ratio Ext235 nm/Ext290 nm of the supernatants (S) or sediments (Sed) after each iteration step according to equation 3. The (corrected) length from AFM agrees very well with the metric data. **D)** Mass of WS_2 after each iteration step

5.2.3.2 ML Enrichment Secondary Cascade #2 (weakly size selected)

In an attempt to increase the mass of the monolayer-rich dispersion, a second example of a ML enrichment secondary cascade was designed. In this case, the stock dispersion produced via liquid phase exfoliation was initially trapped between 1.5-10 krpm, giving a broad size distribution of nanosheets in the starting dispersion in all lateral dimensions. As in the first step of SLCC, it was centrifuged at 2.5 krpm rotational speed for 16 hrs. After this step, the sediment consisting of large and thick nanosheets was discarded and the supernatant centrifuged at 4 krpm for 14 hrs discarding still thick nanosheets from the dispersion in the sediment. The supernatant was centrifuged again in a short 1 hr high speed centrifugation at 10 krpm to remove very small nanosheets in the supernatant. Overall volume was reduced, and the dispersion was further centrifuged at a rotational speed of 5 krpm for 5 hrs. Here, the sediment was discarded and the supernatant was taken for 2 hr centrifugation at 8 krpm rotational speed. After this step, the supernatant was discarded and the sediment finally centrifuged for 12 hrs at the low rotating speed of 3 krpm. The sediment was discarded again and the supernatant collected as a final ML rich dispersion of the cascade.

At each step of the cascading procedure, dispersions were subjected to UV-Vis and PL/Raman. AFM characterisation and statistical analysis were performed on the final dispersion.

PL/Raman spectroscopy on seven samples corresponding to each step of the cascade were taken with an excitation wavelength of 532 nm. They were measured in liquid as described in the methods section (chapter 2). Normalized PL/Raman spectra are shown in Figure 5.7B and illustrate the increase in relative PL intensity which corresponds to the higher content of ML in the dispersion.

UV-Vis spectra of the dispersions at each step of the secondary cascade were normalised to 290 nm. Observable changes in the region 200 - 250 nm are related to

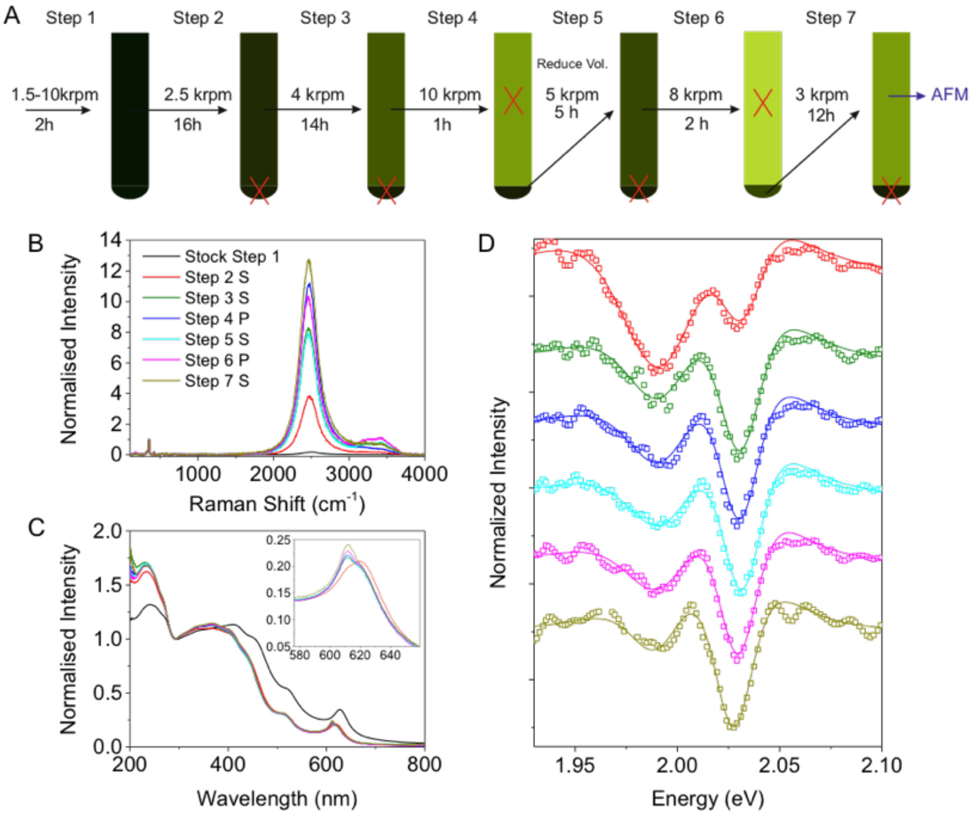

Figure 5.7: Spectroscopic data of example 2 of the monolayer enrichment. **A)** Schematic of the centrifugation procedure. The final supernatant was subjected to AFM. **B)** Normalized Raman/PL spectra (λ= 532 nm) measured on liquid drops of the dispersions after the centrifugation steps as indicated in A) showing the increase in relative PL intensity related to the ML enrichment. **C)** UV-Vis extinction spectra normalized to 290 nm. Changes in the spectra region 200-250 nm are related to changes in length. Inset: A-exciton. Changes in the shape of the A-exciton are related to varying distributions of ML and FL WS_2. **D)** Second derivatives of the A-exciton obtained after smoothing the spectrum with the Lowess method (10-15 points). The spectra were fitted to the second derivative of two Lorentzians

variations in the length of the nanosheets. The inset of Figure 5.7C shows changes in the A-exciton position which are related to changes in thickness. Those were observed in details through the 2nd derivative of the A-exciton region were calculated (Figure 5.7D), presenting contributions of ML and FL WS_2.

The final dispersion of the enrichment procedure as indicated in Figure 5.7A was subjected to AFM imaging. A representative image as well as the statistically calculated number of layers and length histograms are presented in Figure 5.8.

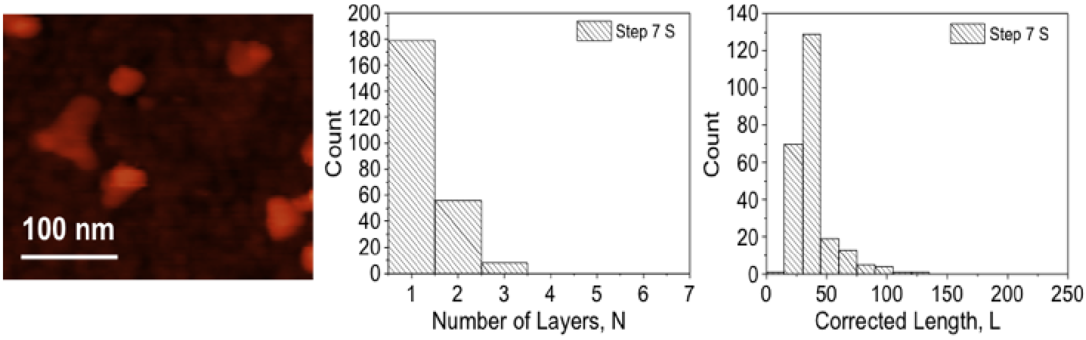

Figure 5.8: AFM analysis of selected samples of the monolayer enrichment procedure 2

Based on the analysis of the spectroscopic characterisation and AFM imaging, the monolayer volume fraction, as well as the mean length and mass of WS_2 were calculated (Figure 5.9A-D). As expected the ML volume fraction increased with each iteration as confirmed by PL/Raman and AFM on the final sample. Also, information regarding the mean length of nanosheets and WS_2 mass was extracted at each step of the SC and is presented in Figure 5.9. As a result of this secondary cascade, the ML volume fraction increased from 6% in the starting dispersion to 74% (PL/Raman in agreement with AFM) at the end of the cascade. <L> of 40 nm is similar to the SLCC #1. Notably, the mass of WS_2, while still being low (0.1 mg) has increased by a factor of ~5 compared to SLCC#1. This confirms that careful tuning of the cascade shows promise in producing reasonable quantities of high quality, ML rich dispersions.

5.2.4 Summary of ML Enrichment Results

Above we described Secondary Cascades (S.C.), which used strongly (original sample 6-8 krpm, a secondary sample labelled S.C.1) and weakly (1.5-10 krpm, S.C.2) size-selected dispersions as starting points for monolayer enrichment. Figure 5.10 is an informative summary of the findings of the described monolayer enrichment process

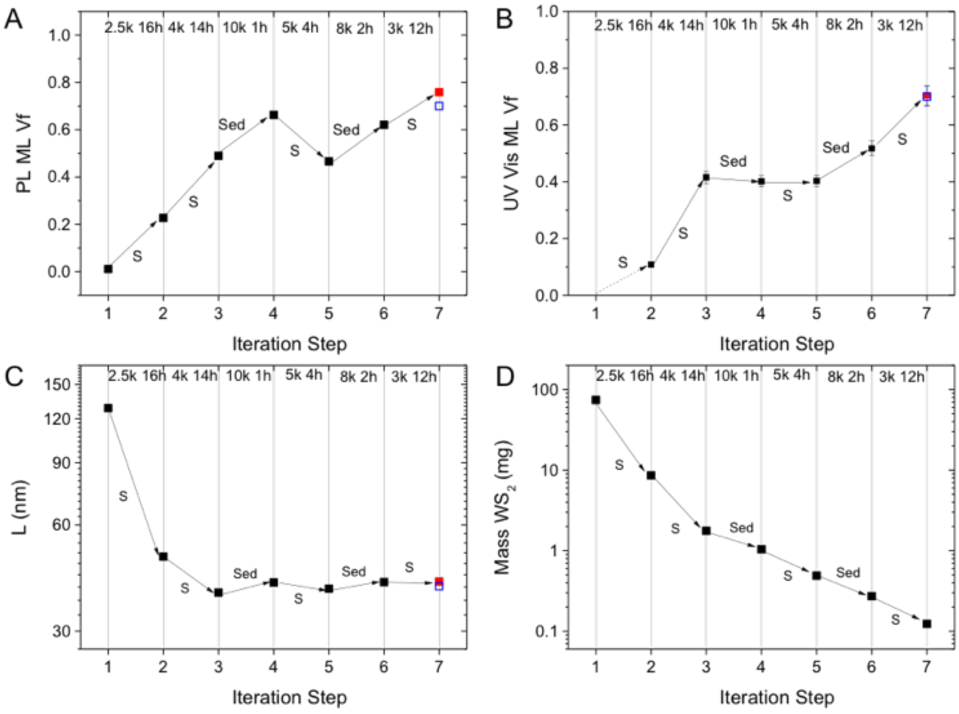

Figure 5.9: Summary of example 2 of the ML enrichment centrifugation procedure. **A)** Volume fraction of monolayers determined from the PL/Raman metric of the supernatants (S) or sediments (Sed) after each iteration step. **B)** Volume fraction of monolayers determined from the UV-Vis A-exciton shape metric. Again, a strong discrepancy is observed when very small nanosheets are enriched. **C)** Mean length determined from the empirical UV-Vis peak intensity ratio Ext235 nm/Ext290 nm of the supernatants (S) or sediments (Sed) after each iteration step according to equation 3. The (corrected) length from AFM agrees very well with the metric data. **D)** Mass of WS_2 after each iteration step

in both cases.

The AFM based number of layers histogram for the S.C.2 final dispersion with a typical image in the inset Figure 5.10A shows clearly that monolayers dominate this sample. AFM analysis states that $N_{mono}/N_{all} \sim 74\%$ and monolayer $V_f \sim 70\%$ (out of 4% and 1% in the starting dispersion). The PL/Raman spectra of the 6-8 krpm dispersion and both ML enriched dispersions are shown in Figure 5.10B. While the 6-8 krpm dispersion displayed $I_{PL}/I_{Raman} = 2.8$, equivalent to $V_f = 16\%$, it is clear that the enriched samples display considerably more intense PL. We found $I_{PL}/I_{Raman} = 10.9$ and 12.7, for the S.C.1 and S.C.2 dispersions, giving V_f of 65% and

75% respectively, in good agreement with the mentioned AFM statistics.

Figure 5.10C presents extinction spectra for the 6-8 krpm sample and the S.C.1 and S.C.2 dispersions. The shapes of these spectra are almost indistinguishable because high-speed centrifugation steps have been included in the cascade to remove very small nanosheets giving similar <L> values for these dispersions which was confirmed by AFM statistics. We note that in this nanosheet size range, scattering does not exist as the extinction spectrum is identical to the absorbance spectrum.

Even more interesting is the shape of the A- excitonic components of the extinction spectra as shown in the inset of Figure 3.9A and Figure 5.10C. Not only were there changes in the centre of mass peak position (Figure 5.10D), but also in shape. Unlike the spectra associated with thicker nanosheets, the 6-8 krpm spectrum has a peak at ~612 nm and a shoulder at ~622 nm as mentioned in 4.4.2 (Figure 3.9, ML-rich samples have A-excitonic responses dominated by a peak close to 610 nm (2.032 eV) which is extremely close to the position of the A-excitonic PL peak (2.023 eV, implying a Stokes shift of 10 meV). Due to the exponential scaling of the A-exciton energy with layer number [1], we associate the feature at ~610 nm (2.033 eV) in the extinction/absorbance spectrum of the ML-rich sample with the absorbance of monolayer WS_2 and the component at ~622 nm (1.99 eV) with the combined contribution of few-layered WS_2.

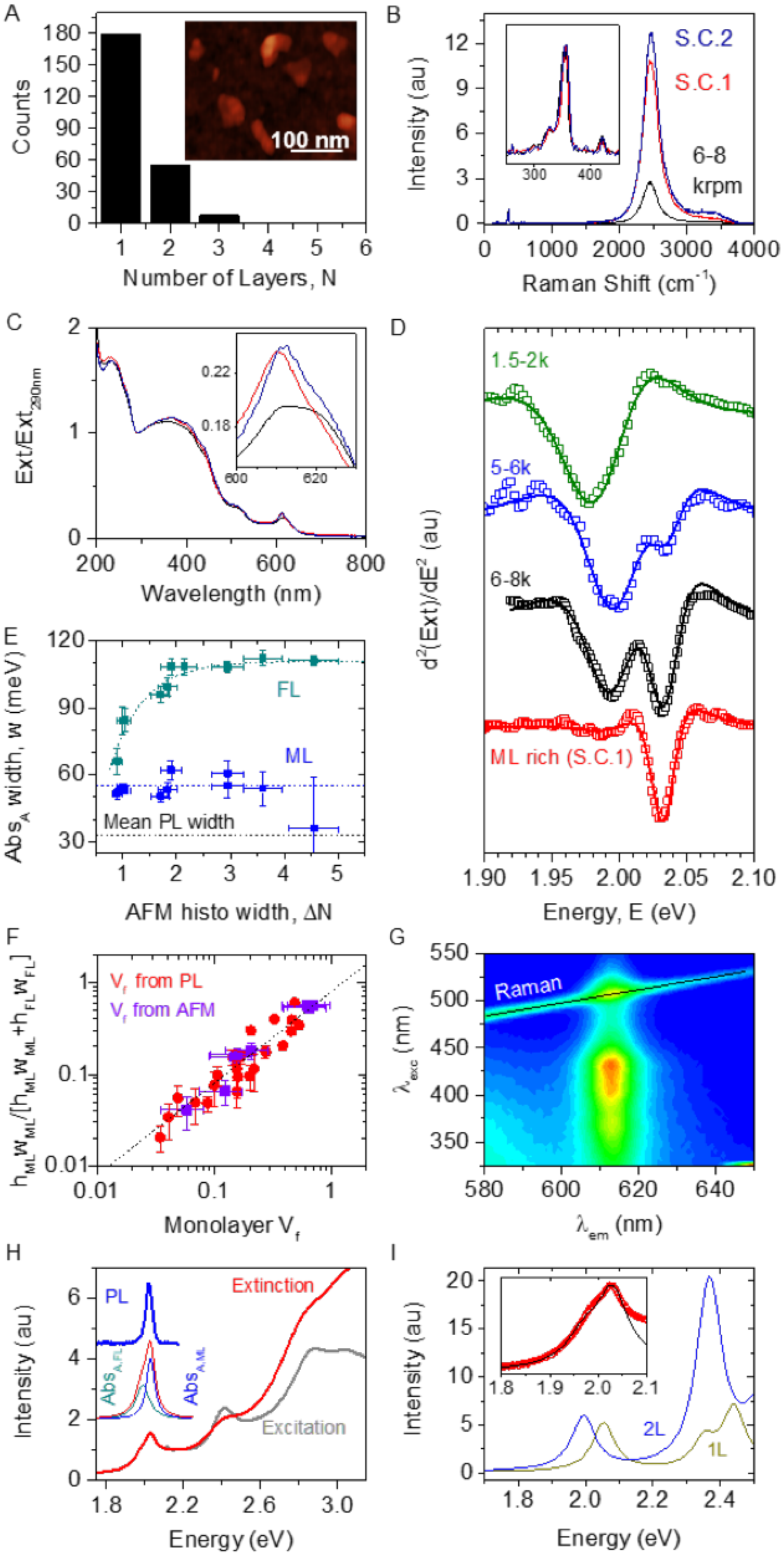
A
Counts
180
150
120
90
60
30
0
1 2 3 4 5 6
Number of Layers, N
100 nm
B
Intensity (au)
12
9
6
3
0
S.C.2
S.C.1
6-8
krpm
300
400
0 1000 2000 3000 4000
Raman Shift (cm^{-1})
C
Ext/Ext_{290nm}
2
1
0
0.22
0.18
600
620
200 400 600 800
Wavelength (nm)
D
$d^2(Ext)/dE^2$ (au)
1.5-2k
5-6k
6-8k
ML rich (S.C.1)
1.90 1.95 2.00 2.05 2.10
Energy, E (eV)
E
Abs_A width, w (meV)
120
90
60
30
FL
ML
Mean PL width
1 2 3 4 5
AFM histo width, ΔN
F
$h_{ML}w_{ML}/[h_{ML}w_{ML}+h_{FL}w_{FL}]$
1
0.1
0.01
V_f from PL
V_f from AFM
0.01 0.1 1
Monolayer V_f
G
550
500
450
400
350
λ_{exc} (nm)
Raman
580 600 620 640
λ_{em} (nm)
H
Intensity (au)
6
4
2
0
PL
Extinction
$Abs_{A,FL}$
$Abs_{A,ML}$
Excitation
1.8 2.2 2.6 3.0
Energy (eV)
I
Intensity (au)
20
15
10
5
0
1.8 1.9 2.0 2.1
2L
1L
1.8 2.0 2.2 2.4
Energy (eV)

Figure 5.10: Characterisation of the monolayer enriched dispersions (summary). **A)** AFM nanosheet thickness (expressed as layer number) histogram and representative image of WS_2 nanosheets from a dispersion enriched in monolayers by a secondary LCC. **B)** Raman/PL spectra of the ML-rich dispersion (red) compared to the first stage size-selected dispersion used for the ML enrichment centrifugation (blue). An alternative secondary cascade yielded a similar dispersion (yellow). **C)** Optical extinction spectra of the three dispersions. Inset: Zoom in of the A-exciton showing clear changes in spectral shape. **D)** Second derivative spectra for a number of WS_2-SC dispersions fitted to the sum of the second derivatives of two Lorentzians. **E)** Width of absorbance Lorentzian curves, representing mono- and few-layer nanosheets, found by fitting second derivatives **F)** A-exciton shape monolayer metric, obtained from fitting the second derivative of the extinction spectra to two Lorentzians, as a function of ML volume fraction. The violet squares represent data where V_f was measured from AFM, whereas V_f was determined from the PL/Raman ML metric in the case of the red data points. The dashed line shows a linear relation that can be used to determine the $\mathrm{V_f}$ from the shape of the A exciton. **G)** Excitation-emission contour plot of the ML-rich dispersion measured in a PL spectrometer. **H)** Extinction spectrum of the ML-rich dispersion compared to the excitation spectrum at the ML emission (after subtraction of the water background). The same excitonic features are evident in both spectra. Lower inset: A- exciton absorbance deconvoluted into the individual components of ML and few-layer WS_2 as well as their sum. Upper inset: Measured PL spectrum (450 nm excitation). **I)** Theoretical absorption curves for monolayer (1L) and bilayer (2L) WS_2. Inset: Extinction curve measured for S.C.2 monolayer enriched sample (open symbols). Also shown is the weighted sum (Abs = 0.71Abs1L + 0.24Abs2L, black line) of the theoretical monolayer and bilayer absorption spectrum. These weightings were chosen to reflect the volume fraction of monolayers and bilayers in the S.C.2 sample as measured by AFM

The observed relationship was further studied in detail. To do this, we carefully smoothed the extinction spectra of all samples with the Lowess method prior to differentiating the spectrum. In contrast to first differentiating and smoothing the second derivatives with Adjacent Averaging (see subsection 2.2.1), this alternative method narrowed the contributing peaks roughly 3-fold, allowing the resolution of closely spaced peaks. Examples of the resultant second derivatives are shown in Figure 5.10D. Monolayer-poor samples (1.5-2 krpm) are dominated by one peak at ~1.98 eV while the monolayer-rich sample (S.C.1) is dominated by one peak at ~2.03 eV, with intermediate samples showing both components at the same time.

More information about the components was extracted by fitting the second derivatives by the second derivative of two Lorentzians. A Lorentzian can be written as (Equation 5.1):

$$L(E) = \frac{h}{[1 + (\frac{(E-E_0)}{w/2})^2]} \tag{5.1}$$

where:

h - represents the height,

E_0 - centre and w the fwhm.

Differentiating two Lorentzians twice was used to fit the experimental data and to extract the height, width and centre of the two peaks.

In all cases, the applied procedure fit the data very well. The higher energy component always had a position of $\mathrm{E}_0 = 2.033$ eV consistent with absorbance of the monolayer A-exciton. The lower energy component was found to be between 1.98 and 1.997 eV. It is associated with the individually, unresolvable sum of few-layer A-exciton absorptions. In fact, the monolayer component can be differentiated from the few-layers only because of the logarithmic dependence. It implies, that the energy difference between A-excitonic transitions for 1- and 2- layer nanosheets are 19 meV while being only 11 meV between 2- and 3-layer nanosheets and 8 meV between 3- and 4-layer nanosheets.

Next, it was observed and presented in Figure 5.10E that the width of the monolayer A-exciton absorbance peak is invariant with the width of the nanosheet thickness distribution. In fact, the monolayer peak is always ~55 meV wide. Thus, the width of the few-layer A-exciton absorbance peak should increase as the thickness distribution broadens and in fact, the FL peak width increases from ~65 to ~110 meV as the AFM thickness histogram width increases from 1 to 4.5

With this peak assignment in mind, we propose that the area under the ML A-exciton extinction peak should scale with the monolayer content in the dispersion. Because it is proportional to h × w, we have calculated the metric $\mathrm{S_A}$ which we suggest should scale with the monolayer volume fraction (Equation 5.2).

$$S_A = \frac{h_{ML}w_{ML}}{h_{ML}w_{ML} + h_{FL}w_{FL}} \tag{5.2}$$

In Figure 5.10F, we plot $\mathrm{S_A}$ versus $\mathrm{V_f}$ for a range of samples finding good linearity as described by $\mathrm{S_A} = (0.8 \pm 0.05)\mathrm{V_f}$. As a result, $\mathrm{S_A}$ can be used as an alternative metric for the monolayer volume fraction determination according to the equation below (Equation 5.3).

$$V_f = (1.25 \pm 0.008)S_A \tag{5.3}$$

The availability of having highly monolayer-enriched dispersions allows us to measure the photoluminescence using a standard PL spectrometer. As shown in Figure 5.10G, emission from the A-exciton can be well resolved with the fitting of the emission spectrum giving position and widths virtually identical to those measured in the Raman spectrometer. The real advantage of measurement with the PL spectrometer is the ability to measure excitation spectra. Such spectra allow the measurement of the absorption spectrum of the luminescent species at a higher resolution than would usually be possible. As can be seen in Figure 5.10H, the excitation spectrum rougly follows the extinction/absorbance spectrum, but with sharper peaks, in particular in the case of the B-exciton. As an inset in Figure 5.10I , we also compare the measured PL spectrum with the deconvoluted A-exciton absorbance contributions from mono- and few-layer WS_2. The monolayer A- exciton absorbance is very close to the PL with only a slight Stokes shift ($\sim$10 meV). We find a strong dependence on layer number with the A-exciton shifting from 2.06 eV for the ML to 1.99 eV in the bilayer

In summary, the Secondary Liquid Cascade Centrifugation presented is a simple, powerful and broadly applicable technique to separate liquid-exfoliated nanosheets by thickness. Cascades can be designed to produce the desired size and thickness distributions and the required degree of monolayer enrichment. Although the achievements are very impressive, the enrichment process is limited by the initial number of monolayers present in the sample volume, monolayers geometry, time scale as well as the limits due to available equipment (rotation speed). Ultimately, we believe that cascades will be designed to produce dispersions containing only a given nanosheet thickness at a predetermined lateral size. Also, this technique can be applied to virtually any 2D material stabilised by solvents, surfactants or polymers using only benchtop centrifuges.

Chapter 6

Films

6.1 Introduction

WS_2 semiconducting nanosheets described in detail in chapter 3 exhibit unique size-dependent optical properties [108]. They are a promising material for future electronics applications. Although they exhibit desirable properties, there is a significant drawback associated with being dispersed in a liquid. For many device applications, such as transistors, it is required that the materials must be in solid form, what is challenging to achieve without quenching the optical properties. In the following chapter, a simple and efficient method of transferring WS_2 from liquid dispersion into PMMA matrix is described. Not only were nanosheets successfully transferred and optically homogeneous films produced, but also the nanosheet monolayer properties such as photoluminescence were maintained at a high level with no significant intensity reduction. A new road for TMDC films is thus opened up, allowing them to be integrated into real life devices in order to make use of their outstanding properties.

6.1.1 WS_2 Dispersions Preparation.

WS_2 dispersions were prepared by probe sonicating powder (Sigma Aldrich, order number 243639-50G, initial concentration 30 g/l) in an aqueous surfactant solution (sodium cholate, SC, Sigma Aldrich) with a procedure similar to that described in subsection 6.1.1. This time WS_2 powder was immersed in 80 ml of an aqueous surfactant solution (C_{SC} = 6 g/l) in a 100 ml metal beaker. The beaker was mounted in a water bath connected to a chiller system maintaining the external temperature at 5 °C. A solid flathead sonication tip was lowered to the bottom of the beaker and then raised 1 cm from it. The mixture was probe sonicated (Sonics VXC-500) for 1 h at 60 % amplitude with a pulse of 4 s on and 2 s off. The dispersion was centrifuged in $50ml$ aliquots using 50 lL vials in a Hettich Mikro 220R centrifuge equipped with a fixed-angle rotor 1016 at 6 krpm (2660 g) for 1.5 h. The supernatant was discarded. The sediment was collected and redispersed in 80 mL of a fresh surfactant (C_{SC} = 2 g/l) solution and subjected to a second sonication using the solid flathead tip for 5 h at 60 % amplitude with a pulse of 4 s on and 4 s off. Again, the two-step sonication procedure was applied, as it yields a higher concentration of exfoliated WS_2 and removes impurities from the starting powder otherwise accumulated in the dispersion. The dispersion prepared this way is called a "stock dispersion".

To select nanosheets by size, we used liquid cascade centrifugation (Beckman Coulter Avanti XP centrifuge, 15 °C) with sequentially increasing rotation speeds (method described in details in subsection 3.2.2).

The stock dispersion was first transferred into four vials and centrifuged for 2 hrs at 1k g. The sediment containing unexfoliated and very large/thick nanosheets was discarded, and the supernatant transferred into six vials and centrifuged for 2 hrs at 5k g. This time sediment was collected and labelled as "1-5k g WS_2". The supernatant was again transferred equally into 6 vials and centrifuged for 2 hrs at

22k *g*. The sediment was collected and labelled as “5-22k *g* WS_2” and supernatant discarded. Both “1-5k g” and “5-22k g” samples were taken into further experiments described in following sections of this chapter (subsection 6.1.1).

6.1.2 Water to Polymer Transfer

Both WS_2 dispersions – “1-5k g” and “5-22k g” (size selected as described in 7.1.1) were processed in parallel to form solid WS_2 films. Since they were both H_2O-SC based dispersions, it was necessary to formulate a multi-step protocol to; one decrease the surfactant (SC) concentration to as low as possible (close to 0 g/l); two, replace H_2O with a solvent compatible and favourable for spin coating; three increase WS_2 concentration as much as possible.

This was achieved through multiple centrifugations in two steps, where the first one can be considered as “cleaning & concentration” and the second one as “transfer”. The scheme of the procedure is presented in Figure 6.1 and described in details below.

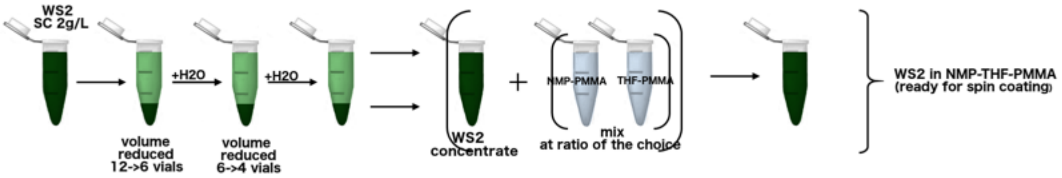

Figure 6.1: General scheme of WS_2 nanosheet transfer from H_2O-SC dispersion into PMMA-THF-NMP

Washing and concentrating of WS_2: The 18 ml of “1-5k *g* WS_2” and “5-22k *g* WS_2” were transferred equally into 12 vials (1.5 ml Eppendorf centrifuge tubes) and subjected to centrifugation (Hettich Mikro 220R, 15○C, 1195-A fixed angle rotor) at 22k *g* for 3 h. The sediment was redispersed in H_2O with reduced volume to a total of 6 (1.5 ml) vials. This sample was again centrifuged at 22k *g* for 3 h and the sediment collected in H_2O with reduced volume to a total of 4 (1.5 ml) vials. This washing was repeated a third time after which the WS_2 was redispersed in only 1.5 ml and referred to as “WS_2 concentrate”.

Transfer: First, PMMA (350,000 Mw) was dissolved in both NMP and THF at a concentration of 30 gl^{-1}, respectively, by stirring. The NMP-PMMA and THF-PMMA were mixed at a ratio of 2:5 giving a NMP-THF-PMMA medium that can readily be spin-coated. To transfer WS_2 into the NMP-THF-PMMA solution, the WS_2 concentrate, as well as the NMP-THF-PMMA polymer solution were bath sonicated for $\sim 1min$. Finally, the WS_2 concentrate was injected to the NMP-THF-PMMA at the concentration of choice and gently sonicated to avoid any aggregation

6.2 WS_2-PMMA-NMP-THF - Liquid Characterization

After successfully transferring WS_2 from H_2O-SC into the PMMA-NMP-THF based medium, it was crucial to characterise the final dispersion and compare it with the initial one. This step was important, as the goal is to maintain the initial favourable features of WS_2 nanosheets present in the H_2O-SC based dispersion after transfer into PMMA-NMP-THF and afterwards into the final film. To do so, it was necessary to track any changes at each step of the procedure.

To confirm the presence of the desired properties of the dispersions before and after transfer, the samples were subjected to UV-Vis Spectroscopy (Extinction and Absorption), AFM and Raman/PL measurements.

The powerful tool of extinction spectroscopy was used to characterise the 2D nanosheet dispersions (pre- and post-transfer dispersions of both sizes, Figure 6.2). As described in the previous chapters, the observed changes in the spectral profile are correlated to the nanosheet size and thickness due to edge and confinement effects.

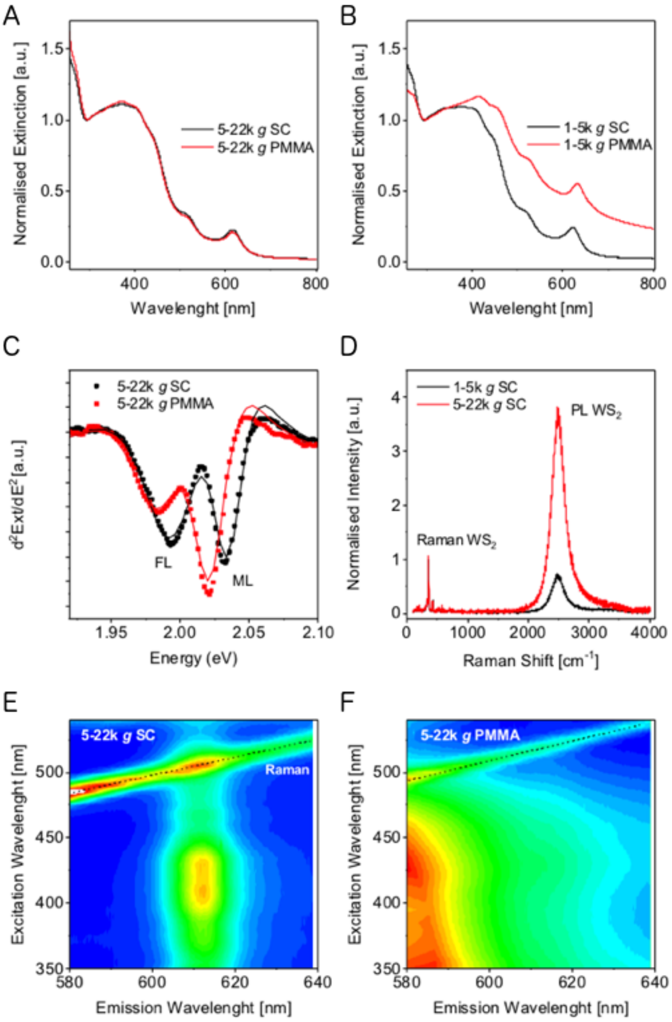

Figure 6.2: **A)** Normalised extinction spectra of WS_2 dispersion trapped in a range of 5-22k g in H_2O (before transfer) and THF-NMP-PMMA (after transfer). **B)** Normalised extinction spectra of WS_2 dispersion trapped in a range of 1-5k g in H_2O (before transfer) and in THF-NMP-PMMA (after transfer). **C)** 2^{nd} derivative of the A-exciton peak for WS_2 dispersion trapped in a range of 5-22k g in H_2O (before transfer) and in THF-NMP-PMMA (after transfer). **D)** Raman / PL spectrum of WS_2 H_2O-SC dispersions trapped in a range of 1-5k g and 5-22k g. **E)** Photoluminescence excitation emission contour plot of the WS_2 dispersion in H_2O-SC. **F)** Photoluminescence excitation emission contur plot of the WS_2 dispersion in THF-NMP-PMMA

In brief, extinction intensity ratios can be used to express lateral size, while peak positions (in SC) can be used to assess the nanosheet layer number.

In Figure 6.2A-B, extinction spectra of small (5-22k g, A) and larger (1-5k g, B) WS_2 nanosheets are shown before and after transfer to the organic polymer solution.

According to previously established metrics, nanosheet lengths were calculated to be 46 nm and 59 nm respectively. The lateral dimensions of WS_2 nanosheets were also confirmed by statistical AFM (Figure 6.3) according to the procedure described in details in section 3.2.5.

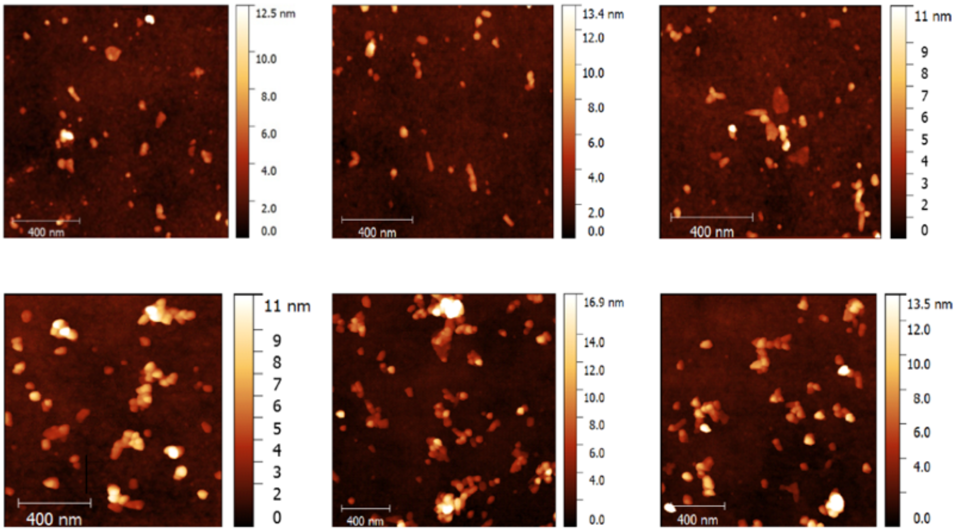

Figure 6.3: AFM characterisation of the dispersion; 5-22 kg – top row (3 example images), 1-5 kg – bottom row (3 example images)

After the transfer, no significant changes were found in the extinction spectrum of "5-22k g" sample. In contrast, an increased non-resonant scattering background ($>$ 650 nm) was observed for the "1-5k g" sample suggesting reaggregation in the case of larger/thicker WS_2 (Figure 6.2A-B).

In order to evaluate more clearly whether reaggregation occurred also in the smaller/thinner "5-22k g" sample, the second derivative of the A-exciton region of the extinction spectra (1.9 – 2.1 eV) is analysed, as it shows separate peaks for monolayered (ML) and fewlayered (FL) WS_2, respectively. For the "5-22k g" sample (Figure 6.2C), the ML component is still clearly discernible after the transfer suggesting negligible aggregation. Both monolayer and few-layer components are red-shifted in the organic polymer solution compared to the aqueous SC reference system due to solvatochromic effects [56]. Importantly, the line-width of the monolayer component is still narrow. This confirms that the PMMA-THF-NMP solvent mixture is an excellent stabiliser for liquid-exfoliated WS_2.

When comparing the ML and FL contributions for the "5-22k *g*" and "1-5k *g*" samples, it is clear that the ML content is lower in the "1-5k *g*" sample as expected. The ML content is also reflected in the PL/Raman ratios (Figure 6.2D) which is 3.66:1 and 0.69:1, respectively. According to the previously established metrics (section 4.4.3) this corresponds to ML volume fractions of 21% and 4%, respectively, in the initial H_2O-SC based dispersions in good agreement with UV Vis. Unfortunately, PL/Raman ratios cannot be compared with the post transfer dispersions, as the THF evaporation is too rapid to maintain a constant focus during the measurement (section 3.2.3).

However, it is possible to gain insight into the photoluminescence from a measurements using a commercial PL spectrometer in the case of the monolayer-rich dispersion. The resultant excitation-emission contour plots of the "5-22k *g*" sample before and after transfer are shown in Figure 6.2E-F. In the H_2O-SC dispersion, the characteristic ML WS_2 PL is observed at 612 nm. This is no longer the case after transfer due to solvent signal masking the WS_2 PL (Figure 6.2F).

6.2.1 Liquid to Solid (Film) Transfer

The transfer procedure described above, results in two high quality monolayer-rich WS_2 dispersions in an organic solvent/polymer mixture that is compatible with spin coating. The production of the WS_2-PMMA films is described below.

WS_2 films were prepared on glass (SCHOTT) substrates with a size of 1.5*2 cm which also determined the area of the WS_2 films. The spin coating procedure was performed under argon atmosphere. The WS_2-THF-NMP-PMMA dispersions (section 7.1.2) were bath sonicated for 3 minutes to remove any inhomogeneity or aggregates.

To create one WS_2-PMMA film, a drop (50 μL) of the dispersion was placed in the middle of the substrate, possibly evenly covering the surface and then spin coated. To spread the THF-NMP-PMMA dispersion on the glass substrate with minimal waste, a statical spin coating with two steps of spinning was applied. Those were the 30s 700 rpms (step 1) and 20s 1000rpm (step 2). The films were left to dry overnight in dehumidified air, as moisture was found to introduce haze into the film.

6.3 WS_2-PMMA – Films Characterization

The dried WS_2-PMMA films were characterised to assess both the film quality (e.g. homegeity, surface roughness) and to compare the optical properties of the WS_2-PMMA films with the initial WS_2-SC dispersions. Results are summarised in Figure 6.4.

The WS_2-PMMA films were characterised by UV-Vis spectroscopy by measuring both absorption and extinction spectra (Figure 6.4A-B). The extinction and absorption spectra are very similar with a negligible scattering contribution in extinction. This confirms the high optical quality of the films. Extinction spectra were also smoothed, and 2^{nd} derivatives were calculated (Figure 6.4A-B insets) showing that contributions of both FL and ML are present in the WS_2 films. The FL contribution peak is found at 1.993 eV in both films and the ML contribution at 2.027 eV. As expected, the ML peak is more pronounced in the "5-22k *g*" sample. Importantly, the ratio of monolayer/fewlayer area is comparable to the initial dispersion suggesting minimal reaggregation throughout the transfer and film formation process. In addition, it should be mentioned that the monolayer peak position is also very similar to the initial dispersion. In fact, the red-shift observed in the WS_2-PMMA-THF-NMP is reversed suggesting that PMMA has a negligible solvatochromic effect as opposed to the NMP-THF mixture.

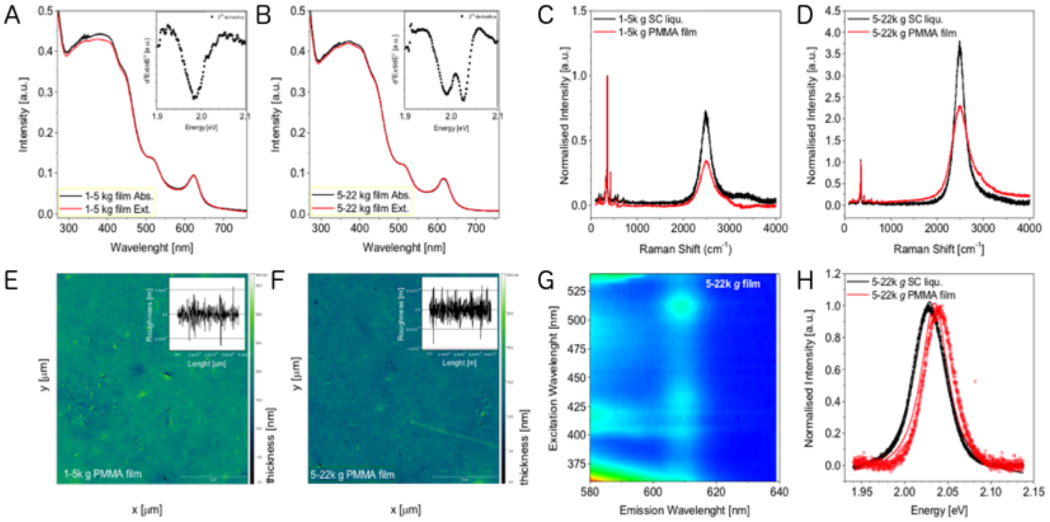

Figure 6.4: **A)** Absorption and extinction spectra of WS_2-PMMA film infused with WS_2 nanosheets trapped in a range of 1-5k g, Inset: 2nd derivative of A-exciton. **B)** Absorption and extinction spectra of WS_2-PMMA film infused with WS_2 nanosheets trapped in a range of 5-22k g, Inset: 2nd derivative of A-exciton. **C&D)** AFM of the WS_2-PMMA films surface made of the WS_2 dispersions trapped between 1-5k g **(C)** and 5-22k g **(D) Insets (C)&(D):** Roughness across the surface of the film. **E)** Raman / PL spectra of the WS_2-PMMA film infused with WS_2 nanosheets trapped between 1-5k g compared to the corresponding initial dispersion in H_2O-SC. **F)** Raman / PL spectra of WS_2-PMMA film infused with WS_2 nanosheets trapped between 5-22k g compared to the corresponding initial dispersion in H_2O-SC. **G)** Photoluminescence excitation emission contour plot of WS_2-PMMA film made of the WS_2 dispersions trapped between 5-22k g. **H)** Photoluminescence spectra of WS_2-SC dispersion and WS_2-PMMA film 5-22k g, excitation 430 nm). The solid lines are Lorentzian fits

As a handle to control the optical density of the WS_2 in the film, the optical density (OD) of the corresponding dispersions (Figure 6.5A-C) can be used as a guide. In general, it is found that the optical density of the WS_2 in the film scales with the concentration in the dispersion, but gives optical densities lower by ∼ 3 orders of magnitude (Figure 6.5C). In the final films, ODs as high as ∼0.1 at the A-exciton are achievable resulting in films of yellow-greenish colour which are robust and have a homomogeneous surface as shown by scanning electron microscopy (except at edges, SEM, Figure 6.6). Higher optical densities under these processing conditions are not accessible, as the nanosheets aggregate in the dispersion at higher concentrations.

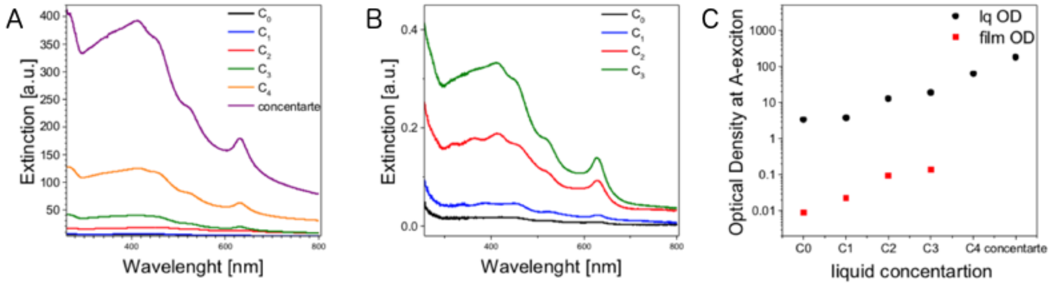

Figure 6.5: **A)** Extinction spectra of THF-PMMA-WS_2 dispersions with different WS_2 contents; WS_2 trapped 1-5k g. **B)** Extinction spectra of WS_2-PMMA films made out of the corresponding dispersions. **C)** The optical density of the THF-NMP-WS_2 dispersions and the corresponding WS_2-PMMA films at A-exciton position

The negligible scattering in the films suggests that the films surface is relatively smooth. SEM (Figure 6.6) confirms that the films are uniform over wide areas. To gain more insights with a higher resolution, AFM was performed on both films (Figure 6.4C-D). A 10*10 μm^2 surface was scanned to calculate the roughness of the films. This yielded estimated roughness values of 0.18 nm for the “1-5k g” WS_2 films and only 0.11 nm for the “5-22k g” WS_2 film (insets Figure 6.4C-D). These values confirm that films are very smooth and uniform and are comparable to pure polymer films without nanomaterial. Note that such a smooth surface over areas of >100 μm^2 is sufficient for many optical applications.

To test whether the WS_2 monolayers retain their optical properties in the thin film, Raman/photoluminescence spectroscopy (Raman/PL) was performed with 532 nm excitation wavelength and low as possible laser power (to avoid heating). Figure 6.4C-D shows the Raman/PL spectra of the films compared to the corresponding Raman/PL spectra of the aqueous dispersions (N.B. this measurement was not possible in the organic solvent mixture). The PL:Raman ratio decreased slightly for films when compared to the liquid SC dispersion. Also, the PL peaks broaden in the films. This could be either due to heating in the film, reaggregation, inhomogeneous broadening or doping from the polymer. Since there is no asymmetry or peak shift

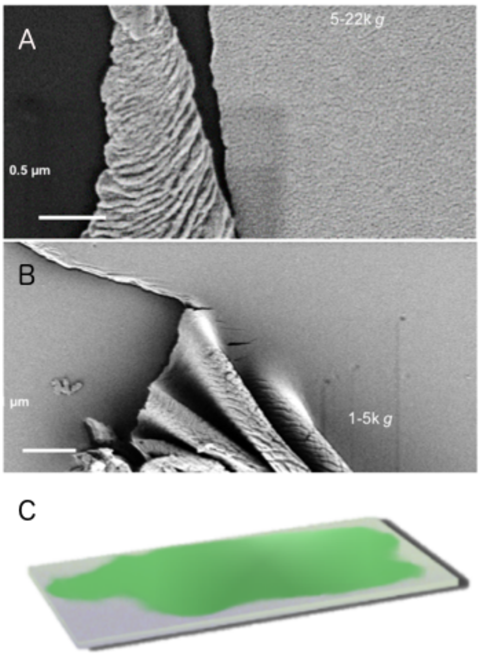

Figure 6.6: SEM characterisation of the surface of the film; **A)** 5-22 kg, **B)**1-5 kg **C)** film visualisation over the substrate

observed, it is suggested that potential doping from the polymer is negligible, as this would likely result in a pronounced contribution from trions[34], [85]. Importantly, while the PL intensity is lower, the peak broadens. Thus, the area stays roughly constant which would not be the case if pronounced reaggregation occurred.

To test whether the broadening of the PL is more likely due to heating or inhomogeneous broadening from a non-uniform polymer surrounding, the films were subjected to photoluminescence measurements in a conventional PL spectrometer, where heating can be excluded due to the lower excitation power. Note that such a measurement is only possible on optically homogeneous films, where artefact from scattering are surpressed. An example contour plot map corresponding to sample "5-22k g" is presented in Figure 6.4G. Photoluminescence excitation emission contour plots were acquired at same conditions as ones for liquid dispersion of WS_2 (Figure 6.2E-F). Photoluminescence features are again visible and well defined. The features are the same as for the aqueous dispersion, but complemented by minor horizontal artefacts due to the measurement in the films. Moreover, single emission spectra were acquired for both the liquid aqueous dispersion and the resultant polymer film (Figure 6.4H). Contrary to the Raman/PL measurement, there is no red-shifting or broadening of the PL in films. This suggests that heating influenced Raman/PL spectra. Importantly, this measurement confirms that optical properties of the monolayer WS_2 are pristine in the film. The spectra can be fitted well to a single Lorentzian, again suggesting minimal doping from PMMA stabiliser in a thin film. In conclusion, the elaborated transfer and film formation procedure gives access to pristine properties in thin films produced from LPE ideal for optics applications and potentially electronic applications, if a non insulating polymer matrix was used.

Chapter 7

Conclusions

The work presented in this thesis is a modest contribution to the collective efforts of the researchers interested in 2D nanomaterials all over the world. It aimed to contribute to the understanding of the optical properties of 2D materials – especially WS_2 – via liquid exfoliation, size selection and exploration of the fundamental linear and nonlinear properties of the nanosheets in dispersion. Finally, a strategy to preserve the (monolayer) properties of the WS_2 nanosheets in liquid dispersions in polymer composite films was elaborated with minimal reaggregation.

Each experimental chapter of that thesis addressed a single independent problem on the way to exploit the properties of (monolayer-enriched) WS_2 produced in bulk quantities from liquid exfoliation. WS_2 served as a model 2D material, but it is expected that the learnings are transferrable to other 2D materials.

The work described in chapter WS_2 – High-Quality Liquid Exfoliated Nanosheets (chapter 3) aimed for the preparation of state of the art nanosheets dispersions of WS_2 in aqueous SC. This was done by optimisation of already known LPE protocols. The liquid cascade centrifugation was established as powerful tool to size-select initially produced so called “stock dispersion” with minimal material wastage. In that way, 8 reasonably narrow size/thickness distribution WS_2 dispersions were isolated. Their lateral dimensions ranging between 175-35 nm (length) and 7.1-2.2 (layers) were quantitatively determined by statistical atomic force microscopy and transmission electron microscopy. Further, the linear optical properties of these well-defined WS_2 dispersions were characterised. A combination of the microscopic and spectroscopic data lead to the development of empirical equations to quantify the mean nanosheet length and thickness based on the shape of extinction spectra due to edge and confinement effects as previously shown for MoS_2 [44]. Also, another empirical equation to extract the monolayer content in the given dispersion was presented. This was based on the Raman/PL spectroscopy data, as only monolayered WS_2 exhibits appreciable fluorescence, while all WS_2 nanosheet units contribute to the Raman spectra. For the first time, it was shown that monolayer content can be determined by statistical AFM imaging and analysis, if sufficient numbers of nanosheets are recorded (~ 350 in the case of polydisperse samples).

The mentioned metrics equations based on extinction spectroscopy were also proven to be mostly transferable from aqueous into NMP environment with only minor adjustments accounting for solvatochromic effects. That makes them extremally flexible and useful for future work excluding the necessity of time-consuming imaging to determine lateral dimensions of the WS_2 nanosheets or their thickness. Last but not least, the production of monolayer-rich LPE WS_2 enabled first insights into the chemical degradation of these nanosheets in the environment. The ageing process of WS_2 nanosheets in aqueous SC dispersions was studied via PL spectroscopy. Although the PL vanishes/changes over time presumably due to the reaction with water and oxygen, an easy and efficient prevention technique has been found related to reducing the storage temperature.

The chapter Nonlinear Optical Characterization (chapter 4) deals with the mechanisms behind the NLO properties of WS_2 and alike nanomaterials which is in its nature complicated and complex. In many cases, it is influenced by a variety of factors from which the most important is the incident laser pulse and the intrinsic properties of the nanomaterials[56], [78]. The size-dependent saturable absorption and optical limiting capacity of the WS_2 nanosheets in the aqueous SC dispersions have been presented and described. Significant ultrafast NLO properties of the layered WS_2 nanosheets suggest a great promise in the development of nanophotonic devices. Its strength is not only in the NLO behaviour of exfoliated WS_2 dispersions but also in flexibility of the material postprocessing. [56], [78]. The size-dependent saturable absorption and optical limiting capacity of the WS_2 nanosheets in the aqueous SC dispersions have been presented and described. Significant ultrafast NLO properties of the layered WS_2 nanosheets suggest a great promise in the development of nanophotonic devices. Its significance is not only in the exfoliated WS_2 dispersions' NLO properties itself but its flexible high expandability of the material in its form.

The WS_2 - Monolayer Enrichment of Liquid Dispersions part (chapter 5) describes the efforts taken to monolayer enrich standard WS_2 dispersion through the post processing by centrifugation. Starting with the initial "stock dispersion," multiple approaches were taken with a view to meet that goal. It includes homogeneous centrifugation, repeated cascading and finally complex secondary cascades. That let us to achieve dispersions with monolayer content as high as $\sim 75\%$ (and reasonable nanosheet lateral size) out of the starting 4% which is undoubtedly a significant improvement.

Last but not least, the chapter Films (chapter 6) describes an approach to transfer WS_2 nanosheets suspended in aqueous SC into PMMA based composites in thin films of high optical quality. By transferring high quality aqueous surfactant dispersions to organic solvent-PMMA mixtures, spin-coating was accessible as deposition technique. From a WS_2-PMMA-NMP-THF mixture, high-quality WS_2-PMMA films with OD of ~ 0.1 were prepared. Not only are they uniform and smooth but simultaneously, the pristine properties of the initial WS_2 material (including monolayer photoluminescence) were preserved.

In the process, first of all we have learned how to make high quality samples by using spectroscopic metrics. Further the size depenedent optical (linear and nonlinear) properties were investigated and described through the empirical equations. This knowledge is not only applicable to WS_2 but can be transferred to other 2D materials as well.

While well defined state of the art preparation protocole was estabilished the degradation process was studied through the optical meausrements.

The WS_2 dispersions were successfully transferred into PMMA polymer matrix retaining the pristine WS_2 properties in a such. The method is transferrable and flexible so other matrices for deposition can be used. Presented findings are a proof of concept that the properties of liquid WS_2 disperions can be retained in a solid film.

The next step would be to on demand mix and match both matrix and active material as required for certain applications. A semiconducting polymer matrix can be used for LEDs. A conductive matrix (PEDOT-PSS & graphene, below percolation threshold) as an aid to increase network conductivity and composites with donors and acceptors for improved photoconductors. Starting with such a high-quality dispersion, a variety of derivatives like filtrated films, polymer composites can be prepared. The ability to preserve the dispersions properties, satisfies requirements for multiple applications in photonic and electronic devices.

Bibliography

Articles

[1] N. Peimyoo, W. Yang, J. Shang, X. Shen, Y. Wang, and T. Yu, “Chemically driven tunable light emission of charged and neutral excitons in monolayer ws 2,” vol. 8, no. 11, 1132. DOI: 10.1021/nn504196n.

[2] L. Pauling, “The structure of the chlorites,” *Proceedings of the National Academy of Sciences of the United States of America*, vol. 16, no. 9, 1930, ISSN: 0027-8424. DOI: 10.1073/pnas.16.9.578.

[3] M. Skribljak, a. Dasgupta, and a. B. Biswas, “The crystal structure of cadmium indate,” *Acta Crystallographica*, vol. 12, no. 12, pp. 1049–1050, 1959, ISSN: 0365110X. DOI: 10.1107/S0365110X59002924.

[4] K. K. Kam and B. A. Parkinson, “Detailed photocurrent spectroscopy of the semiconducting group vib transition metal dichalcogenides,” *The Journal of Physical Chemistry*, vol. 86, no. 4, pp. 463–467, 1982, ISSN: 0022-3654. DOI: 10.1021/j100393a010.

[5] E. F. Meyer, “Textbook forum. thermodynamics of mixing of ideal gases: A persistent pitfall,” *Journal of Chemical Education*, vol. 64, no. 8, p. 676, 1987, ISSN: 0021-9584. DOI: 10.1021/ed064p676.

[6] M. Sheik-bahae, a. a. Said, and E. W. Van Stryland, "High-sensitivity, single-beam n2 measurements," *Optics Letters*, vol. 14, no. 17, p. 955, 1989, ISSN: 0146-9592. DOI: 10.1364/OL.14.000955.

[7] M. Sheik-Bahae, A. Said, T.-H. Wei, D. Hagan, and E. Van Stryland, "Sensitive measurement of optical nonlinearities using a single beam," *Quantum Electronics, IEEE Journal of*, vol. 26, no. 4, pp. 760–769, 1990, ISSN: 0018-9197. DOI: 10.1109/3.53394.

[8] K. Fukami, "19 9 2 nature publishing group," vol. 359, pp. 150–152, 1992.

[9] F. Henari, ", j," vol. 199, no. 1, 1992.

[10] D. G. McLean, R. L. Sutherland, M. C. Brant, D. M. Brandelik, P. A. Fleitz, and T. Pottenger, "Nonlinear absorption study of a c60-toluene solution.," *Optics letters*, vol. 18, no. 11, p. 858, 1993, ISSN: 0146-9592. DOI: 10.1364/OL.18.000858.

[11] L. E. E. W. Tutt, T. F. Boggess, and E. K. Company, "A review of optical limiting mechanisms and devices using organics , fullerenes , semiconductors and other materials," vol. 17, pp. 299–338, 1993.

[12] M. Scalora, J. P. Bowling, and C. M. Bowden, "Letters 5," vol. 73, no. 10, pp. 1368–1371, 1994.

[13] J. W. Perry, K. Mansour, I.-Y. S. Lee, *et al.*, "Organic optical limiter with a strong nonlinear absorptive response," *Science*, vol. 273, no. 5281, pp. 1533–1536, 1996, ISSN: 0036-8075. DOI: 10.1126/science.273.5281.1533.

[14] M. Traving, M. Boehme, L. Kipp, M. Skibowski, F. Starrost, E. E. Krasovskii, A. Perlov, and W. Schattke, "Electronic structure of wse2: A combined photoemission and inverse photoemission study," *Physical Review B*, vol. 55, no. 16, pp. 10 392–10 399, 1997, ISSN: 0163-1829. DOI: 10.1103/PhysRevB.55.10392.

[15] L. Vivien, “Single-wall carbon nanotubes for optical limiting,” *Chemical Physics Letters*, vol. 307, pp. 317–319, 1999, ISSN: 00092614. DOI: `http://dx.doi.org/10.1016/S0009-2614(99)00528-X`.

[16] T. Boeker, R. Severin, A. Mueller, C. Janowitz, R. Manzke, D. Voss, P. Krueger, A. Mazur, and J. Pollmann, “Band structure of mos2, mose2, and alpha-mote2: Angle-resolved photoelectron spectroscopy and ab-initio calculations,” vol. 64, pp. 1–11, 2001, ISSN: 0163-1829. DOI: `10.1103/PhysRevB.64.235305`.

[17] G. Brusatin and R. Signorini, “Linear and nonlinear optical properties of fullerenes in solid state materials,” *Journal of Materials Chemistry*, vol. 12, no. 7, pp. 1964–1977, 2002, ISSN: 09599428. DOI: `10.1039/b202399g`.

[18] N. N. Lepeshkin, A. Schweinsberg, G. Piredda, R. S. Bennink, and R. W. Boyd, “Enhanced nonlinear optical response of one-dimensional metal-dielectric photonic crystals,” *Physical Review Letters*, vol. 93, no. 12, pp. 1–4, 2004, ISSN: 00319007. DOI: `10.1103/PhysRevLett.93.123902`.

[19] H. Rath, J. Sankar, V. PrabhuRaja, T. K. Chandrashekar, A. Nag, and D. Goswami, “Core-modified expanded porphyrins with large third-order nonlinear optical response,” *Journal of the American Chemical Society*, vol. 127, no. 33, pp. 11 608–11 609, 2005, ISSN: 00027863. DOI: `10.1021/ja0537575`.

[20] R. S. S. Kumar, S. V. Rao, L. Giribabu, and D. N. Rao, “Femtosecond and nanosecond nonlinear optical properties of alkyl phthalocyanines studied using z-scan technique,” *Chemical Physics Letters*, vol. 447, no. 4-6, pp. 274–278, 2007, ISSN: 00092614. DOI: `10.1016/j.cplett.2007.09.028`.

[22] S. D. Bergin, V. Nicolosi, P. V. Streich, *et al.*, “Towards solutions of single-walled carbon nanotubes in common solvents,” *Advanced Materials*, vol. 20, no. 10, pp. 1876–1881, 2008, ISSN: 09359648. DOI: `10.1002/adma.200702451`.

[23] S. Detriche, G. Zorzini, J.-F. Colomer, A. Fonseca, and J. B. Nagy, "Application of the hansen solubility parameters theory to carbon nanotubes," *Journal of Nanoscience and Nanotechnology*, vol. 8, no. 11, pp. 6082–6092, 2008, ISSN: 15334880. DOI: `10.1166/jnn.2008.SW16`.

[24] G. Giovannetti, P. A. Khomyakov, G. Brocks, V. M. Karpan, J. van den Brink, and P. J. Kelly, "Doping graphene with metal contacts," *Nature*, vol. 490, no. 7419, pp. 192–200, 2008, ISSN: 00280836. DOI: `10.1103/PhysRevLett.101.026803`. eprint: `0802.2267`.

[25] Y. Hernandez, V. Nicolosi, M. Lotya, *et al.*, "High yield production of graphene by liquid phase exfoliation of graphite," *Nature Nanotechnology*, vol. 3, no. 9, pp. 563–8, 2008, ISSN: 1748-3395. DOI: `10.1038/nnano.2008.215`.

[26] Q. Bao, H. Zhang, Y. Wang, Z. Ni, Y. Yan, Z. X. Shen, K. P. Loh, and D. Y. Tang, "Atomic-layer craphene as a saturable absorber for ultrafast pulsed lasers," *Advanced Functional Materials*, vol. 19, no. 19, pp. 3077–3083, 2009, ISSN: 1616301X. DOI: `10.1002/adfm.200901007`.

[27] J. N. Coleman, "Liquid-phase exfoliation of nanotubes and graphene," *Advanced Functional Materials*, vol. 19, no. 23, pp. 3680–3695, 2009, ISSN: 1616301X. DOI: `10.1002/adfm.200901640`.

[28] A. K. Geim, "Graphene: Status and prospects," *Science*, vol. 324, no. 5934, pp. 1530–1534, 2009, ISSN: 0036-8075. DOI: `10.1126/science.1158877`.

[29] M. Lotya, Y. Hernandez, P. J. King, *et al.*, "Liquid phase production of graphene by exfoliation of graphite in surfactant / water solutions liquid phase production of graphene by exfoliation of graphite in surfactant / water solutions," no. 11, pp. 3611–3620, 2009. DOI: `10.1021/ja807449u`.

[30] J. Wang and W. J. Blau, "Inorganic and hybrid nanostructures for optical limiting," *Journal of Optics A: Pure and Applied Optics*, vol. 11, no. 2, p. 024 001, 2009, ISSN: 1464-4258. DOI: 10.1088/1464-4258/11/2/024001.

[31] J. Wang, Y. Chen, and W. J. Blau, "Carbon nanotubes and nanotube composites for nonlinear optical devices," *Journal of Materials Chemistry*, vol. 19, no. 40, p. 7425, 2009, ISSN: 0959-9428. DOI: 10.1039/b906294g.

[32] J. Wang, Y. Hernandez, M. Lotya, J. N. Coleman, and W. J. Blau, "Broadband nonlinear optical response of graphene dispersions," *Advanced Materials*, vol. 21, no. 23, pp. 2430–2435, 2009, ISSN: 09359648. DOI: 10.1002/adma.200803616.

[33] S. D. Bergin, Z. Sun, P. Streich, J. Hamilton, and J. N. Coleman, "Supporting information for : New solvents for nanotubes : Matching the dispersability of surfactants," *The Journal of Physical Chemistry C*, vol. 3, no. C, pp. 1–8, 2010.

[34] U. Khan, A. ONeill, M. Lotya, S. De, and J. N. Coleman, "High-concentration solvent exfoliation of graphene," *Small*, vol. 6, no. 7, pp. 864–871, 2010, ISSN: 16136810. DOI: 10.1002/smll.200902066.

[35] M. Lotya, P. J. King, U. Khan, S. De, and J. N. Coleman, "High-concentration, surfactant-stabilized graphene dispersions," *ACS Nano*, vol. 4, no. 6, pp. 3155–3162, 2010, ISSN: 19360851. DOI: 10.1021/nn1005304.

[36] K. F. Mak, C. Lee, J. Hone, J. Shan, and T. F. Heinz, "Atomically thin mos2: A new direct-gap semiconductor," *Physical Review Letters*, vol. 105, no. 13, pp. 2–5, 2010, ISSN: 00319007. DOI: 10.1103/PhysRevLett.105.136805.

[37] A. Splendiani, L. Sun, Y. Zhang, T. Li, J. Kim, C. Y. Chim, G. Galli, and F. Wang, "Emerging photoluminescence in monolayer mos2," *Nano Letters*, vol. 10, no. 4, pp. 1271–1275, 2010, ISSN: 15306984. DOI: 10.1021/nl903868w.

[38] G. Xing, H. Guo, X. Zhang, T. C. Sum, and C. H. A. Huan, "The physics of ultrafast saturable absorption in graphene.," *Optics express*, vol. 18, no. 5, pp. 4564–73, 2010, ISSN: 1094-4087. DOI: `10.1364/OE.18.004564`.

[39] Z. Chen, D. Cummins, B. N. Reinecke, E. Clark, M. K. Sunkara, and T. F. Jaramillo, "Core-shell moo3-mos2 nanowires for hydrogen evolution: A functional design for electrocatalytic materials," *Nano Letters*, vol. 11, no. 10, pp. 4168–4175, 2011, ISSN: 1530-6984. DOI: `10.1021/nl2020476`.

[40] E.-Y. Choi, W. S. Choi, Y. B. Lee, and Y.-Y. Noh, "Production of graphene by exfoliation of graphite in a volatile organic solvent," *Nanotechnology*, vol. 22, no. 36, p. 365 601, 2011, ISSN: 0957-4484. DOI: `10.1088/0957-4484/22/36/365601`.

[41] J. N. Coleman, M. Lotya, A. ONeill, *et al.*, "Two-dimensional nanosheets produced by liquid exfoliation of layered materials.," *Science (New York, N.Y.)*, vol. 331, no. 6017, pp. 568–571, 2011, ISSN: 0036-8075. DOI: `10.1126/science.1194975`.

[42] Y. Ding, Y. Wang, J. Ni, L. Shi, S. Shi, and W. Tang, "First principles study of structural, vibrational and electronic properties of graphene-like mx2 (m=mo, nb, w, ta; x=s, se, te) monolayers," *Physica B: Condensed Matter*, vol. 406, no. 11, pp. 2254–2260, 2011, ISSN: 09214526. DOI: `10.1016/j.physb.2011.03.044`.

[43] J. Feng, X. Sun, C. Wu, L. Peng, C. Lin, S. Hu, J. Yang, and Y. Xie, "Metallic few-layered vs¡inf¿2¡/inf¿ ultrathin nanosheets: High two-dimensional conductivity for in-plane supercapacitors," *Journal of the American Chemical Society*, vol. 133, no. 44, pp. 17 832–17 838, 2011, ISSN: 00027863. DOI: `10.1021/ja207176c`.

[44] L. Katz, A. Donval, E. Zussman, and Y. Cohen, “Ordered carbon nanotubes for optical power limiting devices,” *ACS Applied Materials and Interfaces*, vol. 3, no. 12, pp. 4611–4618, 2011, ISSN: 19448244. DOI: 10.1021/am201015q.

[45] U. Khan, H. Porwal, A. O. Neill, P. May, and J. N. Coleman, “Solvent-exfoliated graphene at extremely high concentration solvent-exfoliated graphene at extremely high concentration,” no. June, pp. 9077–9082, 2011, ISSN: 07437463. DOI: 10.1021/la201797h.

[46] T. Korn, S. Heydrich, M. Hirmer, J. Schmutzler, and C. Schller, “Low-temperature photocarrier dynamics in monolayer mos2,” *Applied Physics Letters*, vol. 99, no. 10, 2011, ISSN: 00036951. DOI: 10.1063/1.3636402.

[47] M. B. M. Krishna, V. P. Kumar, N. Venkatramaiah, R. Venkatesan, and D. N. Rao, “Nonlinear optical properties of covalently linked graphene-metal porphyrin composite materials,” *Applied Physics Letters*, vol. 98, no. 8, pp. 2009–2012, 2011, ISSN: 00036951. DOI: 10.1063/1.3553500.

[48] A. Kuc, N. Zibouche, and T. Heine, “Influence of quantum confinement on the electronic structure of the transition metal sulfide ¡math display=”inline”¿ ¡mrow¿ ¡mi¿t¡/mi¿ ¡/mrow¿ ¡/math¿ s ¡math display=”inline”¿ ¡mrow¿ ¡msub¿ ¡mrow/¿ ¡mrow¿ ¡mn¿2¡/mn¿ ¡/mrow¿ ¡/msub¿ ¡/mrow¿ ¡/math¿,” *Physical Review B*, vol. 83, no. 24, p. 245 213, 2011, ISSN: 1098-0121. DOI: 10.1103/PhysRevB.83.245213.

[49] C. Mattevi, H. Kim, and M. Chhowalla, “A review of chemical vapour deposition of graphene on copper,” *J. Mater. Chem.*, vol. 21, no. 10, pp. 3324–3334, 2011, ISSN: 0959-9428. DOI: 10.1039/C0JM02126A.

[50] I. Navas, R. Vinodkumar, and V. P. Mahadevan Pillai, “Self-assembly and photoluminescence of molybdenum oxide nanoparticles,” *Applied Physics A:*

Materials Science and Processing, vol. 103, no. 2, pp. 373–380, 2011, ISSN: 09478396. DOI: 10.1007/s00339-011-6345-9.

[51] S.-l. M. Phototransistors, “Single-layer mos 2 phototransistors,” *ACS nano*, vol. 6, no. 1, pp. 74–80, 2011, ISSN: 1936-086X. DOI: 10.1021/nn2024557.

[52] RadisavljevicB, RadenovicA, BrivioJ, GiacomettiV, KisA, B. Radisavljevic, A. Radenovic, J. Brivio, V. Giacometti, and A. Kis, “Single-layer mos2 transistors,” *Nat Nano*, vol. 6, no. 3, pp. 147–150, 2011, ISSN: 1748-3387. DOI: http://www.nature.com/nnano/journal/v6/n3/abs/nnano.2010.279.html#supplementary-information.

[53] C.-J. Shih, A. Vijayaraghavan, R. Krishnan, *et al.*, “Bi- and trilayer graphene solutions,” *Nature Nanotechnology*, vol. 6, no. 7, pp. 439–445, 2011, ISSN: 1748-3387. DOI: 10.1038/nnano.2011.94.

[54] R. J. Smith, P. J. King, M. Lotya, *et al.*, “Large-scale exfoliation of inorganic layered compounds in aqueous surfactant solutions,” *Advanced Materials*, vol. 23, no. 34, pp. 3944–3948, 2011, ISSN: 09359648. DOI: 10.1002/adma.201102584.

[55] B. Zhou, L. Yang, F. Chen, M. Xu, T. Wu, G. Wu, X. Chen, and D. Feng, “Evolution of electronic structure in eu1-xlaxfe2as2,” *Journal of Physics and Chemistry of Solids*, vol. 72, no. 5, pp. 474–478, 2011, ISSN: 00223697. DOI: 10.1016/j.jpcs.2010.10.075.

[56] Z. Y. Zhu, Y. C. Cheng, and U. Schwingenschlogl, “Giant spin-orbit-induced spin splitting in two-dimensional transition-metal dichalcogenide semiconductors,” *Physical Review B - Condensed Matter and Materials Physics*, vol. 84, no. 15, pp. 1–5, 2011, ISSN: 10980121. DOI: 10.1103/PhysRevB.84.153402.

[57] A. Castellanos-Gomez, M. Poot, G. A. Steele, H. S. J. Van Der Zant, N. Agra??t, and G. Rubio-Bollinger, “Elastic properties of freely suspended mos

2 nanosheets," *Advanced Materials*, vol. 24, no. 6, pp. 772–775, 2012, ISSN: 09359648. DOI: 10.1002/adma.201103965.

[58] H. Fang, S. Chuang, T. C. Chang, K. Takei, T. Takahashi, and A. Javey, "High-performance single layered wse 2 p-fets with chemically doped contacts," *Nano Letters*, vol. 12, no. 7, pp. 3788–3792, 2012, ISSN: 15306984. DOI: 10.1021/nl301702r.

[59] S. Kim, A. Konar, W.-S. Hwang, *et al.*, "High-mobility and low-power thin-film transistors based on multilayer mos2 crystals," *Nature Communications*, vol. 3, p. 1011, 2012, ISSN: 2041-1723. DOI: 10.1038/ncomms2018.

[60] H. Li, Z. Yin, Q. He, H. Li, X. Huang, G. Lu, D. W. H. Fam, A. I. Y. Tok, Q. Zhang, and H. Zhang, "Fabrication of single- and multilayer mos 2 film-based field-effect transistors for sensing no at room temperature," *Small*, vol. 8, no. 1, pp. 63–67, 2012, ISSN: 16136810. DOI: 10.1002/smll.201101016.

[61] C. M, "Photoluminescence from chemically exfoliated mos2," *Nano Lett.*, vol. 12, no. 12, p. 526, 2012, ISSN: 1530-6992. DOI: Doi10.1021/Nl2044887.

[62] K. F. Mak, K. He, C. Lee, G. H. Lee, J. Hone, T. F. Heinz, and J. Shan, "Tightly bound trions in monolayer mos2," *Nature Materials*, vol. 12, no. 3, pp. 207–211, 2012, ISSN: 1476-1122. DOI: 10.1038/nmat3505.

[63] W. Sik Hwang, M. Remskar, R. Yan, *et al.*, "Transistors with chemically synthesized layered semiconductor ws 2 exhibiting 10 5 room temperature modulation and ambipolar behavior," *Applied Physics Letters*, vol. 101, no. 1, 2012, ISSN: 00036951. DOI: 10.1063/1.4732522.

[64] J. Wang, K.-S. Liao, D. Fruchtl, *et al.*, "Nonlinear optical properties of carbon nanotube hybrids in polymer dispersions," *Materials Chemistry and Physics*, vol. 133, no. 2-3, pp. 992–997, 2012, ISSN: 02540584. DOI: 10.1016/j.matchemphys.2012.02.003.

[65] Q. H. Wang, K. Kalantar-Zadeh, A. Kis, J. N. Coleman, and M. S. Strano, “Electronics and optoelectronics of two-dimensional transition metal dichalcogenides,” *Nature Nanotechnology*, vol. 7, no. 11, pp. 699–712, 2012, ISSN: 1748-3387. DOI: `10.1038/nnano.2012.193`.

[66] Q. H. Wang, K. Kalantar-Zadeh, A. Kis, J. N. Coleman, and M. S. Strano, “Electronics and optoelectronics of two-dimensional transition metal dichalcogenides,” *Nature Nanotechnology*, vol. 7, no. 11, pp. 699–712, 2012, ISSN: 1748-3387. DOI: `10.1038/nnano.2012.193`.

[67] W. S. Yun, S. W. Han, S. C. Hong, I. G. Kim, and J. D. Lee, “Thickness and strain effects on electronic structures of transition metal dichalcogenides: 2h-¡math display=”inline”¿ ¡mrow¿ ¡mi¿m¡/mi¿ ¡msub¿ ¡mi¿x¡/mi¿ ¡mn¿2¡/mn¿ ¡/msub¿ ¡/mrow¿ ¡/math¿ semiconductors (¡math display=”inline”¿ ¡mi¿m¡/mi¿ ¡/math¿ ¡math,” *Physical Review B*, vol. 85, no. 3, p. 033 305, 2012, ISSN: 1098-0121. DOI: `10.1103/PhysRevB.85.033305`.

[68] A. Berkdemir, H. R. Gutierrez, A. R. Botello-Mendez, *et al.*, “Identification of individual and few layers of ws2 using raman spectroscopy,” *Scientific Reports*, vol. 3, no. 1, p. 1755, 2013, ISSN: 2045-2322. DOI: `10.1038/srep01755`.

[69] M. Chhowalla, H. S. Shin, G. Eda, L.-J. Li, K. P. Loh, and H. Zhang, “The chemistry of two-dimensional layered transition metal dichalcogenide nanosheets,” *Nature Chemistry*, vol. 5, no. 4, pp. 263–275, 2013, ISSN: 1755-4330. DOI: `10.1038/nchem.1589`.

[70] H. R. Gutie, N. Perea-lo, A. Laura, A. Berkdemir, B. Wang, and M. Terrones, “Extraordinary room-temperature photoluminescence in triangular ws 2 monolayers,” 2013, ISSN: 1530-6992. DOI: `10.1021/nl3026357`.

[71] J. M. Hughes, D. Aherne, and J. N. Coleman, “Generalizing solubility parameter theory to apply to one- and two-dimensional solutes and to incorporate

dipolar interactions," *Journal of Applied Polymer Science*, vol. 127, no. 6, pp. 4483–4491, 2013, ISSN: 00218995. DOI: 10.1002/app.38051.

[72] G.-H. Lee, Y.-J. Yu, X. Cui, *et al.*, "Flexible and transparent mos 2 field-effect transistors on hexagonal boron nitride-graphene heterostructures," *ACS Nano*, vol. 7, no. 9, pp. 7931–7936, 2013, ISSN: 1936-0851. DOI: 10.1021/nn402954e.

[73] O. Lopez-Sanchez, D. Lembke, M. Kayci, A. Radenovic, and A. Kis, "Ultrasensitive photodetectors based on monolayer mos2," *Nature Nanotechnology*, vol. 8, no. 7, pp. 497–501, 2013, ISSN: 1748-3387. DOI: 10.1038/nnano.2013.100.

[74] N. Mao, Y. Chen, D. Liu, J. Zhang, and L. Xie, "Solvatochromic effect on the photoluminescence of mos2 monolayers," *Small*, vol. 9, no. 8, pp. 1312–1315, 2013, ISSN: 16136810. DOI: 10.1002/smll.201202982.

[75] V. Nicolosi, M. Chhowalla, M. G. Kanatzidis, M. S. Strano, and J. N. Coleman, "Liquid exfoliation of layered materials," *Science*, vol. 340, no. 6139, pp. 1 226 419–1 226 419, 2013, ISSN: 0036-8075. DOI: 10.1126/science.1226419.

[76] F. K. Perkins, A. L. Friedman, E. Cobas, P. M. Campbell, G. G. Jernigan, and B. T. Jonker, "Chemical vapor sensing with monolayer mos 2," *Nano Letters*, vol. 13, no. 2, pp. 668–673, 2013, ISSN: 1530-6984. DOI: 10.1021/nl3043079.

[77] H. Terrones, F. Lopez-Urias, and M. Terrones, "Novel hetero-layered materials with tunable direct band gaps by sandwiching different metal disulfides and diselenides," *Scientific Reports*, vol. 3, no. 1, p. 1549, 2013, ISSN: 2045-2322. DOI: 10.1038/srep01549.

[78] K. Wang, J. Wang, J. Fan, *et al.*, "Ultrafast saturable absorption of two dimensional mos2 nanosheets," *ACS nano*, vol. 7, no. 10, p. 9260, 2013. DOI: 10.1021/nn403886t.

[79] M. Yi, Z. Shen, X. Zhang, and S. Ma, "Achieving concentrated graphene dispersions in water/acetone mixtures by the strategy of tailoring hansen solubility parameters," *Journal of Physics D: Applied Physics*, vol. 46, no. 2, p. 025 301, 2013, ISSN: 0022-3727. DOI: 10.1088/0022-3727/46/2/025301.

[80] H. Zeng, G.-B. Liu, J. Dai, *et al.*, "Optical signature of symmetry variations and spin-valley coupling in atomically thin tungsten dichalcogenides," *Sci. Rep.*, vol. 3, no. 4, p. 1608, 2013, ISSN: 2045-2322. DOI: 10.1038/srep01608.

[81] F. Lepine, M. Y. Ivanov, and M. J. J. Vrakking, "Attosecond molecular dynamics: Fact or fiction?" *Nature Photonics*, vol. 8, no. 3, pp. 195–204, 2014, ISSN: 1749-4885. DOI: 10.1038/nphoton.2014.25.

[82] M. Okada, T. Sawazaki, K. Watanabe, T. Taniguch, H. Hibino, H. Shinohara, and R. Kitaura, "Direct chemical vapor deposition growth of ws2 atomic layers on hexagonal boron nitride," *ACS Nano*, vol. 8, no. 8, pp. 8273–8277, 2014, ISSN: 1936086X. DOI: 10.1021/nn503093k.

[83] K. R. Paton, E. Varrla, C. Backes, *et al.*, "Scalable production of large quantities of defect-free few-layer graphene by shear exfoliation in liquids," *Nature Materials*, vol. 13, no. 6, pp. 624–630, 2014, ISSN: 1476-1122. DOI: 10.1038/nmat3944.

[84] K. Wang, Y. Feng, C. Chang, J. Zhan, C. Wang, Q. Zhao, J. N. Coleman, L. Zhang, W. Blau, and J. Wang, "Broadband ultrafast nonlinear absorption and nonlinear refraction of layered molybdenum dichalcogenide semiconductors," *Nanoscale*, vol. 6, pp. 10 530–10 535, 2014, ISSN: 2040-3364. DOI: 10.1039/C4NR02634A.

[85] S. Cho, S. Kim, J. H. Kim, *et al.*, "Phase patterning for ohmic homojunction contact in mote2," *Science*, vol. 349, no. 6248, pp. 625–628, 2015, ISSN: 0036-8075. DOI: 10.1126/science.aab3175.

[86] G. Cunningham, D. Hanlon, N. McEvoy, G. S. Duesberg, and J. N. Coleman, "Large variations in both dark- and photoconductivity in nanosheet networks as nanomaterial is varied from mos 2 to wte 2," *Nanoscale*, vol. 7, no. 1, pp. 198–208, 2015, ISSN: 2040-3364. DOI: 10.1039/C4NR04951A.

[87] X. Duan, C. Wang, A. Pan, R. Yu, and X. Duan, "Two-dimensional transition metal dichalcogenides as atomically thin semiconductors: Opportunities and challenges," *Chem. Soc. Rev.*, vol. 44, no. 24, pp. 8859–8876, 2015, ISSN: 0306-0012. DOI: 10.1039/C5CS00507H.

[88] Y. Gao, Z. Liu, D.-M. Sun, *et al.*, "Large-area synthesis of high-quality and uniform monolayer ws2 on reusable au foils," *Nature Communications*, vol. 6, p. 8569, 2015, ISSN: 2041-1723. DOI: 10.1038/ncomms9569.

[89] D. Hanlon, C. Backes, E. Doherty, *et al.*, "Liquid exfoliation of solvent-stabilized few-layer black phosphorus for applications beyond electronics," *Nature Communications*, vol. 6, p. 8563, 2015, ISSN: 2041-1723. DOI: 10.1038/ncomms9563.

[90] C. Huo, Z. Yan, X. Song, and H. Zeng, "2d materials via liquid exfoliation: A review on fabrication and applications," *Science Bulletin*, vol. 60, no. 23, pp. 1994–2008, 2015, ISSN: 20959281. DOI: 10.1007/s11434-015-0936-3.

[91] Z. X. Khoo, J. E. M. Teoh, Y. Liu, C. K. Chua, S. Yang, J. An, K. F. Leong, and W. Y. Yeong, "3D printing of smart materials: A review on recent progresses in 4D printing," *Virtual and Physical Prototyping*, vol. 10, no. 3, pp. 103–122, 2015, ISSN: 1745-2759. DOI: 10.1080/17452759.2015.1097054.

[92] D. W. Latzke, W. Zhang, A. Suslu, T. R. Chang, H. Lin, H. T. Jeng, S. Tongay, J. Wu, A. Bansil, and A. Lanzara, "Electronic structure, spin-orbit coupling, and interlayer interaction in bulk mos2 and ws2," *Physical Review B - Condensed Matter and Materials Physics*, vol. 91, no. 23, pp. 1–6, 2015, ISSN: 1550235X. DOI: 10.1103/PhysRevB.91.235202.

[93] J. Ribeiro-Soares, C. Janisch, Z. Liu, A. L. Elias, M. S. Dresselhaus, M. Terrones, L. G. Cancado, and A. Jorio, “Second harmonic generation in wse2,” *2D Materials*, vol. 2, no. 4, p. 045 015, 2015, ISSN: 2053-1583. DOI: 10.1088/2053-1583/2/4/045015.

[94] F. Schwierz, J. Pezoldt, and R. Granzner, “Two-dimensional materials and their prospects in transistor electronics,” *Nanoscale*, vol. 7, no. 18, pp. 8261–8283, 2015, ISSN: 2040-3364. DOI: 10.1039/C5NR01052G.

[95] R. A. Susantyoko, X. Wang, L. Sun, W. Sasangka, E. Fitzgerald, and Q. Zhang, “Influences of annealing on lithium-ion storage performance of thick germanium film anodes,” *Nano Energy*, vol. 12, pp. 521–527, 2015, ISSN: 22112855. DOI: 10.1016/j.nanoen.2015.01.024.

[96] X. Yu, M. S. Prevot, N. Guijarro, and K. Sivula, “Self-assembled 2d wse2 thin films for photoelectrochemical hydrogen production,” *Nature Communications*, vol. 6, no. May, p. 7596, 2015, ISSN: 2041-1723. DOI: 10.1038/ncomms8596.

[97] H. Zhang, “Ultrathin two-dimensional nanomaterials,” *ACS Nano*, no. Xx, pp. 9451–9469, 2015, ISSN: 1936086X. DOI: 10.1021/acsnano.5b05040.

[98] K. G. Zhou, M. Zhao, M. J. Chang, Q. Wang, X. Z. Wu, Y. Song, and H. L. Zhang, “Size-dependent nonlinear optical properties of atomically thin transition metal dichalcogenide nanosheets,” *Small*, vol. 11, no. 6, pp. 694–701, 2015, ISSN: 16136829. DOI: 10.1002/smll.201400541.

[99] “2D Materials Beyond Graphene for High-Performance Energy Storage Applications,” *Advanced Energy Materials*, vol. 6, no. 23, p. 1 600 671, 2016, ISSN: 16146832. DOI: 10.1002/aenm.201600671.

[101] C. Backes, B. M. Szydlowska, A. Harvey, *et al.*, “Production of highly monolayer enriched dispersions of liquid-exfoliated nanosheets by liquid cascade cen-

trifugation," *ACS Nano*, vol. 10, no. 1, pp. 1589–1601, 2016, ISSN: 1936-0851. DOI: 10.1021/acsnano.5b07228.

[102] V. Forsberg, R. Zhang, J. B??ckstr??m, C. Dahlstr??m, B. Andres, M. Norgren, M. Andersson, M. Hummelg??rd, and H. Olin, "Exfoliated mos2 in water without additives," *PloS one*, 2016, ISSN: 19326203. DOI: 10.1371/journal.pone.0154522.

[103] J. J. Gought, K. E. Siewerskat, S. Mehigant, D. Hanlont, C. Backest, Z. Gholamvandt, and B. M. Szydloskat, "Ag nanoparticle decorated graphene oxide: Fluorescence quenching and surface enhanced raman scattering," no. September, pp. 121–123, 2016.

[104] Y. Li, N. Dong, S. Zhang, K. Wang, L. Zhang, and J. Wang, "Optical identification of layered mos 2 via the characteristic matrix method," *Nanoscale*, vol. 8, pp. 1210–1215, 2016, ISSN: 2040-3364. DOI: 10.1039/C5NR06287J.

[105] K. F. Mak and J. Shan, "Photonics and optoelectronics of 2d semiconductor transition metal dichalcogenides," *Nature Photonics*, vol. 10, no. 4, pp. 216–226, 2016, ISSN: 1749-4885. DOI: 10.1038/nphoton.2015.282.

[106] K. M. McCreary, A. T. Hanbicki, G. G. Jernigan, J. C. Culbertson, and B. T. Jonker, "Synthesis of large-area ws2 monolayers with exceptional photoluminescence," *Scientific Reports*, vol. 6, no. 1, p. 19 159, 2016, ISSN: 2045-2322. DOI: 10.1038/srep19159.

[107] J. Song, L. Xu, J. Li, J. Xue, Y. Dong, X. Li, and H. Zeng, "Monolayer and Few-Layer All-Inorganic Perovskites as a New Family of Two-Dimensional Semiconductors for Printable Optoelectronic Devices," *Advanced Materials*, vol. 28, no. 24, pp. 4861–4869, 2016, ISSN: 09359648. DOI: 10.1002/adma.201600225. arXiv: arXiv:1011.1669v3.

[109] K. Wang, B. M. Szyd, G. Wang, X. Zhang, J. J. Wang, J. J. Magan, L. Zhang, J. N. Coleman, J. Wang, and W. J. Blau, "Ultrafast nonlinear excitation dynamics of," 2016. DOI: `10.1021/acsnano.6b02770`.

[110] K. Wang, B. M. Szydlowska, G. Wang, X. Zhang, J. J. J. Wang, J. J. Magan, L. Zhang, J. N. Coleman, J. J. J. Wang, and W. J. Blau, "Ultrafast nonlinear excitation dynamics of black phosphorus nanosheets from visible to mid-infrared," *ACS Nano*, vol. 10, no. 7, pp. 6923–6932, 2016, ISSN: 1936086X. DOI: `10.1021/acsnano.6b02770`.

[111] Q. Zhang, F. Zhang, S. P. Medarametla, H. Li, C. Zhou, and D. Lin, "3D Printing of Graphene Aerogels," *Small*, vol. 12, no. 13, pp. 1702–1708, 2016, ISSN: 16136810. DOI: `10.1002/smll.201503524`.

[112] T. Carey, S. Cacovich, G. Divitini, J. Ren, A. Mansouri, J. M. Kim, C. Wang, C. Ducati, R. Sordan, and F. Torrisi, "Fully inkjet-printed two-dimensional material field-effect heterojunctions for wearable and textile electronics," *Nature Communications*, vol. 8, no. 1, p. 1202, 2017, ISSN: 2041-1723. DOI: `10.1038/s41467-017-01210-2`.

[113] K.-S. Chen, I. Balla, N. S. Luu, and M. C. Hersam, "Emerging Opportunities for Two-Dimensional Materials in Lithium-Ion Batteries," *ACS Energy Letters*, vol. 2, no. 9, pp. 2026–2034, 2017, ISSN: 2380-8195. DOI: `10.1021/acsenergylett.7b00476`.

[114] M. Cugov, D. Jasna Jablan Jasmina Lovri, N. G. Cin, and J. Mario, "Accepted manuscript," *Journal of Pharmaceutical and Biomedical Analysis*, 2017, ISSN: 9031220280. DOI: `10.1016/j.jpba.2017.01.025`.

[115] H. Gullapalli, K. Kalaga, S. Vinod, M.-T. F. Rodrigues, A. George, and P. M. Ajayan, "2D material integrated macroporous electrodes for Li-ion batteries,"

RSC Advances, vol. 7, no. 52, pp. 32 737–32 742, 2017, ISSN: 2046-2069. DOI: 10.1039/C7RA05354A.

[116] A. Harvey, J. B. Boland, I. Godwin, A. G. Kelly, B. M. Szydlowska, G. Murtaza, A. Thomas, D. J. Lewis, P. OBrien, and J. N. Coleman, “Exploring the versatility of liquid phase exfoliation: Producing 2d nanosheets from talcum powder, cat litter and beach sand,” *2D Materials*, vol. 4, no. 2, p. 025 054, 2017, ISSN: 2053-1583. DOI: 10.1088/2053-1583/aa641a.

[117] S. M. Holmes, P. Balakrishnan, V. S. Kalangi, X. Zhang, M. Lozada-Hidalgo, P. M. Ajayan, and R. R. Nair, “2D Crystals Significantly Enhance the Performance of a Working Fuel Cell,” *Advanced Energy Materials*, vol. 7, no. 5, p. 1 601 216, 2017, ISSN: 16146832. DOI: 10.1002/aenm.201601216.

[118] A. G. Kelly, T. Hallam, C. Backes, *et al.*, “All-printed thin-film transistors from networks of liquid-exfoliated nanosheets,” *Science*, vol. 356, no. 6333, pp. 69–73, 2017, ISSN: 0036-8075. DOI: 10.1126/science.aal4062.

[119] L. Khalil, E. Papalazarou, M. Caputo, *et al.*, “Electronic band structure for occupied and unoccupied states of the natural topological superlattice phase sb2te,” *Physical Review B*, vol. 95, no. 8, pp. 1–6, 2017, ISSN: 24699969. DOI: 10.1103/PhysRevB.95.085118.

[120] “Re-inventing print,” *Nature Nanotechnology*, vol. 12, no. 4, pp. 283–283, 2017, ISSN: 1748-3387. DOI: 10.1038/nnano.2017.64.

[121] L. Shi and T. Zhao, “Recent advances in inorganic 2D materials and their applications in lithium and sodium batteries,” *Journal of Materials Chemistry A*, vol. 5, no. 8, pp. 3735–3758, 2017, ISSN: 2050-7488. DOI: 10.1039/C6TA09831B.

[122] G. Wang, K. Wang, B. M. Szydlowska, A. A. Baker-Murray, J. J. Wang, Y. Feng, X. Zhang, J. Wang, and W. J. Blau, “Ultrafast nonlinear optical properties of a graphene saturable mirror in the 2 um wavelength region,”

Laser Photonics Reviews, vol. 1700166, p. 1 700 166, 2017, ISSN: 18638880. DOI: 10.1002/lpor.201700166.

[123] Y. Han, Y. Ge, Y. Chao, C. Wang, and G. G. Wallace, "Recent progress in 2D materials for flexible supercapacitors," *Journal of Energy Chemistry*, vol. 27, no. 1, pp. 57–72, 2018, ISSN: 20954956. DOI: 10.1016/j.jechem.2017.10.033.

[124] ——, "Recent progress in 2D materials for flexible supercapacitors," *Journal of Energy Chemistry*, vol. 27, no. 1, pp. 57–72, 2018, ISSN: 20954956. DOI: 10.1016/j.jechem.2017.10.033.

[125] J. Wilson and A. Yoffe, "The transition metal dichalcogenides,"

Monographs & Textbooks

[21] A. U. Acuna and F. Amat-Guerri, *Early History of Solution Fluorescence: The Lignum nephriticum of Nicolas Monardes*, M. N. Berberan-Santos, Ed. Springer Berlin Heidelberg, 2008, pp. 3–20. DOI: 10.1007/42432007006.

[100] C. Backes, D. Hanlon, B. M. Szydlowska, A. Harvey, R. J. Smith, T. M. Higgins, and J. N. Coleman, *Preparation of Liquid-exfoliated Transition Metal Dichalcogenide Nanosheets with Controlled Size and Thickness: A State of the Art Protocol*, 118. 2016, vol. 2016, e54806–e54806. DOI: 10.3791/54806.

[108] B. Szydlowska, *Highly Monolayer Enriched WS2 Dispersions Produced by Liquid Phase Exfoliation in Liquid Cascade as Nonlinear Optical Materials*, ser. OSA Technical Digest (online). OSA, 2016, NoTu3D.5. DOI: 10.1364/NOMA.2016.NoTu3D.5.